METHODS FOR SURFACE AGE ESTIMATION AND STUDY OF EVAPORATIVE COOLING INDUCED AIR-WATER GAS TRANSFER

A thesis submitted for the degree of

Doctor of Philosophy

by

Fatima Ali

Department of Mechanical and Aerospace Engineering

College of Engineering, Design and Physical Sciences

Brunel University London

Uxbridge, UB8 3PH

United Kingdom

July 2020

Supervision:

Dr. Jan G. Wissink

Dr. Tze Pei Chong

"إِنَّهُ مَنْ يَتَّقِ وَيَصْبِرْ فَإِنَّ اللَّهَ لا يُضِيعُ أَجْرَ الْمُحْسِنِينَ"

سورة يوسف الآية 90

Acknowledgment

In the name of Allah, the Most Gracious and the Most Merciful.

Alhamdulillah, all praises to Almighty Allah for the strengths and His blessing in completing this thesis. Firstly, I would like to express my sincere gratitude to my supervisor Dr. Jan G. Wissink for his guidance, encouragement and support throughout my PhD research. His invaluable help and advice of constructive suggestions throughout my thesis work have contributed to success of this research. I could not have imagined having a better advisor and mentor for my PhD study. I would like to give special thanks to my co-advisor Dr. Tze Pei Chong.

I gratefully acknowledge the support by the state of Baden-Würrtemberg for the computing time on bwHPC and the support by the Gauss Centre for Supercomputing e.V. for providing computing time on the GCS Super- computer SUPERMUC-NG at Leibniz Supercomputing Centre.

I am grateful to my parents and parents-in-law for their prayers, understanding and motivational support.

To my husband: Thank you for always believing in me and for being by my side throughout this long period of my research. I could not have done this without you.

My appreciation also goes to my dearest friends for sharing their research experience.

Declaration

I declare that this dissertation is the result of my own work except where specifically indicated in the text. It has not been previously submitted, in part or whole, to any university or institution for any degree, diploma, or other qualification.

Fatima Ali

(Student ID: 1537854)

Contents

Acknowledgment **4**

Declaration **5**

1 Introduction **1**

1.1 Research Background 1

1.2 Aim and objectives 7

1.3 Thesis outline 10

2 Literature review **12**

2.1 Fundamental concepts 12

2.2 Gas transfer velocity K_L 14

2.3 Surface age (τ) 15

2.4 Gas transfer models 17

2.4.1 Conceptual models 18

2.4.1.1 Film model 18

2.4.1.2 Penetration model 19

2.4.1.3 Surface renewal model 20

2.4.1.4 Film-renewal model 21

2.4.1.5 Random eddy model 21
2.4.1.6 Surface divergence model 22
2.4.2 Hydrodynamic models 22
2.4.2.1 Large-eddy model 23
2.4.2.2 Small-eddy model 23
2.4.3 Eddy diffusivity models 24
2.5 Analysis of scalar transport mechanism 25
2.5.1 Buoyant convectively induced turbulence 26
2.5.2 Wind-shear turbulence 28
2.5.3 Bottom-shear turbulence 30
2.6 WENO schemes 32
2.7 Surface film effects 34
2.7.1 Surface tension 34
2.7.2 Marangoni effect 35

3 Lagrangian approach 36
3.1 Lagrangian Modelling 36
3.1.1 Reconstruction of 3D velocity field adjacent to the surface . . . 39
3.1.2 Lagrangian method 41
3.2 Weighted/Non-weighted $\overline{\tau}$ 46
3.3 Mesh refinement study 47
3.4 Results 49

4 Continuum method 59

4.1 Introduction 59
4.1.1 Two ways to observe fluid flow 61
4.2 Numerical Aspects 63
4.2.1 WENO-Z scheme in a 1D test problem 63
4.2.2 Grid refinement studies in 3D 66
4.3 Modelling used in the continuum method 70
4.3.1 Probability density distributions of surface age 73
4.4 Overestimation of surface age 76
4.5 Results and discussions 82

5 Marangoni forces 89
5.1 Introduction 89
5.2 Methodology 90
5.3 Boundary conditions 95
5.4 Overview of the simulations 96
5.5 Grid refinement study 99
5.6 Flow field 105
5.6.1 Instantaneous scalar structures near the surface 112
5.7 Scalar transport 121
5.7.1 Concentration boundary layer 121
5.7.2 Horizontally averaged temperature and concentration profiles . . 122
5.7.3 Mass flux 131
5.7.4 Gas transfer velocity 134
5.8 Conclusion 139

6 Conclusion and suggestions for future work 140

6.1 Conclusion 140

6.2 Suggestions for future work 143

List of Tables

3.1 Overview of the simulations. A structured (Cartesian) mesh was used to resolve the water phase. 39

3.2 Times of the velocity field snapshots used to calculate K_L 39

3.3 Number of active particles using the initial w velocity classes for simulation BT10 50

3.4 Averaged relative error (ARE) in gas transfer velocity K_L 57

3.5 Maximum relative error (MRE) in gas transfer velocity K_L 58

4.1 The maximum absolute error MAE in τ and the order of accuracy p . . 65

4.2 Refinement of cells in z direction for simulation BT10 using $N = 7$ and $RXY = 5$ 68

4.3 Refinement of cells in the x, y directions for simulation BT10 using N=7 and RZ=10 69

4.4 Influence of N on mean surface age $\overline{\tau}$ for simulation BT10, BT20 and BY10 with the refinement of RXY=5 and RZ=10 69

4.5 Averaged relative error of mean surface age $\overline{\tau}$ 85

4.6 Relative error in the gas transfer velocity K_L 88

5.1 Overview of simulations. In all simulations the Prandtl number Pr was set to 7 typically for water at 293.15 K, 5L $\times$ 5L $\times$ 5L Domain and 200 $\times$ 200 $\times$ 252 base mesh size is used. The Kolmogorov scale is denoted by η. 99

5.2 Grid refinement study, domain size= 5L $\times$ 5L $\times$ 5L, $Ma = 1049$, $\pi \mathrm{L}_{B,Sc=16} = 0.041$, $\pi \mathrm{L}_{B,Sc=200} = 0.0116$. 101

List of Figures

1.1 Schematic illustration of the turbulence generating sources introducing atmospheric gas transfer in the water. Produced following the example of Herlina [31] 8

1.2 Flow chart showing how gas transfer velocity is determined in Chapters 3, 4 and 5. 11

2.1 Motion of fluid parcels 17

2.2 Two-phase flow for sheared wavy interface [52]. 30

3.1 Time-step sensitivity study for BT10 simulation comparing first order Euler method to second order Adams-bashforth AB2 method at time $t = 16.7$ s. See Tables 3.1 and 3.2 43

3.2 Horizontal velocity vectors and magnitude (contours), representing $\partial w/\partial z$, at the interface of BY10 simulation at $t = 50$ s and $t = 100$ s 45

3.3 p-refinement 47

3.4 Mesh refinement study, when particles are initially placed at the nodes of the mesh. 48

3.5 Particle paths of seven individual particles at time $t = 50$ s for BY10 simulation. 49

3.6 Influence of initial w velocity classes on number of active particles (P) for simulation BT10 51
3.7 Influence of initial w velocity on $\overline{\tau}_w$ and $\overline{\tau}_{nw}$ for simulation BT10 . . . 52
3.8 The gas transfer velocity K_L in time for simulation BT10 for case (a) WF, NWF and (b) WB, NWB. 53
3.9 The gas transfer velocity K_L in time for simulation BT20 for case (a) WF, NWF and (b) WB, NWB. 54
3.10 The gas transfer velocity K_L in time for simulation BY10 for case (a) WF, NWF and (b) WB, NWB. 55
3.11 The gas transfer velocity K_L in time for simulation BY20 for case (a) WF, NWF and (b) WB, NWB. 56

4.1 A material volume and a Eulerian control volume 61
4.2 Schematic showing a cross section of the concentration boundary layer adjacent to the surface and the deformation of fluid parcel 62
4.3 Effect of refinement in z-direction (1D periodic box) 65
4.4 Schematic illustration of the width of $(\Delta z/N)$ of the initial surface age density distribution ρ_τ. N represents the number of mesh cells in the z-direction. Δz is the depth of the computational domain and $\rho_\tau > 0$ only in the mesh cell at the bottom. Note that $z_{top} = 0$ corresponds to the surface. 67
4.5 Schematic of continuum method, using $N = 3$ cells in the z-direction and a refinement in z of $RZ = 10$. 70

4.6 (a) Cumulative distribution and (b) comparison between the instantaneous probability distribution calculated directly from the continuum method (direct-ρ_τ) and lognormal distribution (theory-ρ_τ) of the surface age (for BT10 simulation at $t = 100\,\mathrm{s}$ for N=32, RZ=10, RXY=5, using $\mu = 1.495$ and $\sigma^2 = 1.137$). 74

4.7 (a) Cumulative distribution and (b) comparison between the instantaneous probability distribution calculated directly from the continuum method (direct-ρ_τ) and lognormal distribution (theory-ρ_τ) of the surface age (for BT20 simulation at $t = 31.73\,\mathrm{s}$ for N=16, RZ=10, RXY=5, using $\mu = 1.930105$ and $\sigma^2 = 1.262667$). 75

4.8 (a) Cumulative distribution and (b) comparison between the instantaneous probability distribution calculated directly from the continuum method (direct-ρ_τ) and lognormal distribution (theory-ρ_τ) of the surface age (for BY10 simulation at $t = 90\,\mathrm{s}$ for N=16, RZ=10, RXY=5, using $\mu = 1.46187$ and $\sigma^2 = 0.80147$). 75

4.9 Overestimation of surface age by assuming the (a) upward and downward velocities are the same and (b) upward and downward velocities differ for simulation BY10. 82

4.10 Effect of N on mean surface age $\overline{\tau}$ using Rz=10 and RXY=5 for simulation (a) BT10 at $t = 16.7$s, (b) BT20 at $t = 31.73$s and (c) BY10 at $t = 90$s. 84

4.11 Gas transfer velocity K_L in time at $t = 16.7$s for simulation BT10 using RZ=10, RXY=5 and N=32. 86

4.12 Gas transfer velocity K_L in time at $t = 31.73$s for simulation BT20 using RZ=10, RXY=5 and N=32. 87

4.13 Gas transfer velocity K_L in time at $t = 90$s for simulation BY10 using RZ=10, RXY=5 and N=32. 87

5.1 Surface tension of water, data taken from [89] 96

5.2 u-velocity component profile after $t = 80$s at $z/L = 4.5$ using different grid sizes. Only every sixth data point is shown. 101

5.3 v-velocity component profile after $t = 80$s at $z/L = 4.5$ using different grid sizes. Only every sixth data point is shown. 102

5.4 w-velocity component profile after $t = 80$s at $z/L = 4.5$ using different grid sizes. Only every sixth data point is shown. 103

5.5 Temperature profile ($Ma = 1049$) after $t = 80$s showing (a) T at the center line $y/L = 2.5$ and (b) at $x/L = 2.5$ and $z/L = 4.5$ obtained using different grid sizes (see Table. 5.2). Only every third data point is shown. 104

5.6 Concentration profile ($Ma = 1049$) after $t = 80$ s showing (a) C at the center line $y/L = 2.5$ and (b) at $x/L = 2.5$ and $z/L = 4.5$ from simulations with different scalar grid refinement factors (see Table. 5.2). Only every third data point is shown. 105

5.7 Marangoni effects on u_{rms} at time $t = 150$s. Only every fifth data point is shown. 106

5.8 Marangoni effects on w_{rms} at time $t = 150$s. Only every fifth data point is shown. 107

5.9 Influence of Marangoni number $Ma = 0, 70, 350$ on integral length scale. 108

5.10 Surface divergence contours from simulation (a) MB03 and (b) MB13 . 110

5.11 Snapshots of instantaneous surface divergence contours from simulation (a) MB03 and (b) MB13 111

5.12 Surface divergence contours from simulation (a) MB03, (b) MB13 and (c) MB10 111

5.13 Velocity vectors and magnitude (contours) of scalar distribution for $Sc = 50$ at the surface. Snapshots taken at time $t = 77$ s from simulation (a) MB03 and (b) MB13. 113

5.14 Temperature distribution at the surface from simulation (a) MB03 (b) MB13 and (c) MB10. 114

5.15 Temperature contours in the cross section at $x/L = 2.5$ (identified by the arrow in Fig. 5.14a) of simulation MB03. 115

5.16 Temperature visualization from the simulation MB53. 116

5.17 Visualization of scalar transport for $Sc = 100$ from the simulation MB03. 118

5.18 Visualization of scalar transport for $Sc = 100$ from the simulation MB53. 119

5.19 Visualization of scalar transport from the simulation MB03 for the cases (a) $Sc = 16$ and (b) $Sc = 200$. The thickness of boundary layer reduces with increasing Schmidt number. 120

5.20 Growth of the boundary layer thickness for various values of the non-dimensional surface heat flux for Marangoni number (a) $Ma = 0$ (b) $Ma = 70$ and (c) $Ma = 350$. 121

5.21 Influence of different values of Marangoni $Ma = 0, 70, 350$ on the horizontally averaged surface temperature in the presence of a constant value of the non-dimensional surface heat flux of $\phi_T = 1.5$. 123

5.22 Non-dimensional horizontally averaged temperature profiles for simulation (a) MB03 and (b) MB53. 124

5.23 Marangoni effects on the instantaneous Rayleigh number Ra_δ in the presence of a constant non-dimensional surface heat flux of $\phi_T = 1.5$. 125

5.24 Maximum of T_{rms} in time to observe the effects of (a) Marangoni forces and (b) non-dimensional surface heat flux. 126

5.25 Marangoni effects on horizontally averaged T_{rms} distribution using the Schmidt number $Sc = 16$ at $t = 101.25$s for various non-dimensional surface heat flux of ϕ_T (a) 0.777, (b) 1.5 and (c) 2.33. 128

5.26 Marangoni effects on horizontally averaged C_{rms} distribution at $t = 101.25$s for various non-dimensional surface heat flux of ϕ_T (a) 0.777, (b) 1.5 and (c) 2.33. 130

5.27 Variation of mass flux with depth at $t = 200$s using a non-dimensional heat flux of $\phi_T = 0.777$. The mass fluxes are normalised with total flux ($D\partial\overline{c}/\partial z + < c'w' >$). Diffusive $-D\partial\overline{c}/\partial z$ (solid lines) and convective $< c'w' >$ (dashed lines) mass fluxes plotted against z/L at various Sc numbers for (a) $Ma = 0$ (MB01) and (b) $Ma = 70$ (MB11). Only every fifth data point is shown. 132

5.28 Variation of mass flux with depth z/L at various Sc numbers for $Ma = 0$ (MB01) and $Ma = 70$ (MB11) with a fixed non-dimensional heat flux $\phi_T = 0.777$ at $t = 200$s. The mass fluxes are normalised with total flux $(D\partial\overline{c}/\partial z + < c'w' >)$. 133

5.29 Variation of mass flux with depth for two different Marangoni numbers (a) $Ma = 0$ (blue line) and $Ma = 70$ (red line) with a constant Schmidt number $Sc = 50$ at $t = 200$s. (b) Detailed plot of variation of mass flux with depth for $Ma = 0$ and 70 with $Sc = 50$ and $\phi_T = 0.777$. 134

5.30 Variation of transfer velocity K_L with Schmidt number $Sc = 16, 50, 100, 200$ at time $t = 150$s. 135

5.31 Comparison of the gas transfer velocity K_L obtained by using the surface divergence model (SDM) and the direct numerical simulation (DNS) with the non-dimensional surface heat flux for Marangoni forces (a) $Ma = 0$, (b) $Ma = 70$ and (c) $Ma = 350$. 136

5.32 Effect of Marangoni $Ma = 0, 70, 350$ on the gas transfer velocity K_L. . 138

Nomenclature

$(.^*)$	Non-dimensional quantities	$(-)$
α	Thermal expansion factor	$(1/K)$
β	Surface divergence	$(1/s)$
ΔT	Temperature difference	(K)
δ	Thickness of the concentration boundary layer	(m)
δ_t	Time interval	(s)
δ_{i3}	Kronecker delta	$(-)$
ϵ	Turbulent energy dissipation rate	(m^2/s^3)
η	Kolmogorov length scale	(m)
μ	Dynamic viscosity	$(kg/m/s)$
ν	Kinematic viscosity of water	(m^2/s)
$\overline{\tau_w}$	Weighted mean surface age	(m/s)

$\overline{\tau_{nw}}$	Non-weighted mean surface age	(m/s)
$\overline{\tau}$	Mean surface age	(m/s)
ρ	Density	(kg/m^3)
$\rho(\tau)$	Probability density distribution of surface age	$(-)$
ρ_τ	Surface age density	(kg/m^3)
σ	Surface tension	(N/m)
τ	Surface age	(m/s)
C_b	Dissolved gas concentration in bulk region	(kg/m^3)
C_s	Gas concentration at the surface	(kg/m^3)
C_τ	Cumulative distribution of surface age	$(-)$
D	Gas molecular diffusion	(m/s)
g	Gravitational acceleration	(m/s^2)
K_L	Gas transfer velocity	(m)
L	Characteristic length scale	(m)
L_x	Computational domain size in x-direction	(m)
L_y	Computational domain size in y-direction	(m)
L_z	Computational domain size in z-direction	(m)

Ma	Marangoni number	$(-)$
P	Number of active particles	$(-)$
r	Renewal time	(s)
Ra	Rayleigh number	$(-)$
Re	Reynolds number	$(-)$
Sc	Scmidt number	$(-)$
T	Temperature	(K)
t	Time	(s)
T_b	Bulk temperature	(K)
T_r	Renewal time	(s)
U	Characteristic velocity scale	(m/s)
u	Velocity component in x-direction	(m/s)
u'	Fluctuating velocity	(m/s)
u'_L	Root mean square of turbulent fluctuations	(m/s)
u_∞	Turbulent velocity scale	(m/s)
v	Velocity component in y-direction	(m/s)
w	Velocity component in z-direction	(m/s)

w_{th}	Threshold	$(-)$

Abbriviations

1D One dimensional

2D Two dimensional

3D Three dimensional

AB2 Second order Adams-Bashforth method

ARE Averaged relative error

BL Boundary layer

DNS Direct numerical simulation

HLTT Hybrid Lagrangian tracking and temperature

LES Large eddy simulation

MAE Maximum absolute error

MPI Message passing interface

MRE Maximum relative error

NWB Non-weighted backward

NWF Non-weighted forward

SDM Surface divergence model

WB Weighted backward

WENO Weighted essentially non-oscillatory

WF Weighted forward

Abstract

This thesis presents numerical studies of fundamental fluid mechanical mechanisms that play a role in the transfer of atmospheric gases across the air-water interface. At first numerical methods are discussed that allow the calculation of the mean surface age and the interfacial gas transfer velocity from snapshots of the interfacial flow field. After constructing the near-surface three-dimensional (3D) velocity field from the interfacial velocity field, first the Lagrangian particle tracking method is employed to estimate the mean surface age. Subsequently, a new continuum method was developed as an alternative to the Lagrangian approach. To estimate the mean surface age, a continuous surface age density was introduced to replace the point particles used in the Lagrangian method. To obtain a smooth initial density distribution on the uniform base mesh in the z-direction, N number of mesh cells were used. Each grid cell was refined in the x, y and z-direction by a factor of $RXY = 5$ and $RZ = 10$, respectively. On the refined mesh, an unsteady three-dimensional convection equation for the surface age density was solved using the fifth-order-accurate WENO-Z scheme for the convection terms combined with a third-order Runge-Kutta method for the time-integration. For the surface age density, ρ_τ, a symmetry boundary condition was used at the surface, while below the region where the initial surface age density was introduced, ρ_τ was set to zero, to model that the surface age density left the near surface region. The results obtained with the continuum method were in good agreement with the results from the Lagrangian particle tracking method.

Subsequently, the effects of Marangoni forces, induced by temperature differences at the air-water interface, on the instantaneous development of a buoyant convective instability for several Sc-numbers was studied by Direct Numerical Simulation (DNS). Simultaneously with the flow, five scalar convection diffusion equations were solved. The first scalar, the temperature, is non passive as it affects the flow through buoyancy forces. The other scalars are passive and represent the transport of atmospheric gases. The Prandtl number for the temperature was $Pr = 7$ and the Schmidt numbers for the mass transport were $Sc = 16, 50, 100, 200$. The latter simulations allow a non biased comparison of the effect of Schmidt number on the gas transfer velocity K_L.

For the flow solver, the convective terms were solved using the fourth order kinetic energy conserving discretization, while the diffusive term was solved using the fourth order central scheme. After substituting the descritized momentum equations into the continuity equation a Poison equation for the pressure was obtained. This Poison equation for the pressure was solved using the conjugate gradient method with simple diagonal decomposition. Time integration was performed using the second order Adams-Bashforth method. It was shown that Marangoni forces that promote the Rayleigh instability result in significant increases in the amount of atmospheric gases transferred across the air-water interface and should not be neglected.

Chapter 1

Introduction

This chapter includes the research background, aims and objectives of the research and an outline of the thesis. The research question, research model and motivation are discussed.

1.1 Research Background

Gas exchange across the air-water interface plays a vital role in environmental processes and various industrial applications in a range of engineering fields. The atmosphere and rivers, lakes, seas and oceans are essentially linked in a dynamical system. One typical example is the absorption of significant amounts of heat and gases into the oceans and other natural water bodies. For instance, the absorption of oxygen across the air-water interface is important to sustain aquatic life. The oceans constitute a major sink for heat and green house gases by removing significant quantities from the air. Due to this, the oceans tend to lessen the increase in carbon dioxide in the atmosphere which

is related to human activity. Unfortunately, this results in a significant increase in acidification which is very critical to the aquatic habitat and leads to the destruction of their life e.g. coral reefs. It is noted that up to 40% of the produced carbon dioxide is absorbed into the ocean, resulting in an increase in carbonic acid [19]. The production of carbonic acid decreases the CO_2 gas pressure. Thus, the significant capacity of ocean to absorb CO_2 from the atmosphere is for a huge part due to the formation of carbonic acid [80].

Heat transfer across the air-water interface is an important driver of weather conditions [48]. Absorption of heat reduces the oxygen solubility in water bodies so that less oxygen is carried from the water surface to the deeper regions leading to an oxygen depletion [59]. The gas transfer process does not only play an important role in global warming but also in re-aeration problems in rivers and lakes. This shows that an improved knowledge of the gas exchange mechanism is an important factor for the assessment and management of water quality.

Climate change has a significant effect on balancing the amount of gases absorbed in water bodies and the gases in atmosphere. The gas transfer models used for the prediction of climate change can be improved with a good understanding of the air-water gas exchange mechanism. In the first part of the present study, the estimation of surface age and gas transfer velocity using a continuum model is investigated. In the second part, the effect of Marangoni forces on the instantaneous development of the buoyant instability across the air-water interface is studied. At low wind speeds, due to evaporative cooling at night, the upper water surface cools down. As cold water is slightly heavier than warm water a buoyant instability is generated. By modelling

the water-surface cooling by a constant heat flux, the buoyant instability will cause horizontal gradients in the surface temperature field. Such gradients in the surface temperature give rise to gradients in the surface tension resulting in the occurrence of Marangoni forces. These forces tend to promote the buoyant instability.

Most of the flows are turbulent in nature. A turbulent flow is classified as an apparently random motion with a large variety (continuum) of different scales. The macro scales are basically determined by the largest scales in the turbulent flow. Whereas, the smallest scales (several order of magnitude smaller than macro scales) in the turbulent flow are determined by the micro scales (Kolmogorov scales) that characterise the dissipation of turbulent kinetic energy. A huge range of different scales exists in between the micro and macro scales (the so-called inertial range) at which turbulent kinetic energy is conserved. Energy is exchanged within this range of scales from small to large and vice versa. Kolmogorov [46] determined that the scaling of the turbulent energy spectrum in the inertial range as a power of the wave number is $k^{-5/3}$. Generally, the interaction of molecular diffusion and turbulence governs the air-water gas transfer process. The rate of transfer is controlled by resistance on the water side [33]. Turbulence is increasingly damped close to the water surface. Due to this, molecular diffusion is a much more effective and dominating source of gas transfer at the water surface than turbulent convection. If the turbulence is absent from the water, in time the molecular diffusion of gases towards the water bulk eventually becomes very slow. If turbulence is established (whether by bottom shear, wind shear or buoyancy), this process is significantly enhanced. Fundamentally, turbulence tends to decrease the thickness of the diffusive concentration boundary layer close to the surface. As a result,

diffusion becomes more effective at the surface. The typical boundary layer thickness of low soluble environmentally important gases such as oxygen is about $\delta \approx 10 - 1000\mu m$ [32], which makes it very hard to carry out precise measurements. Consequently, many researchers used conceptual models to explain the gas exchange process using measureable parameters such as turbulent Reynolds number or surface divergence. The film model developed by Lewis & Whitman (1924) [57] is the first and simplest model. It is assumed that both sides of the air-water interface are covered with a stagnant film, where only molecular diffusion takes place. Thus, the gas transfer was assumed to be governed by diffusion and the gas transfer velocity K_L is inversely proportional to the film thickness δ, so that

$$K_L = \frac{D}{\delta} \text{ m}/s, \tag{1.1}$$

where D is the diffusion of the gas in water. Realistically, this model is an oversimplification of the actual mechanism [63]. An improved model, that took the surface renewal events into accounts, was proposed by Higbie [34]. Higbie discovered that the existence of turbulence plays a vital role in the liquid-bulk by bringing up fresh packages of unsaturated liquid to the surface, thereby replacing the saturated liquid to the surface. The surface renewal time was considered as the typical time Δt between two consecutive renewal events. He assumed Δt to be constant. Danckwerts [14] improved the penetration model with the concept of the surface renewal rate r. For this he made two assumptions: The first one was that all fluid parcels at the surface have equal probability of being replaced by fresh fluid from the bulk of the fluid body, independent of their surface age τ. Therefore, the probability density function of the surface age τ in Danckwert's model is the exponential distribution. The second assumption made

by Danckwerts was that the diffusion is the only transport mechanism at the interface, which was also originally assumed by Higbie. Hence, the surface renewal model, encompassing the exponential distribution of the surface age, is expressed by

$$K_L = \sqrt{Dr} \ \mathrm{m}/s, \tag{1.2}$$

where the mean surface age $\tau = 1/r$ may be interpreted as the average time between surface renewal events and has to be determined by performing experiments. Many researchers tried to estimate the renewal rate r. Fortescue & Pearson [23] proposed the large-eddy model by making the assumption that the gas transport process is dominated by the large turbulent eddies. Therefore, the term r can be approximated by the ratio of the velocity rms the of large eddies and the integral length scale u'_L/L.The advection-diffusion equation of a steady roll cell was solved numerically resulting in the expression

$$K_L = a\sqrt{\frac{D\,.\,u'_L}{L}}, \tag{1.3}$$

where L is the turbulent integral length, u'_L is the root mean square of the turbulent fluctuations and a is a constant with value 1.46. However, for the higher turbulence levels Banerjee [7] and Lamont [53] concluded that the characteristic time scales of small eddies determined the renewal rate. Here r was defined by $r = \sqrt{\epsilon/\nu}$, where ϵ is the rate of turbulent energy dissipation close to the surface and ν is the kinematic viscosity. Using dimensional analysis the relation

$$K_L = b\sqrt{D}\,\left[\frac{\epsilon}{\nu}\right]^{1/4}, \tag{1.4}$$

is obtained, where b is the constant of proportionality. As an alternative, the two regime model was proposed by Theofanous *et al.* [85], which combines the large and small-eddy models. They suggested that the large-eddy model is appropriate for low turbulent Reynolds numbers Re_T and the small-eddy model for high Re_T turbulent flow and proposed the following expressions

$$K_L = 0.73\, u'\, Sc^{-0.5}\, {Re_T}^{-0.5} \quad \text{when} \quad Re_T < 500, \tag{1.5}$$

$$K_L = 0.25\, u'\, Sc^{-0.5}\, {Re_T}^{-0.25} \quad \text{when} \quad Re_T > 500, \tag{1.6}$$

where Sc is the Schmidt number and Re_T is the turbulent Reynolds number defined by

$$Re_T = \frac{u_\infty \Lambda}{\nu}, \tag{1.7}$$

where u_∞ is the root mean square (r.m.s) of the horizontal velocity fluctuations, Λ is two times the horizontal integral length scale of the fluctuations and ν is the kinematic viscosity.

Note that the rate of turbulent energy dissipation ϵ is estimated on the large-eddy scale as $\epsilon = u_\infty^3/\Lambda$. The critical value of Re_T separating both regimes is approximately 500. Another alternative model to calculate the renewal rate r is the surface divergence model, proposed by McCready *et al.* [63]. Here, the 2D divergence of the velocity at the surface is used to calculate r. Using this model, the gas transfer velocity is estimated by

$$K_L = c\sqrt{D\beta'}, \tag{1.8}$$

where D is the molecular diffusivity, c is the constant of proportionality and β' is the r.m.s of the surface divergence. More detailed information on the gas transfer models is given in Sections 2.4.1 and 2.4.2.

1.2 Aim and objectives

In order to sustain aquatic life, atmospheric gas transfer from air into water, for instance seas, lakes, rivers and oceans is very important. The low soluble atmospheric gas transfer across the air-water interface is governed by resistance at the water side. The gas transfer is determined by the gas flux. At the liquid surface, the gas flux is fully determined by molecular diffusion and the amount of molecular diffusion is determined by the concentration boundary layer thickness underneath the surface. The thinner the concentration boundary layer thickness, the more molecular diffusion of gases will occur. Deep down into the bulk, molecular diffusion becomes insignificant and the vertical atmospheric gas transport is fully dominated by turbulent convection. In nature, turbulence can be generated in the environment by three major mechanisms, namely bottom-shear-induced turbulence (e.g. in windless rivers), surface-shear-induced turbulence (e.g. wind shear on lakes) and buoyant-convective-induced turbulence (e.g. turbulence in lakes caused by surface cooling). Figure 1.1 shows a schematic of the three distinct types of turbulent generating sources. The present study is focused on quantifying the mean surface age and the gas transfer velocity using the surface velocity field as obtained in experiments or numerical simulations. After constructing the near-surface three-dimensional velocity field, first the Lagrangian particle tracking method is employed to estimate the mean surface age, Subsequently a new continuum method was

developed as an alternative to the Lagrangian approach. The main advantage of the continuum method is the ease with which this can be implemented within a numerical code where it can be used to determine the mean surface age while the simulation is running. Apart from this, it also provides a very good approximation of the lognormal distribution of surface ages.

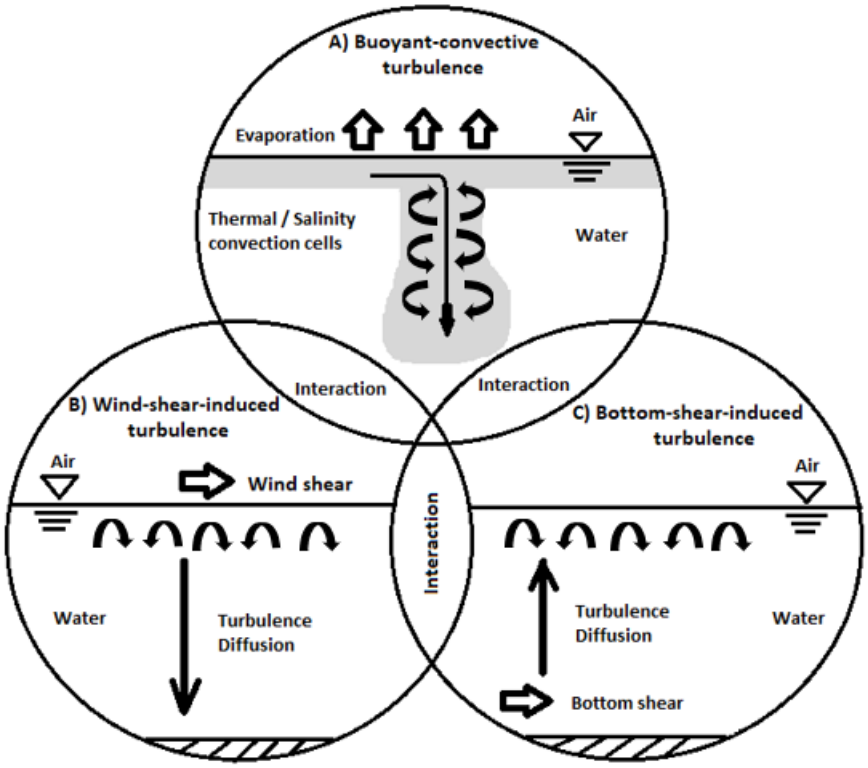

Figure 1.1: Schematic illustration of the turbulence generating sources introducing atmospheric gas transfer in the water. Produced following the example of Herlina [31]

Many researchers have focused on the most dominant gas transport process, which is the one induced by wind-shear, such turbulence is introduced directly at the surface.

This turbulence generating process is very important when sufficiently high wind speeds produce significant amounts of shear. The other two processes becomes more important if the wind speed is low. In rivers, the dominant turbulence-inducing mechanism driving the interfacial gas transfer is bottom-shear-induced turbulence. However, buoyancy-induced turbulence may be the most important turbulent source in sheltered lakes or in oceans at low wind speed conditions.

The role of interfacial velocity field in the determination of the gas transfer velocity is not fully understood. The aim of this thesis is to investigate the dependence of the gas transfer velocity on the interfacial velocity field. For this purpose both existing velocity fields generated in previous DNS as well as newly generated data (studying the temperature induced Marangoni forces from the interfacial velocity field) were used.

To reach this aim the following research objectives were set:

- Development of a continuum method to calculate mean surface age.
- Applying the continuum method to determine the probability distribution of the surface age.
- Use results generated by the continuum method to directly calculate the interfacial gas transfer velocity from a 2D velocity field stored at the surface.
- To show that surface temperature-gradient-induced Marangoni forces cannot be ignored when simulating the development of a buoyant convective instability driven by a fixed temperature-gradient at the surface (to model cooling).
- Performing a series of runs to study the effects of Marangoni forces on the instantaneous development of a buoyant convective instability for several Sc-numbers

per simulation.

- Performing a grid refinement test to see whether the results produced at realistic Marangoni number Ma are mesh-independent.

1.3 Thesis outline

The relevant background with a description of the gas transfer problem of the present research is presented in Chapter 1. This chapter also covers the objectives, and a brief summary of the methodology which is presented in more detail in further chapters. Chapter 2 covers the relevant literature review on air-water gas transfer processes. It also discusses the conceptual models of gas transfer including theoretical background as well as previous experimental investigations on gas transfer and previously obtained results related to the effect of Marangoni forces on the properties of turbulent flow. In Chapter 3, the methodology, and in particular the numerical techniques used in the implementation of the Lagrangian particle method for the estimation of the surface age and gas transfer velocity using the Danckwert's model, are presented. The reconstruction of the three-dimensional near-surface velocity fields, and the Euler and Adams-Bashforth method used for the time-integration are also discussed. Chapter 4 presents the development of the continuum method to calculate the gas transfer velocity. This chapter also presents a comparison of the results obtained from the Lagrangian and continuum method. In Chapter 5, it is shown that Marangoni forces cannot be ignored when simulating the development of a buoyant convective instability driven by a fixed temperature-gradient at the surface (to model evaporative cooling). A grid

refinement study is performed to see whether the results produced at realistic Ma are mesh-independent. Finally, Chapter 6 presents the conclusion of the present research and also recommendations for future research.

Figure 1.2: Flow chart showing how gas transfer velocity is determined in Chapters 3, 4 and 5.

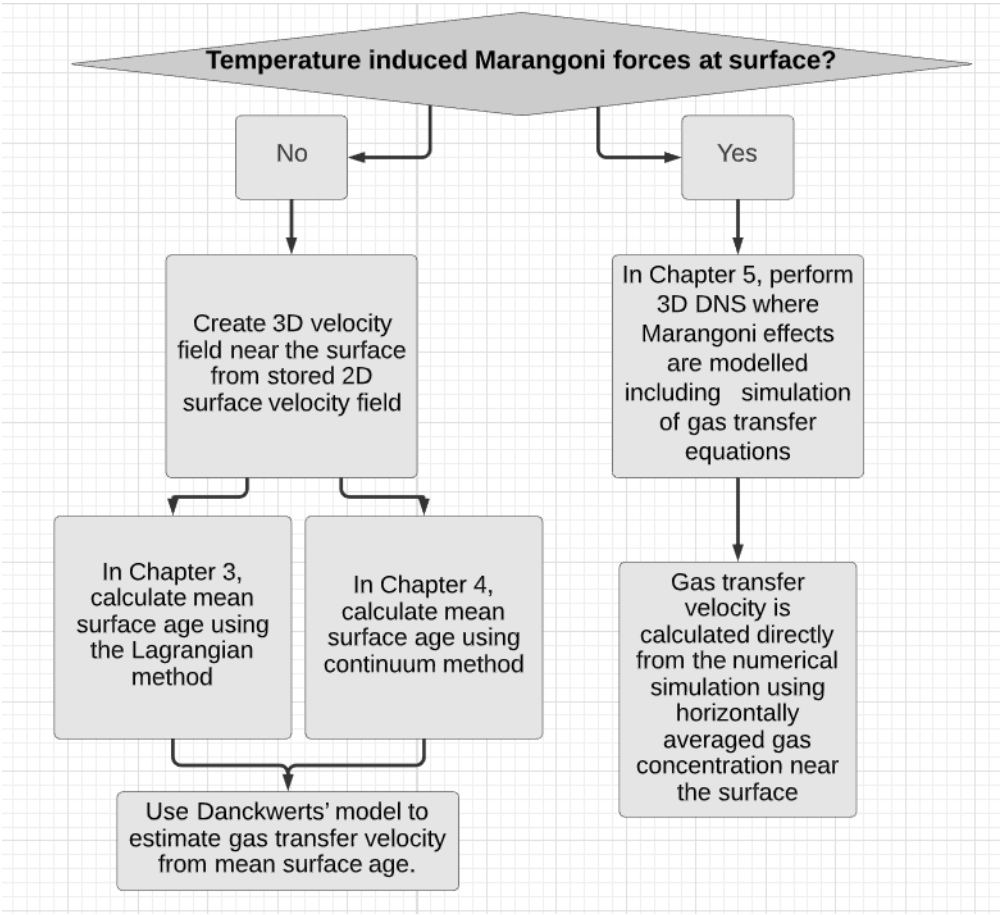

Chapter 2

Literature review

In this chapter, a comprehensive review on gas transfer processes and the importance of surface age including a summary of the theoretical background, existing gas transfer models using various parameters, experimental investigations on gas transfer as well as their development and shortcomings are presented. Research models and numerical methods introduced in this study are based on the above analysis.

2.1 Fundamental concepts

The gas transfer process across the air-water interface of low soluble gases such as oxygen O_2, carbon monoxide CO, nitric oxide NO and ozone O_3 is controlled by resistance on the water side. Gas transfer of a stationary fluid without any disturbances is governed by the molecular diffusion. However, in more realistic cases the fluid may be in motion generated by bottom shear, wind shear, buoyant convection due to surface cooling or any combination of these (see Figure 1.1). The rate of gas transfer corresponds

to the gas flux at the water interface which is fully governed by molecular diffusion. Slightly away from the interface, turbulent gas flux tends to reduce the diffusive boundary layer thickness. This interaction between diffusion and turbulent convection gas flux determines the thickness of the concentration boundary layer and plays a vital role in air-water gas transfer process. The gas concentration boundary layer has a very small thickness δ of about $10 - 1000\mu m$ which indicates that only slightly away from the water interface molecular diffusion is entirely replaced by turbulent convection. The gas transportation process is characterized by the turbulent gas flux j, in which molecular diffusion is described by Fick's law.

$$\overrightarrow{j} = -D\nabla c, \tag{2.1}$$

where c is the gas concentration in $\mathrm{Kg/m^3}$ and D is the diffusivity in $\mathrm{m^2/s}$. The minus sign indicates that the gas flux at the surface, when the water is unsaturated, is directed downwards. The (downward) gas flux, that is studied in this work, across the flat horizontal homogeneous plane is given by

$$\overrightarrow{j} = -D \left.\frac{\partial c}{\partial z}\right|_i, \tag{2.2}$$

where the subscript i corresponds to the interface and z denotes the vertical direction. In the surface age calculations $z = 0$ at the surface and the positive z direction is downwards. In contrast, in chapter 5, discussing temperature-induced Marangoni forces at the surface, the positive z direction is pointed upwards. In all simulations, the x and y coordinates are always directed horizontally. Further below, in the water body, the

turbulent gas flux will begin to dominate the total gas flux and the equation (2.2) for the average gas flux $\overrightarrow{j}$ reads

$$\overrightarrow{j} = -D\frac{\partial \overline{c}}{\partial z} + \overline{c'w'}, \tag{2.3}$$

where $\overline{c}$ and $\overline{c'w'}$ represent the time averaged gas concentration and time averaged turbulent convection of the concentration in the z-direction respectively. Note that the c' is the concentration and w' is z-velocity fluctuation.

2.2 Gas transfer velocity K_L

The gas transfer flux is often expressed in the gas transfer velocity K_L, defined by

$$K_L = \frac{\overrightarrow{j}}{\Delta c} = \frac{\overrightarrow{j}}{c_s - c_b}, \tag{2.4}$$

where c_b represents the gas concentration in the bulk region of water and c_s is the gas concentration at the interface identified by Henry's law. The transfer processes of the low soluble gases are mainly governed by resistance on the water side. Lewis & Whitman [57] identified the mass concentration profile in a two-phase (air-water) system by a supposition of two distinct surface films, one at the air side and the other at the water side. Each distinct surface film has a mass transfer coefficient, k_a for the air (gas) phase and k_w for the water (liquid) phase. The actual mass transfer velocity

(K_L) corresponds to the individual mass transfer coefficients, defined by

$$K_L = \frac{1}{k_w} + \frac{1}{H_c k_a}, \tag{2.5}$$

where H_c represents Henry's constant which plays an important role to estimate the resistance at the water phase, which explains that when the ratio of $k_w/H_c k_a$ is large, the air (gas) phase resistance take over the transportation process. On the other hand, the resistance on the water (liquid) side controls the transportation process when the ratio is small. The value of Henry's constant H_c is inversely related to the gases that are of environmental interest such as N_2, O_2, CO, CO_2. These are very low soluble gases and thus they have a high H_c. So the conclusion is that the transfer of low soluble atmospheric gases across the air-water interface is controlled by the water phase of the interface [41].

As defined earlier, the gas exchange processes for low-diffusivity atmospheric gases are governed by a very thin gas concentration boundary layer with a standard thickness of $\delta = 10 - 1000\mu m$. This thickness is significantly influenced by the mass diffusivity D, the time scale and the turbulence intensity.

2.3 Surface age (τ)

Surface age is an important modelling parameter in the gas transfer process across the air-water interface. It is important for various applications including atmosphere-ocean gas transfer and sea surface temperature. Fluid is brought from the bulk towards the surface and stays there for a certain time before it is transported back to the bulk by

a downwelling motion. That certain time period is defined as surface age τ (see Figure 2.1). The concept of surface age was originally introduced in the "penetration model" by Higbie [34] to analyse the mass transfer across the gas-liquid interface (see section 2.4.1.1). He employed a constant surface renewal time t by assuming that the surface age τ of the liquid elements arriving at the interface is uniformly distributed. In the past, many researchers Danckwerts [14], Perlmutter [71], Koppel *et al.* [47], Chung *et al.* [12], Fan *et al.* [22], Fortescue & Pearson [23], focused their efforts on estimating the surface age τ in their proposed models.

Further improvement for the prediction of the surface age in turbulent interfacial transport was made by Kermani & Shen [44]. They directly quantified the surface age τ of fluid particles associated with surface renewal events using the hybrid Lagrangian tracking and temperature method, known as HLTT. In this method, Lagrangian particle tracking is combined with a temperature based Eulerian approach. Many researchers used the Eulerian method to calculate the fluid velocity and combine it with the Lagrangian method used to calculate the location of fluid particles. The Eulerian approach deals with concentration of fluid particles and calculates their convection and diffusion. Lai & Chen [51] adopted a Eulerian model with a Lagrangian model for indoor particle distribution and deposition. Their results shows that both models are comparable. On the other hand, some studies proves that the calculations in Lagrangian method are computationally expensive and quite more time consuming than the Eulerian method [28, 35, 70, 76, 90].

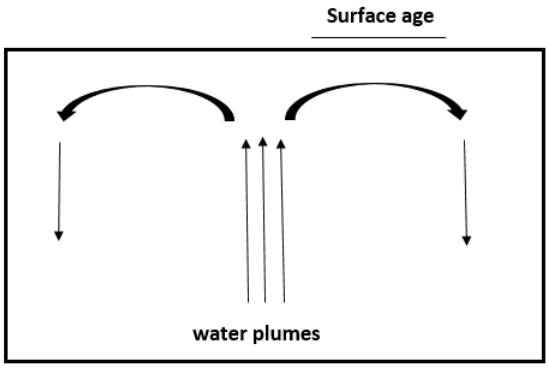

Figure 2.1: Motion of fluid parcels

The present study focuses on the estimation of surface age. To investigate this problem, data from a series of direct numerical simulations (DNS) [32] is used to elucidate the mechanisms that play an important role in the gas transport across the air-water interface. Each of the DNS stored a sequence of snapshots of the velocity field in a horizontal plane at the surface. Using the data from this plane the three-dimensional velocity field in the upper part of the concentration boundary layer at the water side was reconstructed which was subsequently used in order to estimate the surface age using a Lagrangian method to track point particles and the continuum method by introducing a continuous surface age density (see Chapter 3 & 4).

2.4 Gas transfer models

The significance of the gas transfer process across the air-water interface is defined in the previous section. To understand the actual mechanism of the gas transfer process, the quantification of only the gas transfer velocity K_L is not sufficient and it is required

to explain the total mass flux in Eq. 2.3. Previously, due to the complexity of performing measurements inside the ultra-thin gas concentration boundary layer, many researchers focused on the physical mechanism of the gas exchange process using transfer models and established several statistical relations between K_L and measurable flow parameters.

Gas transfer models can be classified into three set of classes that are discussed in the following:

1. Conceptual models;
2. Hydrodynamic models;
3. Eddy diffusivity models.

2.4.1 Conceptual models

Efforts have been made to explain the transfer velocity K_L with conceptual models. "Conceptual models are simple solutions of the vertically one-dimensional diffusion equation without any explicit advection flow field. The effect of turbulence is incorporated through initial conditions and boundary conditions, which are characterized by time and spatial scales" Brumley & Jirka [10]. Some of the models are detailed below:

2.4.1.1 Film model

Lewis & Whitman [57] developed the very first conceptual model named as the "film model". They supposed the existence of stagnant films that are located on each side of the interface, where only molecular diffusion occurs. Gas transfer was defined by

the stagnant film thickness and the gas concentration in the bulk of the water body was supposed to be constant corresponding to the fully mixed situation. It is noted that this model actually oversimplifies the complexity of transport mechanism, where a stagnant film was not physically present but a region was assumed in which the gas transfer was governed by the molecular diffusion.

The actual purpose of development of this model was to estimate the relation between the resistance of the gas-phase and the liquid-phase for different atmospheric gases with varying solubilities in water. This leads to the following relation between K_L and the stagnant film thickness δ (m),

$$K_L = \frac{D}{\delta} \text{ m}/s, \tag{2.6}$$

where D (m^2/s) is the molecular diffusivity. This model appeared to be a good estimate for transport processes where molecular diffusion is dominant. However, in experimental studies, it was noted that the relation between transfer velocity K_L and D was not linear [63].

2.4.1.2 Penetration model

A refined model was developed by Higbie [34] that takes surface renewal effects into account. He acknowledged the existence of the turbulence that plays a vital role in the bulk region of the liquid by bringing up fresh packages of unsaturated liquid (and replacing the saturated liquid) to the surface. This gas transfer occurs for a certain renewal time T_r by assuming that the surface age τ of the liquid elements arriving at

the interface is uniformly distributed. Higbie derived the relation

$$K_L = \sqrt{\frac{D}{\pi T_r}}. \tag{2.7}$$

2.4.1.3 Surface renewal model

Danckwerts [14] improved the penetration model with the concept of surface renewal rate r. For this he made two assumption. The first one was that all fluid parcels at the surface have equal probability of being replaced by fresh fluid from the bulk of fluid body, independent of their surface age τ. Therefore, the probability density function of the surface age τ is the exponential distribution. The second assumption made by Danckwerts was that the diffusion is the only transport mechanism at the interface, this was originally assumed by Higbie. Hence, the surface renewal model following the exponential distribution of the surface age so that the t is no longer constant, expressed by

$$K_L = \sqrt{Dr} \ \ \mathrm{m}/s, \tag{2.8}$$

where $1/r$ may be interpreted as average time between surface renewal events and has to be determined by performing experiments. The prediction of gas transfer across the air-water interface has improved by both of these models. Following that, the relation between the K_L and D was formed by using penetration and surface renewal models and expressed by

$$K_L = D^n \ \ \mathrm{m}/s, \tag{2.9}$$

where n is the power of diffusivity and its value depends on surface dynamics conditions ranging between $n = 1/2 - 2/3$ [39]. A surface renewal model was found to be a significant improvement compared to the film model [38, 87].

2.4.1.4 Film-renewal model

O'Connor & Dobbins [69] proposed a film-renewal model by combining the film model and the penetration model, thereby assuming the existence of a liquid film at the interface in which liquid elements are continuously replaced by a fresh liquid from the bulk of the liquid body. This assumption leads to the expression

$$K_L = \sqrt{Dr} \coth\left(\frac{\delta}{\sqrt{D/r}}\right) \text{ m}/s. \tag{2.10}$$

The above expression is asymptotic to the surface renewal model for large r values and the film model for small r values.

2.4.1.5 Random eddy model

This model was developed by Harriott [29]. He proposed that the gas transport mechanism is enhanced by the turbulent eddies even though they do not reach the interface. These turbulent eddies have a random lifespan and will approach the interface within some random distance. The only transport mechanism considered is molecular diffusion from this random distance up to the interface. He derived

$$K_L = \frac{\sqrt{Dr}}{1 + \delta\sqrt{D/r}} \text{ m}/s. \tag{2.11}$$

2.4.1.6 Surface divergence model

McCready *et al.* [63] presented the surface divergence model. It was related to the horizontally averaged gas transfer velocity K_L to the horizontal velocity field at the interface. The divergence of this horizontal velocity field observed at the interface is given by

$$w_i = -\left(\frac{\partial u_i}{\partial x} + \frac{\partial v_i}{\partial y}\right) z = -\beta z, \tag{2.12}$$

where u_i, v_i, w_i are the velocities near the interface in x, y, z-direction, respectively. The expression in parenthesis is known as 'surface divergence' strength and tagged as β for convenience. Hence, the model is called surface divergence model (SDM) which leads to the expression

$$K_L = c\sqrt{D\beta'}. \tag{2.13}$$

The root mean square (rms) of the surface divergence β' can be theoretically approximated for simple problems. This approximation was adopted by Brumley & Jirka [11].

The conceptual model shows that transfer velocity K_L is dependent on $\sqrt{D}$. In spite of that, the gas transport process is influenced by the hydrodynamics, which is still unseen in the term r. In this study, the numerical results enable estimation of the fraction r in terms of surface age τ.

2.4.2 Hydrodynamic models

Several researchers presented conceptual models which focused on the relation between the term r and the considerable diversity of turbulent flow parameters. The advection-

diffusion equation is used in hydrodynamic models under the assumption of a single flow pattern.

2.4.2.1 Large-eddy model

Fortescue & Pearson [23] proposed the large-eddy model by elaborating the surface renewal model. They make the assumption that the gas transport process is dominated due to the large turbulent eddies. Therefore, the term r can be determined by velocity rms of large eddies and integral length scale ${u'}_L/L$. The advection-diffusion equation of a steady roll cell was solved numerically resulting in the expression

$$K_L = a\sqrt{\frac{D\,.\,{u'}_L}{L}}, \tag{2.14}$$

where L is the turbulent integral length, ${u'}_L$ is the root mean square of the turbulent fluctuations and a is a constant with a value of 1.46.

2.4.2.2 Small-eddy model

The small-eddy model was presented by Banerjee & Scott [7] and Lamont & Scott [53]. They assumed that the gas transport process is dominated by the small turbulent eddies. These small turbulent eddies have a mean turnover time scale determined by the Kolmogorov time scale. Therefore, the parameter r can be estimated by $(\epsilon/\nu)^{1/2}$. Where ϵ is the rate of turbulent energy dissipation close to the surface and ν is the kinematic viscosity. This leads to a relation

$$K_L = b\sqrt{D}\,\left[\frac{\epsilon}{\nu}\right]^{1/4}, \tag{2.15}$$

the constant b has a value of 0.4 according to Lamont & Scott [53].

Note that large-eddy model and small-eddy model predicted quite different dependencies of K_L on the turbulent Reynolds numbers. A detailed explanation provided by Theofanous *et al.* [85] resolved this discrepancy between these two models by pointing out that large turbulent eddies are dominant for the mass transfer mechanism using a low turbulent Reynolds numbers as in the experiments of Fortescue & Pearson. Whereas in Banerjee *et al.* and Lamont & Scott experiments, a high Reynolds numbers was used for which mass transfer mechanism is controlled by small eddies.

A dimensional analysis can better explain the estimation of r by the expression $(\epsilon/\nu)^{1/2}$. The rate of energy dissipation per unit mass (ϵ) has dimension (m^2/s^3) and viscosity (ν) has (m^2/s).

Dimensional analysis: $[\epsilon] = m^2 s^{-3}$; $[\nu] = m^2 s^{-1}$

$$\left[\frac{\epsilon}{\nu}\right]^{1/2} = \frac{m^2 s^{-3}}{m^2 s^{-1}} = s^{-1}, \tag{2.16}$$

where (s^{-1}) is the dimension of r.

2.4.3 Eddy diffusivity models

Contrarily, in the above stated models, only one turbulence scale was assumed to be dominant in transport mechanism. The eddy diffusivity models, instead, were supposed to be multi-scale where the dominating scales fluctuate with depth. "Using eddy diffusivity closure to relate the transport to the mean concentration gradient, they provide a single description for the entire turbulent field and so avoid the need for any artifi-

cial, sharp boundaries or sudden renewal events" Brumley & Jirka [10]. Generally, the supposition behind the eddy diffusivity model was that the sum of turbulent diffusion D_t and molecular diffusion D_m together gives the total diffusivity F_T. This yields the following relation

$$F_T = D_m + D_t, \tag{2.17}$$

where D_t fluctuates with depth and follows a power dependency $D_t = \alpha z^n$, α is defines as a constant and n ranges between 2 and ∞ for D reliance. By integrating the inverse of the total diffusivity $(1/F_T)$ to ∞ depth provides

$$K_L = (n/\pi)\sin(\pi/n)\,\alpha^{(1/n)}\,D^{1-1/n}. \tag{2.18}$$

The prediction of power dependency is $n = 2$ according to Son & Hanratty [81]. Their result, shows that the transfer velocity is directly proportional to $\sqrt{D}$ leading to identical results as the surface renewal model. Alternatively, when the power dependency is $n = \infty$, this model shows identical results to Lewis & Whitman [57] (Film model).

2.5 Numerical analysis of scalar transport mechanism

The gas and heat transport problem are problems that deal with scalar transport. The heat and gas transport mechanisms are assumed to be dominated by diffusion and convection while neglacting evaporation and radiation. The only difference is that the Prandtl number (Pr) is the ratio of kinematic viscosity ν and thermal diffusivity

α. On the other hand, Schmidt number (Sc) is the ratio of kinematic viscosity ν and mass diffusivity D. In the literature, different terms are used depending on the conditions and the focus of the proposed particular research. The 'mass/heat transfer' terms are frequently used in literature in which the primary focus is based on fluid dynamics. Alternatively, a wider term 'scalar transfer' is used in papers that focus more on numerics. During the review of research papers, it is important to recognize that either terminology explains the same problem or there is a comparison between Sc and Pr. To date, numerous numerical simulations of scalar transport at the air-water interface have been performed. There have been more simulations on heat transfer than on mass transfer, as heat transfer takes a vital role in industrial applications.

There are three main sources to generate turbulence in the environment i.e. buoyant convectively driven turbulence, wind-shear induced turbulence and bottom-shear induced turbulence (see Figure 1.1). Several researchers have investigated the interaction between the gas transfer mechanism using the different turbulence generation methods. The studies focused on these three turbulent conditions are briefly summarized in the following sections.

2.5.1 Buoyant convectively induced turbulence

Buoyancy-driven flows are present in our everyday life on different scales, from a very small range such as in the cooling of electronic micro-chips, to a very large scale such as the natural convection in the atmosphere. Whereas the difference in fluid density is significantly high, fluid with lower density will start to rise up and fluid with high density will start to descend, respectively.

A basic problem in fluid dynamics that has been thoroughly investigated is the Rayleigh-Bénard convection (RB convection). It is the type of natural convection that occurs when a horizontal layer of the fluid is heated from below and cooled from above. Several aspects of the turbulent RB covection problem has been reviewed by Ahlers *et al.* [1]. In this review they elucidate the dependence of Nusselt and Reynolds number on the Reyleigh and Prandtl number. Many researchers investigated RB convection using a range of Prandtl number and Rayleigh number [5, 13, 16, 17, 18, 25, 45, 86].

Turbulence was measured in an oceanic convective mixed layer during a cold-air outbreak by Shay & Gregg [77] in the upper ocean. They established a relationship between the turbulent dissipation rate and the surface buoyancy flux. Subsequently, Shay & Gregg [78] studied a buoyant convective instability near the Bahamas that was generated by daytime heating and evaporative cooling at night. The plumes generated by the convective instability were observed to penetrate up to 100m deep. The relation between buoyancy induced turbulence and sea surface temperature was studied by Graham & Barnett [24]. They found that for large scale deep penetrative (buoyant) convection to take place in the Indian and Pacific oceans, it is needed that the water surface temperature exceeds $27.5\,^0$C. Further increases in sea surface temperature, however, did not produce any additional effect. Sea surface temperature was associated between convection and surface wind divergence. This study [24] was conducted and according to their results, sea surface temperature is not necessary to be over $27.5\,^0$C for very effective convection although wind divergence is quite related with deep convection. Similar studies were performed in a lake environment by Imberger [36]. Other researchers studying buoyancy convective instability driven turbulent convection

in lakes were Brubaker [9], Sander *et al.* [74] and Jonas *et al.* [43]. The turbulent transport model of Zeman & Lumley [93] was also concerned with buoyancy instability effects on the vertical flux through the mixed layer. However, none of the above works really addresses the convective transfer of atmospheric gases by the buoyant convective instability. Macintyre et al. [61] expanded the scope of the research into penetrative (buoyant) convection by including investigation into the gas transfer coefficients due to wind shear and penetrative convection through the mixed layer. Many researchers investigated the gas exchange across the atmosphere and the surface via a buoyant convective instability by using various models [2, 21, 55, 75]

The gas transfer process is dominant by buoyant-induced turbulence at low wind speed and driven by temperature differences between the surface (cold) and the bulk (warm). To investigate the effectiveness of this process in more detail, Wissink & Herlina [92] performed DNS to calculate gas and heat transfer into the water governed by buoyant-convective instability.

2.5.2 Wind-shear turbulence

Wind-shear induced turbulence is an important mechanism to promote the air-water gas transfer. Wind shear is generated in the vicinity of the interfacial layer. The turbulence induced by wind causes quick mixing and enhances the gas and heat transfer. Wind speed above 3 m/s induce considerable wave growth which may enhance the gas exchange process. Merlivat & Memery [65] studied the gas transfer velocity which linearly changes with friction velocity ranges between $3 - 9$ m/s. The similar results were found by Jähne & Haußecker [37], which confirmed that the gas transfer velocity

K_L is not only a function of wind speed but also a function of the surface friction velocity.

Many researchers extended the complexity of the scalar transport process across the air-water interface by establishing the deformation of the interface produced by wind. The wave generation and the turbulence processes of the sheared deformable interface made it necessary to use more complicated numerical techniques. The studies of Lombardi *et al.* [60] and Angelis *et al.* [15] show that in the case of deformable interface the appearance of waves adds a new source of motion to the gas phase that effects the transport process in the liquid phase. Lombardi *et al.* [60] carried out a direct numerical simulation (DNS) of coupled gas-liquid interface flows over a flat surface. They investigated that the gas-liquid interface generated at the gas side was almost like a rigid wall, while the liquid side of the interface is like a slip surface. Angelis *et al.* [15] presented the turbulent flow over the wavy wall. According to their results, high-frequency waves exert significant impact on the turbulence and average flow characteristics. Kunugi *et al.* [50] performed a direct numerical simulation (DNS) for the turbulent flow over a freely deformable interface with wind-shear studying the carbon-dioxide gas absorption. To evaluate the gas solubility, Henry's law was applied and they concluded that the carbon-dioxide gas exchange coefficient at the turbulent free surface was in good agreement with existing experimental data.

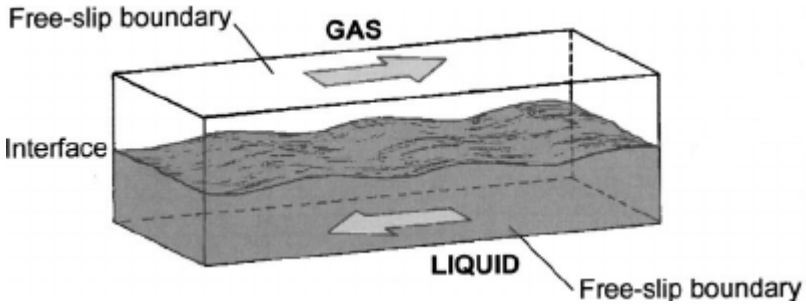

Figure 2.2: Two-phase flow for sheared wavy interface [52].

Finally, a direct numerical simulation of turbulent heat transfer across a mobile, sheared gas-liquid interface was carried out by Lakehal *et al.* [52]. They found that the scalar transport process across the gas-liquid interface was only slightly affected by high-frequency fluctuating fields. The computational setup includes a liquid and a gas phase that flow in opposite directions with a deformable wavy gas-liquid interface as shown in Fig. 2.2 (this picture is taken from the Lakehal paper). Their analysis was limited to the gas side. The effect of Prandtl numbers of $Pr = 1, 5$ and 10 on the thermal field were investigated.

2.5.3 Bottom-shear turbulence

Bottom-shear induced turbulence become dominant and governed the gas transfer process, when wind speeds are quite weak in stream environment. Many researchers presented the relation between gas transfer velocity and flow parameters. These relations are usually based on numerical analysis or experimental investigations [20, 84, 27]. The previously mentioned researchers used empirical methods to obtain gas transfer relations, while a semi-empirical method was used by O'Conner & Dobbins [69].

The re-aeration of open channel flow was studied by Plate & Friedrick [72]. They evaluated various turbulent conditions, namely bottom-shear induced turbulence, wind-shear induced turbulence and the combination of bottom and wind-shear induced turbulence. They introduced a relation of gas transfer velocity K_L as a function of root mean square of the horizontal component of the velocity near the interface. Many researchers performed experiments to relate the gas transfer process in an open channel flow and studied the effect of different surface roughness elements [68, 42, 66, 67]. They found that rate of gas transport agreed with macro-roughness and only the small eddy model is valid for small roughness elements.

Atmane & George [3] directly quantified the bottom-shear induced turbulent mass flux using the eddy-correlation method. The measurements of gas transfer in a tank with grid-stirred turbulence was studied by McKenna & McGillis [64]. They carried out the experiments with various levels of contamination at the surface. They found that the bulk turbulence is unaffected due to the presence of surface films. They determined a relation between the surface divergence and the gas transfer velocity for the case of interfacial contamination. It appeared that the surface divergence is an important parameter for gas transport process (see Brumley [10]). Tamburrino & Gulliver [83] also investigated the relation between the mass transfer in an open channel flow and a free surface turbulence. This study was performed at various Re numbers in the range $8,500 - 45,00$.

Suga and Kubo [82] presented an extended version of the analytical wall-function (AWF) which was developed for Reynolds averaged Navier Stokes simulation to estimate the concentration of turbulent fields and the rate of mas transfer across the

undeformable gas-liquid interface for different values of Schmidt number ranging from $1 \leq Sc \leq 1000$.

2.6 WENO schemes

Weighted essentially non-oscillatory (WENO) schemes have become a very popular approach in a large field of applications, especially in computational fluid dynamics. The first WENO scheme was developed in 1994 by Liu *et al.* [58]. They considered a convex combination of various sub-stencils for the calculation of the mass flux at the grid cell to construct an 'optimum' calculation of the mass flux using nonlinear weights. The main contribution of this scheme was the construction of nonlinear weights using smoothness indicators (SIs) for sub-stencils. Later, various researchers developed a huge variety of WENO schemes. A lot of improvements have been carried out to improve the accuracy of WENO schemes by modifying the SIs. Jiang and Shu [40] introduced WENO-JS scheme and proposed a local SI for the estimation of nonlinear weights. They developed WENO$(2r-1)^{th}$ - order accuracy of the scheme for various stencil sizes $r = 2$ (WENO3) and $r = 3$ (WENO5). Subsequently, Balsara and Shu [6] further extended the WENO scheme up to eleventh-order accuracy. Henrick *et al.* discovered a sufficient condition that the nonlinear weights proposed by Jiang and Shu [40] failed to recover the high order accuracy at critical points where the first-order derivative is zero. They realized that the WENO scheme needed to have an accurate parameter ϵ for the calculation of nonlinear weights. To solve this problem, they introduced a new WENO-M scheme (mapped WENO). This scheme has a fifth-order accuracy in smooth regions as well as critical points. Another approach was discovered by the Borges *et al.*

[8]. They introduced the WENO-Z scheme that has the same order of accuracy as the WENO-M scheme but with less computational cost. They used a different approach to calculate the weights by introducing a global smoothness indicator (GSI) ζ. A brief review of WENO schemes are explained below.

Consider the scalar conservative law equation,

$$\frac{\partial u}{\partial t} + \frac{\partial f(u)}{\partial x} = 0. \tag{2.19}$$

Given a 1D mesh with points $x_i = i\Delta x$, $i = 0, ..., N$, where Δx is the uniform grid space [30, 8], using finite differences, Eq. 2.19 can be defined by

$$\frac{du_i}{dt} = -\frac{\hat{f}_{i+1/2} - \hat{f}_{i-1/2}}{\Delta x} + (\Delta x)^2, \tag{2.20}$$

where the terms $\hat{f}_{i\pm1/2}$ are numerical fluxes.The flux of the 5^{th}-order WENo-JS [40] scheme is defined by $\hat{f}_{i+1/2} = \sum_{k=0}^{2} \omega_k q_k$, where q_k is the 3^{rd}-order flux on the sub-stencil $S_k = (i+k-2, i+k-1, i+k)$. The weight function defined by Jiang and Shu [40] is given by

$$\omega_k^{js} = \frac{\alpha_k}{\alpha_0 + \alpha_1 + \alpha_2}, \tag{2.21}$$

where

$$\alpha_k = \frac{c_k}{(IS_k + \epsilon)^2}, \quad k = 0, 1, 2, \tag{2.22}$$

IS_k is the local smoothness indicator used to measure the smoothness of a solution on sub-stencils S_k. c_k $(k = 0, 1, 2)$ are the optimal weights with $c_0 = 0.1, c_1 = 0.6$ and $c_2 = 0.3$ that generate a 5^{th}-order accurate upstream schem and ϵ is a small positive

real number needed to avoid the denominator becoming zero. Note that ω_k are the normalized weights whereas α_k are not normalized. In the 5^{th}-order WENO-Z scheme presented by Borges *et al.* [8] a global smoothness indicator ζ was used to calculate the weight function,

$$\omega_k^z = \frac{\alpha_k}{\alpha_0 + \alpha_1 + \alpha_2}, \tag{2.23}$$

where

$$\alpha_k = c_k \left(1 + (\frac{\zeta_5}{IS_k + \epsilon})^q\right). \tag{2.24}$$

The global smoothness indicator in [8] reads $\zeta_5 = |IS_2 - IS_0|$. Where q is an adjustable parameter. If $q = 1$, 4^{th}-order accuracy is obtained. While for $q = 2$ the accuracy is 5^{th}-order [8]. Borges *et al.* pointed out that, to gain the required accuracy for a solution containing discontinuities, reducing q was benificial to obtain a more accurate solution at critical points. Therefore, $q = 1$ was proposed for the WENO-Z scheme in [8].

2.7 Surface film effects

2.7.1 Surface tension

Surface tension is a property of the fluid that allows it to resist external forces, because of the cohesive nature of the fluid molecules. The surface tension of water (as compared to other fluids) is quite large, for instance, for water at $20\,^0$C a value of 7.28×10^{-2} N/m is obtained.

Surface tension is also responsible for the shape of bubbles and liquid droplets. Water droplets tend to be pulled into a spherical shape by the cohesive forces of the

surface and due to its shape, surface tension is identical at every surface location. Surface tension is usually represented by σ and it is expressed as a force F (Newton) exerted parallel to the surface of a liquid divided by the length L (metre) of the line over which the force acts:

$$\sigma = F/L \tag{2.25}$$

Surface tension also depends on physical fluid properties, for instance its temperature (see Sabersky *et al.* [73]). Several experiments were performed by Lapham *et al.* [54] for the determination of surface tension. For instance, the situtensiometry technique was used to determine surface tension by the retraction of a thin-walled tube through the fluid surface. Successive repeatable results were achieved by measuring the surface tension of water with various quantities of alcohol and surfactants added.

2.7.2 Marangoni effect

Marangoni effects occur when surface tension is no longer constant due to differences in e.g. temperature or concentration along the surface. Such differences in surface tension may induce flow. For instance, when the surface tension gradient is produced by variations in temperature, the induced flow is usually known as thermocapillary flow (or thermal Marangoni effects). Whereas, when the surface tension gradient is produced by local differences changes in solute concentration, the resultant phenomenon is known as solute Marangoni effects, e.g., 'tears of wine'. In the present study, the (horizontal) surface tension gradient was generated due to a buoyant instability generated by an unstable vertical surface temperature gradient.

Chapter 3

Lagrangian approach

In this chapter, the Lagrangian particle tracking method is described, which is used to calculate the mean surface age ($\overline{\tau}$). Subsequently, Dankwert's model [14]. Apart from that, also the reconstruction of the three-dimensional velocity field adjacent to the surface from the two-dimensional DNS-generated velocity field at the surface is discussed. Finally, a time-step-reduction study and a particle-density-refinement study is carried out in order to obtain a time-step and particle-density independent approximation of the mean surface age.

3.1 Lagrangian Modelling

A Lagrangian particle tracking technique is used to estimated the mean surface age $\overline{\tau}$. In the literature, various simple theories for the surface age distribution have been proposed. They have been widely used in many applications involving interfacial gas transfer problems. In the present study, the surface renewal theory by Danckwerts [14]

is used to calculate the gas transfer velocity K_L using the mean surface age $\overline{\tau}$. Surface age is a critical parameter for the determination of turbulent interfacial gas transfer that plays an important role in various applications including atmosphere-ocean gas transfer. Gas transport in the upper ocean is controlled by the interplay of molecular diffusion at the interface and turbulent mixing underneath. The hydrodynamic processes of upwelling and downwelling motions in the water phase play an important role in the gas transport near the interface. The upwelling increases interfacial gas transport by replacing saturated fluid close to the interface with fresh, unsaturated fluid from the bulk.

Danckwerts [14] made two assumptions in his surface renewal model. His first assumption was that all fluid particles at the surface have an equal probability of being renewed by fresh fluid elements from the water bulk, independent of their surface age τ. Therefore, the probability density function of the surface age τ is the exponential distribution. The second assumption was that the diffusion is the only transport mechanism at the interface. This model is used in the present study to calculate the gas transfer velocity K_L.

Velocity field snapshots (Table 3.2) stored at the surface are used to calculate the gas transfer velocity (K_L), these snapshots contain the 2-dimensional velocity fields, produced by the direct numerical simulations (DNS) [32, 92]. These DNS were based on experiments performed at KIT by Jirka & Herlina and co-workers (see e.g. [41]) in Karlsruhe, Germany. In the DNS, the mass transfer across the air-water interface was simulated using various computational domains and meshes as detailed in Table 3.1. Only the water phase was simulated, the presence of air above the wa-

ter surface was modeled by assuming that the water at the top of the computational domain was fully saturated with atmospheric gases. In the horizontal directions, periodic boundary conditions were employed while at the bottom of the computational domain symmetry boundary conditions were employed. In the simulations a time step of $10^{-4}L/U$ time units was used and the simulations were run for at least a 100 time units in order to obtain a quasi-steady state. Two different sources were used to produce turbulence, bottom-shear induced turbulence was used in BT10 and BT20 while buoyant-convectively induced turbulence was used in BY10 and BY20, see Table 3.1. For the bottom-shear induced turbulence-driven flow, simulations were conducted for five different Schmidt numbers (2, 4, 8, 16 and 32). Two turbulent Reynolds numbers $R_T = 195$ and $R_T = 507$ (see Eq. 1.7) were solved, using computational domain sizes of 5L ×5L ×3L and 20L ×20L ×5L, respectively. The characteristic length scale L and velocity scale U were typically set to 0.01 m and 0.06m/s, respectively, because the kinematic viscosity in the BT10 and BT20 simulations was $\nu = 10^{-6}$ m^2/s. For buoyant-convectively induced turbulence-driven flow, the Prandtl number was set to $Pr = 6$ for water at 298.15 K. The non-dimensionalization was carried out using $L = 0.01$ m and $U = 0.01$ m/s. Table 3.2 shows the time of the velocity field snapshots used in the K_L calculations.

Table 3.1: Overview of the simulations. A structured (Cartesian) mesh was used to resolve the water phase.

Simulation	Sc	Domain ($\Delta x \times \Delta y \times \Delta z$)	Number of nodes
BT10	2-32	5L × 5L × 3L	128 × 128 × 212
BT20	2-32	20L × 20L × 5L	512 × 512 × 300
BY10	20, 500	10L × 10L × 10L	800 × 800 × 512
BY20	7, 16	30L × 30L × 30L	2400 × 2400 × 1520

Table 3.2: Times of the velocity field snapshots used to calculate K_L

Simulation	Times of the velocity field snapshots (s)
BT10	16.7, 20.04, 23.38, 26.72, 30.06, 33.4, 36.74, 40.08
BT20	28.39, 31.73, 35.07, 38.41, 41.75, 45.09
BY10	50, 60, 70, 80, 90, 100, 110, 120
BY20	40, 45, 50, 55, 60, 65, 70, 75

3.1.1 Reconstruction of 3D velocity field adjacent to the surface

The DNS calculations [92] produced time-sequences of snapshots at the interface containing the local horizontal velocity field $u^*(x, y)$, $v^*(x, y)$ as well as the normal derivative of the vertical velocity $\partial w^*/\partial z(x, y)$, where u^* and v^* are the normalised velocities in the x and y directions, respectively and w^* is the velocity in the vertical, z, direction. Note that $z = 0$ coincides with the air-water interface and $z > 0$ is directed downwards. The time-interval between the recorded subsequent snapshots is relatively large, while also the time period over which snapshots are available was too small to be able to

approximate a time-accurate velocity field. Hence, to approximate the mean surface age, it was assumed that the velocity field was frozen in time. In the DNS, the incompressible Navier-Stokes equations were solved to determine the flow field, together with upto five convection diffusion equations for scalar transport. Periodic boundary conditions were employed in the horizontal directions for all variables. At the bottom of the computational domain either free-slip boundary conditions (for the buoyant-convective simulations BY10 and BY20) or turbulent fluctuations were copied from a concurrently running large-eddy simulation of isotropic turbulence in a periodic box (simulations BT10 and BT20). For BY10 and BY20 a fixed, low temperature (lower than the temperature in the bulk) was prescribed at the interface. While in all simulations a free-slip boundary condition for the velocity was employed. For more detailed information on the setup of the DNS performed see [32, 33, 92]. The free-slip boundary condition for the velocity at the top were exploited below to reconstruct the 3D velocity fields for $z > 0$ as used in the present calculations.

The 2D time-sequences $(u^*, v^*, \partial w^*/\partial z)$ stored at the interface in the DNS were used to reconstruct the 3D velocity fields in a thin region adjacent to the surface. This reconstruction was based on the boundary conditions used in the DNS, where $\partial u/\partial z = \partial v/\partial z = w = 0$ combined with the continuity equation. From this it was derived that in a small region below the surface, u and v are virtually independent of z, while w scales linearly with z such that

$$\begin{cases} u(x,y,z) &= u^*(x,y) \\ v(x,y,z) &= v^*(x,y) \\ w(x,y,z) &= z\ \frac{\partial w^*}{\partial z}\big|_i \end{cases}, \tag{3.1}$$

where the subscript i denotes the interface and the velocity field is assumed to be frozen in time. This reconstruction of the 3D velocity fields was needed as only 2D velocity fields were stored at the interface in the DNS and to be able to track particles moving up towards the interface and subsequently down towards the bulk, a 3D velocity field is needed. Also, this has the added bonus that the method discussed here can also be employed using measurements of 2D interfacial velocity fields as input in order to assess the mean surface age. Calculations of the mean surface age were performed both forward and backward in time. The latter has the advantage that the area with downward moving flow tends to be smaller than the area with flow moving upwards, such that when using a particle-based method (see 3.1.2) significant computing time can be saved.

3.1.2 Lagrangian method

In the Lagrangian particle-based method, both the basic Euler method (single-step) and the second order Adams-Bashforth method have been used to calculate the particle path given an initial location in space (x_0, y_0, z_0) under the influence of the reconstructed 3D velocity field $[u(x,y,z), v(x,y,z), w(x,y,z)]$ given in Eq. 3.1. The particle path is described by:

$$\begin{cases} x(t_{k+1}) &= x(t_k) + \int_{t_k}^{t^{k+1}} u(x(t), y(t), z(t))dt \\ y(t_{k+1}) &= y(t_k) + \int_{t_k}^{t^{k+1}} v(x(t), y(t), z(t))dt \\ z(t_{k+1}) &= z(t_k) + \int_{t_k}^{t^{k+1}} w(x(t), y(t), z(t))dt \end{cases} \tag{3.2}$$

Time integration algorithms employed here are based on finite difference methods [56] and the (constant) time step $dt = t_{k+1} - t_k$ is defined as the distance between consecutive points in time. Due to the low accuracy of the Euler method, defined by

$$\begin{cases} x(t_{k+1}) &= x(t_k) + dt \times u(x(t_k), y(t_k), z(t_k)) \\ y(t_{k+1}) &= y(t_k) + dt \times v(x(t_k), y(t_k), z(t_k)) \\ z(t_{k+1}) &= z(t_k) + dt \times w(x(t_k), y(t_k), z(t_k)) \end{cases}, \tag{3.3}$$

a very small time step is needed to obtain an accurate approximation of the surface age τ so that it takes a lot of time to complete a simulation. As explained in more detail later, the particle surface age τ is defined by the time it takes for a particle originating at z_0 (moving initially upwards to the surface) to return to its original location. Therefore, as an alternative, the second-order-accurate Adams-Bashforth method (two-step) is used to get better results using approximations at two subsequent time steps. This method is defined by:

$$\begin{cases} x(t_{k+1}) &= x(t_k) + \frac{dt}{2}\left[3u(x(t_k), y(t_k), z(t_k)) - u(x(t_{k-1}), y(t_{k-1}), z(t_{k-1}))\right] \\ y(t_{k+1}) &= y(t_k) + \frac{dt}{2}\left[3v(x(t_k), y(t_k), z(t_k)) - v(x(t_{k-1}), y(t_{k-1}), z(t_{k-1}))\right] \\ z(t_{k+1}) &= z(t_k) + \frac{dt}{2}\left[3w(x(t_k), y(t_k), z(t_k)) - w(x(t_{k-1}), y(t_{k-1}), z(t_{k-1}))\right] \end{cases} \tag{3.4}$$

If not stated otherwise all times (like surface age and time-step) were non-dimensionalised using L/U. Where L/U depends on the simulation, i.e. $L/U = 1$s for BY10 and BY20, and $L/U = 1/6$s for BT10 and BT20.

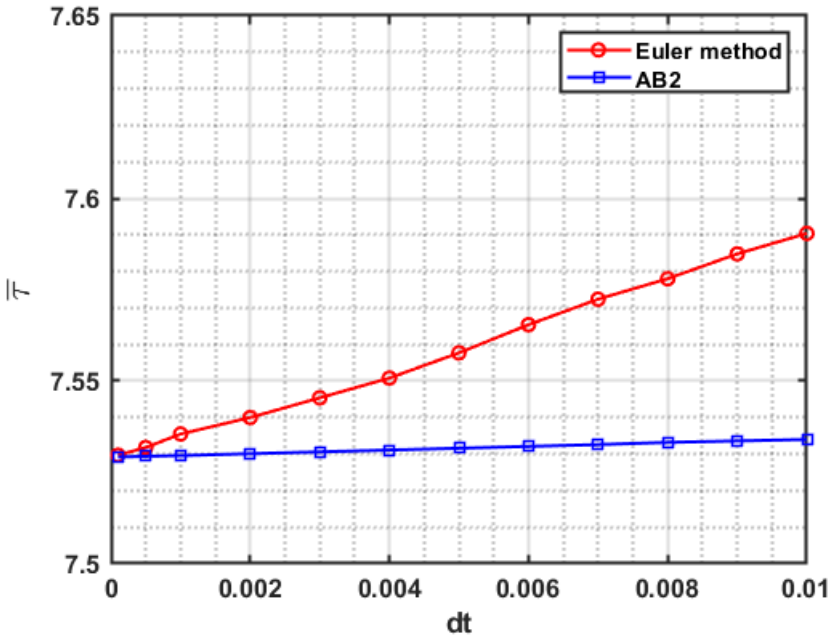

Figure 3.1: Time-step sensitivity study for BT10 simulation comparing first order Euler method to second order Adams-bashforth AB2 method at time $t = 16.7$ s. See Tables 3.1 and 3.2

Various calculations were performed for different time steps using both methods (Euler and AB2) to compare the results. Figure 3.1 shows the variation of mean surface age against time step. The red-line with circular marker shows the results obtained by the Euler method and the blue-line with square marker was obtained using the second-order-accurate Adams-Bashforth AB2 method. It can be clearly seen that the surface age obtained using the Adams-Bashforth method is significantly more accurate than the surface age obtained with Euler, even when using a relatively large time step.

In the Lagrangian method, N massless point particles (that move along with the fluid flow) are introduced uniformly distributed in the plane $z = z_0$. Where $z = z_0$ identifies the plane located somewhere in the area where the velocity field was recon-

structed. Note that the results are independent of actual location of this plane. For the forward calculations particles are only activated when their initial w velocity is negative (upward flow) and vice versa for the backward calculations. The surface age of each particle is determined by integrating the particle path in time using the second-order Adams-Bashforth AB2 method until the z-location, z_p, of the particle is larger than z_0. The mean surface age is then obtained by averaging the surface ages of all particles.

Figure 3.2 shows a vector plot of the (u, v) velocity field at the surface of simulation BY10 in Table 3.1. The coloured contours, representing $\partial w/\partial z$, clearly identify areas of upwelling and downwelling motions (see Figure 3.2). These upwelling and downwelling motions are especially important for the promotion of gas transportation. Typically, the downwelling motions are relatively narrow and separate large areas of upwelling motions thereby forming the footprints of convection cells.

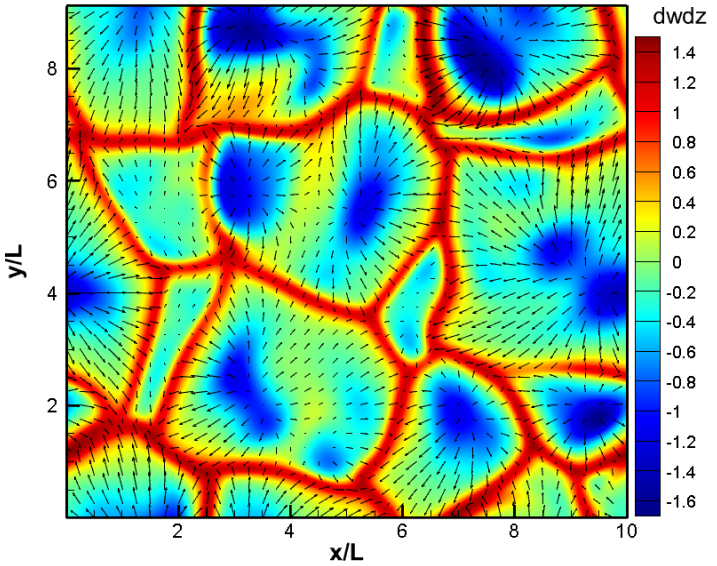

(a) $t = 50$ s

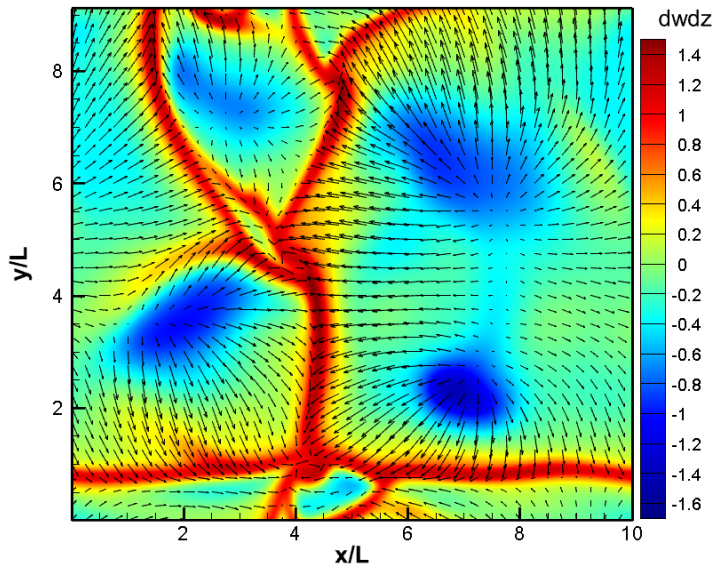

(b) $t = 100$ s

Figure 3.2: Horizontal velocity vectors and magnitude (contours), representing $\partial w/\partial z$, at the interface of BY10 simulation at $t = 50$ s and $t = 100$ s

Figure 3.2a represents $\partial w/\partial z$, a clear picture of several strong upwellings (blue) with

red downwelling areas where flow plunges down at $t = 50$ s. Fifty seconds later the upwellings become weaker as convection cells merge so that the average size of these cells increases (see Figure 3.2b). With the passage of time, the average size of the upwelling regions becomes almost constant even though their locations and shapes continuously change. The significant changes in size, shape and location of the convection cells are typical for the early stages of an evolving buoyant instability that was simulated in the corresponding DNS [32].

3.2 Weighted/Non-weighted $\overline{\tau}$

The two ways in which the mean surface age was determined are explained, assuming forward calculations in time. In the weighted mean surface age $\overline{\tau}$ calculation, each particle is given a weight equal to its (upward) velocity which is proportional to the local particle flux. In the non-weighted method, all weights are the same (as long as the initial velocity is upward). For the weighted method, initially at $t = 0$ s each particle $p(0)$ is given a weight $\psi_{p(0)} = a w_{p(0)}$, where $w_{p(0)}$ is the initial vertical velocity of the particle and $a = 1/\sum_{p(0)} w_{p(0)}$ so that

$$\sum_{p(0)} \psi_{p(0)} = 1. \tag{3.5}$$

Note that $p(t)$ is an indicator function of time which can only be 1 (if the particle is still active) or zero (if it becomes inactive). The mean surface age $\overline{\tau}$ is subsequently

calculated from

$$\overline{\tau} = \int_{t=0}^{\infty} \sum_{p(t)} \psi_{p(0)} dt. \tag{3.6}$$

For the non-weighted method, initially at $t = 0\,s$ each active particle $p(0)$ is given the same weight $\psi_{p(0)} = a$, where $a = 1/N$ and N is the number of active particles at $t = 0$ s. For the rest, the calculation is the same as for the weighted surface age. Note that in practice the calculation of $\overline{\tau}$ is stopped as soon as $\sum_{p(t)} \psi_{p(0)} < 10^{-4}$.

3.3 Mesh refinement study

To obtain more accurate results for the mean surface age $\overline{\tau}$, a particle density refinement is carried out by increasing the density of the $N \times N$ mesh with a particle defined at each node, known as p-refinement. As shown in Figure 3.3, p-refinement relates to the increase in the number of particles in the computational domain. By increasing the number of particles, it is shown that resulting mean surface age becomes independent of particle density. It is important to note that mesh refinement not only leads to a significant reduction in errors in the surface age estimation (see Figure 3.4) but also to a significant increase in computational effort. To estimate the surface age, the velocities are interpolated onto the refined mesh using a second order interpolation. An interpolation is required for each subcell when employing a sub-mesh refinement by a factor of p= 2 (Figure 3.3).

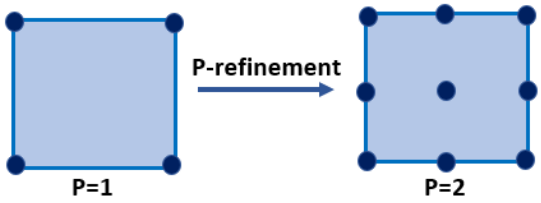

Figure 3.3: p-refinement

The highlighted data shown in Figure 3.4 is the mean surface age corresponds to the $N \times N$ point particles considered in further calculations to reduce errors. The number of $N \times N$ nodes used in BT10, BT20, BY10 and BY20 are 1024×1024, 512×512, 512×512 and 1024×1024, at time $t = 26.72, 28.39, 80$ and 50, respectively. This particle-density refinement study clearly shows all surface age approximations properly converge to a unique solution and the selected particle density used in the calculation of K_L in section 3.4 provides a good approximation.

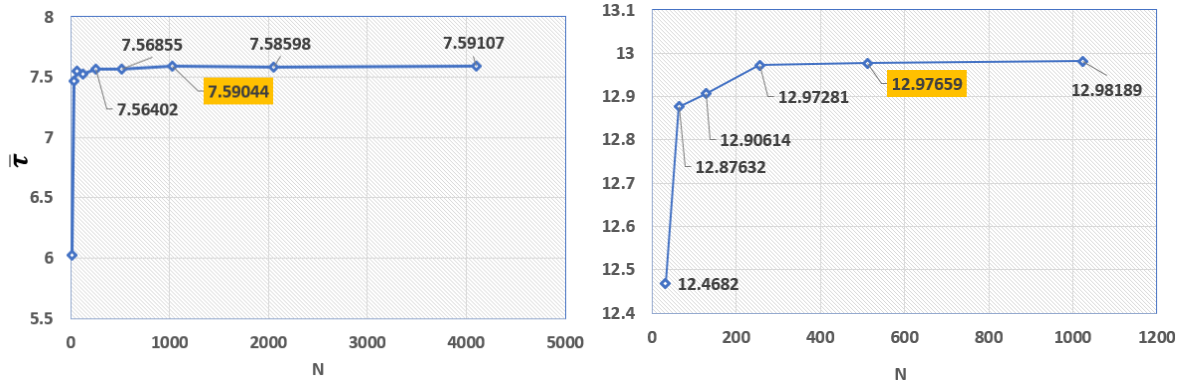

(a) BT10 (b) BT20

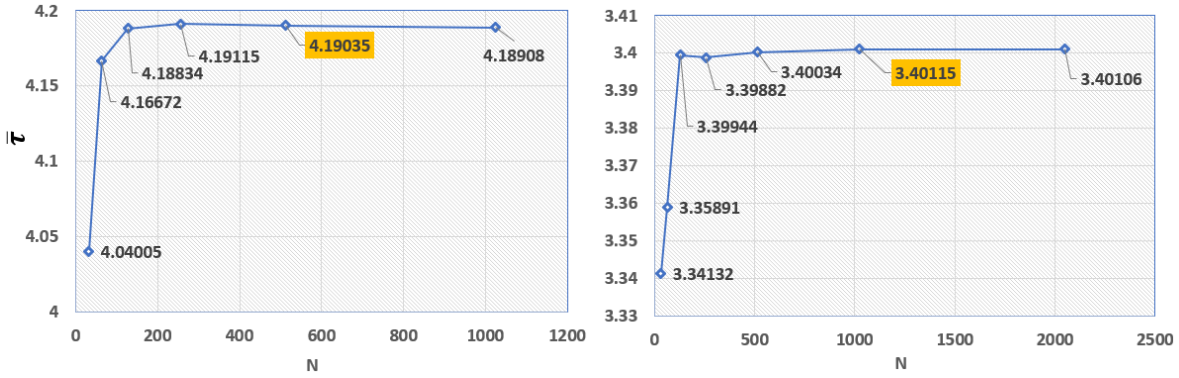

(c) BY10 (d) BY20

Figure 3.4: Mesh refinement study, when particles are initially placed at the nodes of the mesh.

It can be seen in Figure 3.4, with increasing $N \times N$ the mean surface age $\overline{\tau}$ approximation was found to drastically improve and converges to a particular value for each simulation. This mesh refinement study was carried out in order to obtain particle-density independent approximation of the mean surface age $\overline{\tau}$.

3.4 Results

Figure 3.5 shows the particle paths of seven individual particles, which were initially located in the upwelling region. Their paths were traced by performing Lagrangian tracing using the Adams-Bashforth AB2 method for time integration.

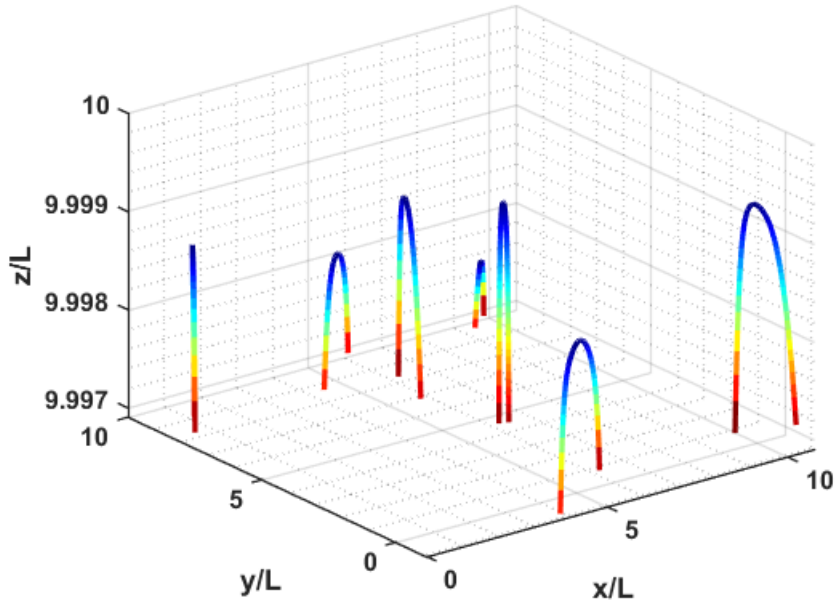

Figure 3.5: Particle paths of seven individual particles at time $t = 50$ s for BY10 simulation.

The blue color indicates that the particles reached a location that is very close to the surface. The surface age τ of a particle is defined by the time it takes for this particle starting at $z = z_0$ to return to its initial height.

The influence of various parameters on the mean surface age $\bar{\tau}$ was studied. One of the important parameters is the threshold (w_{th}), which was used to identify the active fluid particles with absolute velocity greater than w_{th}. The threshold used was $10^{-8}U$. The threshold actually restricts which particles will be used in the calculation of the mean surface age. Fluid particles, defined by having an absolute velocity less than w_{th} are discarded. To study the influence of the threshold on the weighted and non-weighted surface age, active particles were distributed into classes based on their initial vertical (w) velocity.

Table 3.3: Number of active particles using the initial w velocity classes for simulation BT10

Initial w velocity	Class mean	No. of active particles
0-0.02	0.01	171401
0.02-0.04	0.03	126251
0.04-0.06	0.05	69368
0.06-0.08	0.07	34581
0.08-0.10	0.09	15007
0.10 >	0.115	15375

The weighted and non-weighted variants are defined in detail in section 3.2. In the calculations, 1024×1024 uniformly distributed point particles were used to calculate weighted mean surface age $\overline{\tau}_w$ and non-weighted mean surface age $\overline{\tau}_{nw}$. The maximum value of initial w velocity under consideration was 0.13 m/s, threshold classes and the

number of active particles for each class are shown in Table 3.3. It can be seen that, in general, the number of active particles decreases with increasing initial w velocity (see Figure 3.6). Note that the last class has higher number of active particles than its previous class, it is due to the fact that the maximum value of initial w velocity was 0.13m/s, while all other classes were equally distributed.

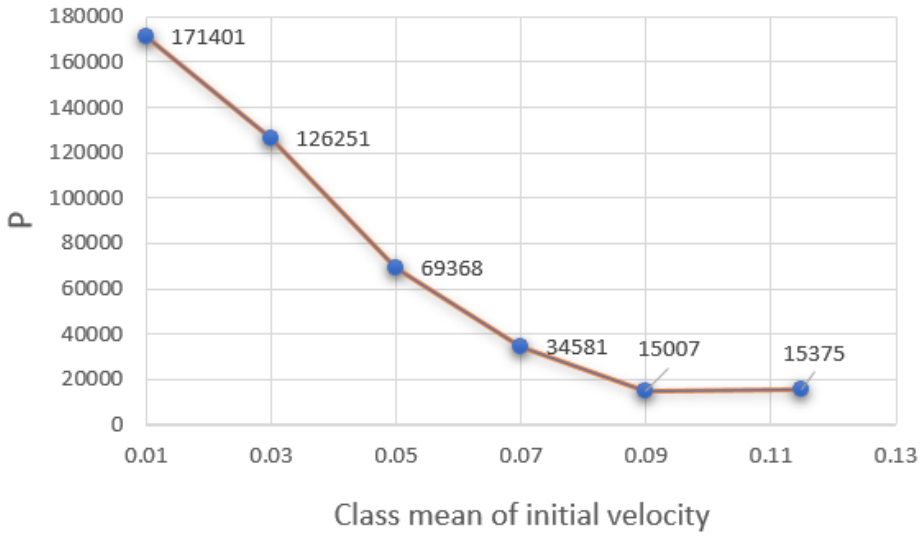

Figure 3.6: Influence of initial w velocity classes on number of active particles (P) for simulation BT10

Figure 3.7 shows the weighted and non-weighted mean surface age as a function of the class mean of the initial velocity for simulation BT10. Initially, in any calculation that starts by activating particles with initial w velocities (< 0.02 and $0.02 - 0.04$), the active particles have a relatively short surface age $\overline{\tau}$. Apparently, the active particles with low initial w velocity are already very close to the peak of their trajectory.

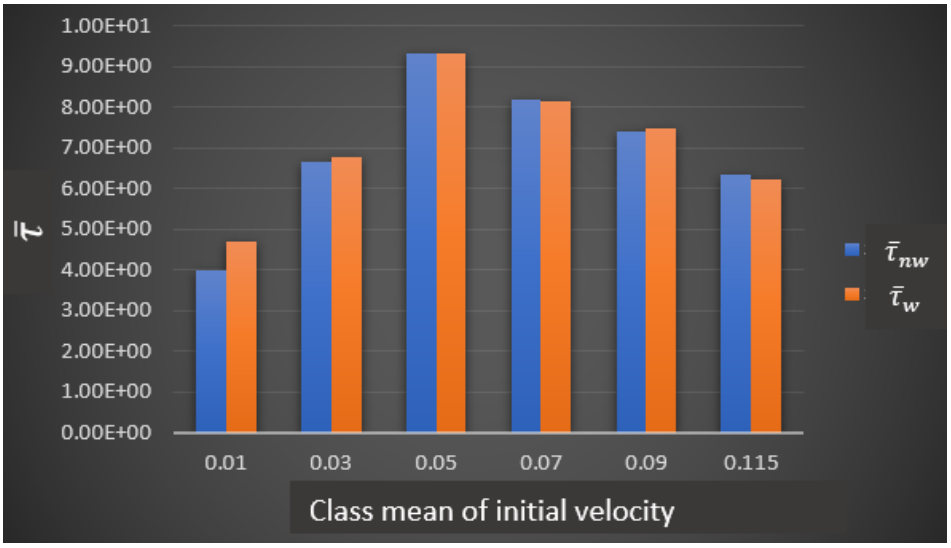

Figure 3.7: Influence of initial w velocity on $\overline{\tau}_w$ and $\overline{\tau}_{nw}$ for simulation BT10

Because of their small initial upward w-velocity, also the divergence so that the particles will only slightly move upwards and sidewards before moving quickly away from the surface. It can be seen that the active particles with a high initial w-velocity (in the last three classes) also tend to have a relatively small surface age. This is due to the fact that particles with a high initial velocity tend to undergo a large horizontal displacement so that particles reach down flow areas more quickly than particles with moderately high initial w-velocity (class 0.04-0.06).

Note that the difference between the $\overline{\tau}_w$ and $\overline{\tau}_{nw}$ in each class is relatively small because the small class size significantly reduces the variation in vertical velocities in each class and, hence, the variation in weights associated with each particle path. As a result the weights applied in the weighted surface age calculation tend to become more and more equal the smaller the class sizes become. The better agreement is obtained between $\overline{\tau}_w$ and $\overline{\tau}_{nw}$.

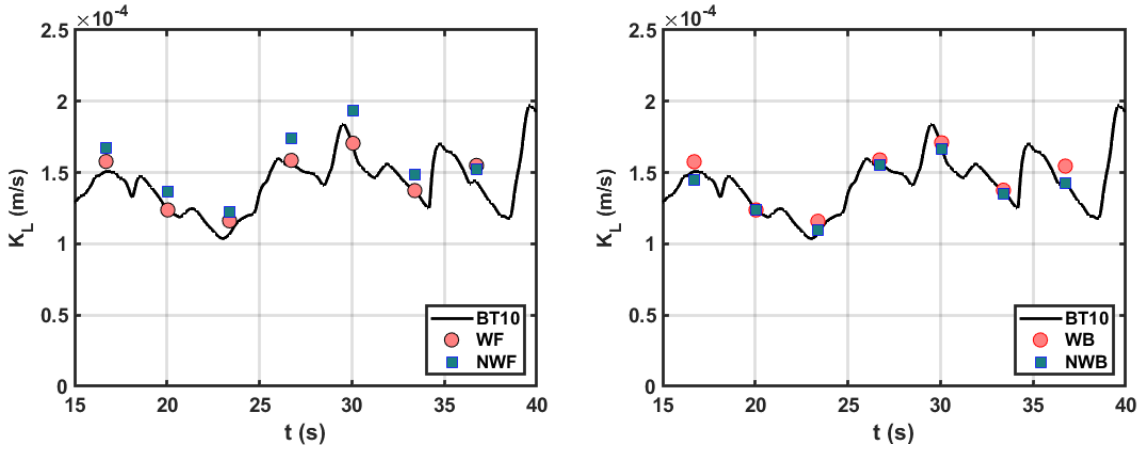

(a) (b)

Figure 3.8: The gas transfer velocity K_L in time for simulation BT10 for case (a) WF, NWF and (b) WB, NWB.

Gas transfer K_L was calculated using Danckwerts model (see section 2.4.1.3). Danckwerts model [14] allows the renewal time to follow an exponential probability distribution of surface renewal rate. K_L was calculated for both weighted and non-weighted mean surface age $\overline{\tau}$ using sequences of snapshots of velocity fields employing time integration both forward and backward in time. Results are shown in Figures 3.8, 3.9, 3.10 and 3.11. The results of K_L obtained from the mean surface age determined for the simulations listed in Table 3.1 compared to the corresponding numerically calculated K_L results of the same simulation. They were found to be in good agreement. For the gas transfer velocity K_L calculations using forward time integration, the weighted WF shows a better agreement with the existing DNS results (BT10) than the non-weighted NWF calculations. For backward time integration, both weighted WB and non-weighted NWB looks closer together in Figure 3.8b.

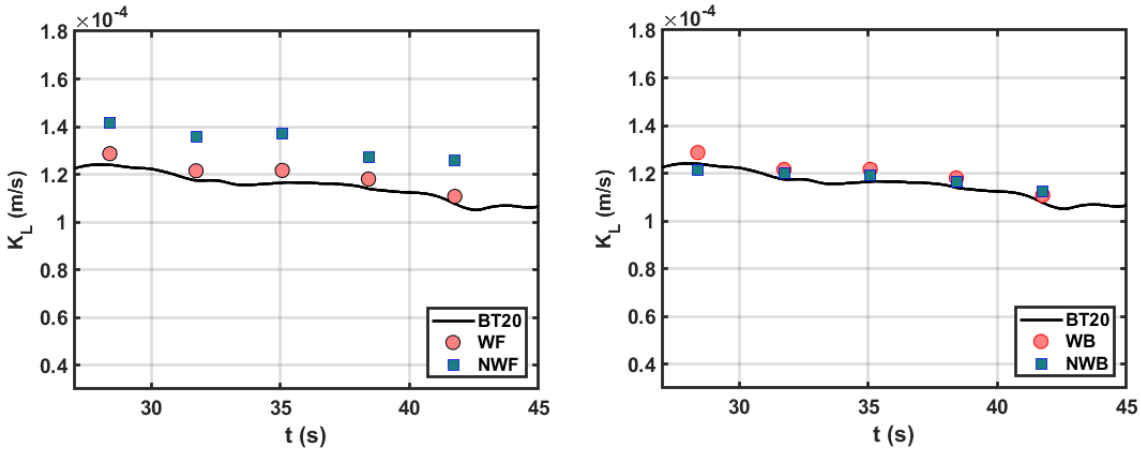

Figure 3.9: The gas transfer velocity K_L in time for simulation BT20 for case (a) WF, NWF and (b) WB, NWB.

In Figure 3.9a, generally both WF and NWF cases for the calculation of the gas transfer velocity K_L were over estimated. Whereas, it can be seen that weighted forward WF case was more accurate and closer to the DNS results, as compared to the results obtained using the non-weighted surface age NWF for BT20 simulation. The maximum error was about 20% for NWF at $t = 35$s. On the other hand, for the backward time integration in part (b), NWB and WB were found to be in good agreement with the DNS results. In particular, only one point at $t = 16.7$ shows the underestimation and overestimation for NWB and WB, respectively.

For the buoyant convectively induced turbulence BY10, shown in Figure 3.10, the predicted K_L results generally show an overestimation for all the cases of weighted/non-weighted surface age for forward/backward in time. Whereas, the weighted surface age for both forward and backward in time integration (WF and WB case) was found to be in good agreement with BY10 DNS results.

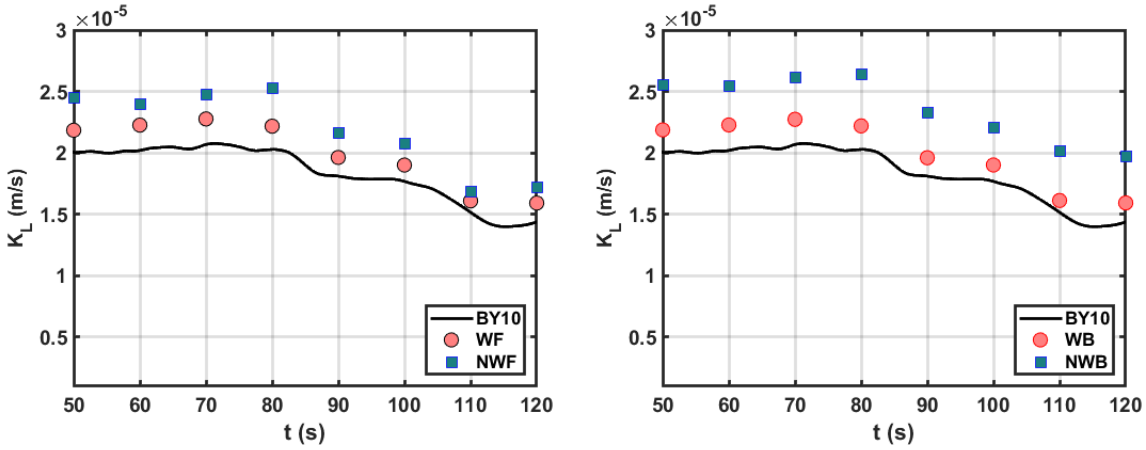

(a) (b)

Figure 3.10: The gas transfer velocity K_L in time for simulation BY10 for case (a) WF, NWF and (b) WB, NWB.

This is likely due to the fact that the divergence was implicitly taken into account (there is a linear relation between the divergence and the initial w velocity) when calculating the weighted surface age. In non-weighted surface age results, the maximum error of about 37.4% can be seen in case NWB at $t = 80$s (see Table 3.5).

In Figure 3.11, the gas transfer velocity K_L profiles are in excellent agreement for the weighted surface age calculations using both forward and backward (WF and WB case) in time integration except the only first point at $t = 40$s which show some overestimation. Hence, it can be concluded that the weighted surface age method in combination with Danckwerts' model produces more accurate results than the non-weighted variant. On the other hand, the non-weighted surface used in the calculation of the gas transfer velocity K_L was found to be overestimated at all times for cases NWF and NWB, with a maximum error of 28.4% at time $t = 40$s in NWB.

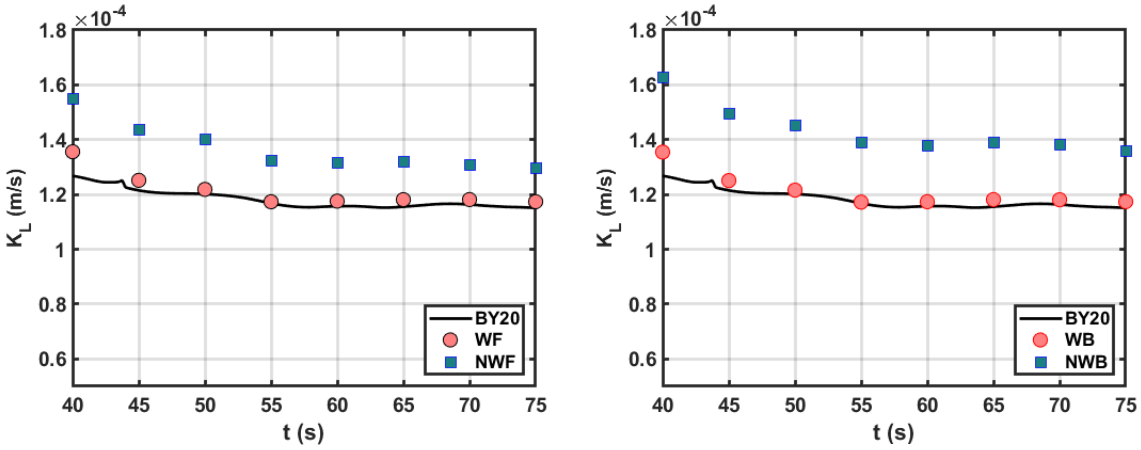

Figure 3.11: The gas transfer velocity K_L in time for simulation BY20 for case (a) WF, NWF and (b) WB, NWB.

The errors were calculated between the gas transfer K_L calculated directly from the numerical results and the predicted gas transfer calculated from Danckwerts model using the mean surface age $\overline{\tau}$. The averaged relative error (ARE) and maximum relative error (MRE), calculated for K_L in Tables 3.4 and 3.5, is given by

$$ARE(K_L) = \frac{1}{N}\sum_{i=1}^{N}\left(\frac{|K_L(i) - K_{L(\overline{\tau})}(i)|}{K_L(i)} \times 100\right), \tag{3.7}$$

$$MRE(K_L) = Max\left(\frac{|K_L(i) - K_{L(\overline{\tau})}(i)|}{K_L(i)} \times 100\right), \tag{3.8}$$

where K_L is the reference value from DNS (see Table 3.1), $K_{L(\overline{\tau})}$ is the predicted value calculated by using the mean surface age $\overline{\tau}$ and N is the total number of the snapshots of velocity field for each simulation.

Generally, K_L calculations obtained by using the weighted surface age approxima-

tions for forward in time integration, appear to be highly accurate.

Table 3.4: Averaged relative error (ARE) in gas transfer velocity K_L

Simulations	ARE(K_L)			
	WF	NWF	WB	NWB
BT10	3.9 %	9.7 %	3.8 %	3.4 %
BT20	4.0 %	16.4 %	4.0 %	2.3 %
BY10	8.9 %	19.1 %	9.0 %	29.1 %
BY20	2.4 %	15.4 %	2.3 %	20.9 %

Whereas, for the backward time integration, the bottom shear induced turbulence (BT10 and BT20) shows similar behaviour for both weighted and non-weighted surface age calculations For the buoyant convectively induced turbulence (BY10 and BY20) surface age calculations. However, the weighted surface age calculations were found to provide more accurate results.

Table 3.4 shows the averaged relative error (ARE) for the estimated gas transfer K_L using Danckwerts' model for all cases. It can be seen that, the K_L obtained using the weighted surface age approximations for forward in time integration (WF case) shows less errors as compared to NWF in all simulations. On the other hand, for backward in time integration (WB and NWB), it was found that simulation BY10 and BY20 shows a better agreement for WB. While, BT10 and BT20 shows slightly better for case NWB as compared to WB.

Table 3.5: Maximum relative error (MRE) in gas transfer velocity K_L

Simulations	MRE(K_L)			
	WF	NWF	WB	NWB
BT10	8.6 %	15.1 %	8.4 %	16.7 %
BT20	6.0 %	20.3 %	6.1 %	4.5 %
BY10	10.7 %	24.5 %	10.8 %	37.4 %
BY20	7.0 %	22.1 %	6.9 %	28.4 %

The corresponding maximum relative errors (MRE) was shown in Table 3.5. It can be seen that the maximum error of 37.4% can be found for case NBW in simulation BY10. Whereas, a smallest maximum-error of 4.5%4 was found in simulation BT20 for case NWB.

Chapter 4

Continuum method

This chapter outlines the development of the continuum method to calculate the mean surface age ($\overline{\tau}$) using the 5^{th} order WENO-Z scheme for the convection and a 3^{rd} order Runge-Kutta for the time integration. Subsequently, the gas transfer velocity K_L is calculated using Danckwerts' model [14]. The continuum method is employed to calculate the evolution of the surface age density, which is subsequently used to calculate the cumulative probability density distribution of the surface age τ.

4.1 Introduction

The surface age is an important parameter in the turbulent transport of heat and atmospheric gases across the air-water interface. This transport process, for instance, affects the water temperature and the transfer of atmospheric gases like O_2 and CO_2 from air into water and vice versa. Gas transfer across the water surface is governed by the interaction of molecular diffusion, which dominates gas transfer in a small layer immediately

underneath the surface, and vertical turbulent convection. The latter dominates further down into the bulk. Surface age is defined as the time that a fluid particle, that has been brought up from the bulk, remains at the surface (after which it eventually moves downwards). During this time, the particle (which is usually assumed to be unsaturated in the beginning) can absorb atmospheric gases. When the particle subsequently moves back towards the bulk, it also transports atmospheric gases downwards. At the surface, the amount of diffusion is governed by the diffusivity of the gas itself and the thickness of the saturation boundary layer. Turbulence typically reduces the thickness of this boundary layer, thereby increasing diffusion. Because there is no turbulent transport at the surface, the transfer velocity is fully determined by diffusion.

In the present study, the (mean) surface age is approximated by two different approaches: i) The Lagrangian particle tracking approach and ii) The continuum approach. Generally in fluid mechanics, Lagrangian methods (with the frame of reference moving with the flow) and Eulerian methods (with fixed frame of reference) can both be used to calculate fluid flow. To calculate the mean surface age, however, the Lagrangian particle tracking method is commonly used. After determining the mean surface age, the gas transfer velocity K_L is usually calculated using (a possibly modified version of) Danckwerts' model. Using the Lagrangian approach is the most natural way to describe fluid flow. It is based on tracking trajectories of discrete fluid particles so that the surface age of each individual particle can be determined directly. The simultaneous tracking of huge quantities of particles is the main disadvantage of the Lagrangian method as it requires extensive book keeping. Hence, to introduce this tracking of huge numbers of individual particles in traditional Eulerian codes (in which the continuum

assumption is employed) extensive modifications are required, especially in massively parallel codes. A more natural way to calculate the mean surface age in such codes is to use a continuum approach and replace the individual particles by a surface age density distribution. To illustrate the suitability of the continuum method to calculate the mean surface age, here both the classical Lagrangian particle tracking method and a newly developed continuum method are used to calculate the mean surface age of fluid particles (or parcels) transported by a predefined (as explained in Section 3.1.1) three dimensional (3D) turbulent flow field near the surface that is reconstructed from a given two dimensional (2D) interfacial velocity field.

4.1.1 Two ways to observe fluid flow

There are two, quite different, ways to observe fluid flow within a 3D domain, either by tracking identifiable, specific fluid point particles in a material fluid volume, the Lagrangian method, or by observing the fluid velocity at fixed locations in space, the continuum method.

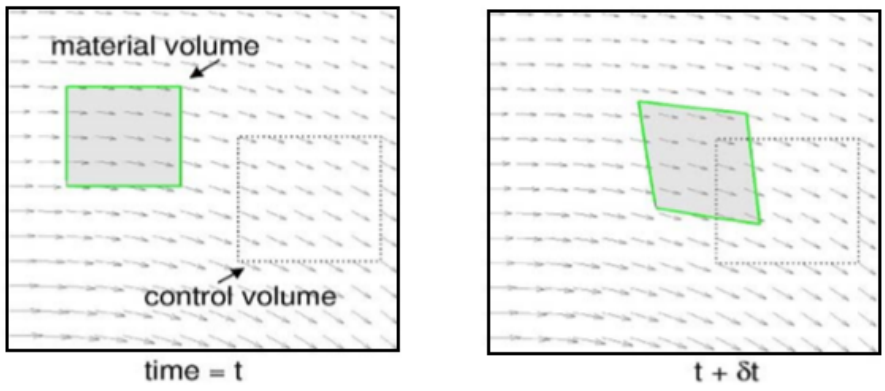

Figure 4.1: A material volume and a Eulerian control volume

Figure 4.1 shows a snapshot of a 2D velocity vector field. In this domain a material volume is identified (green boundary and shaded) as well as a control volume (dotted boundary).

The (Lagrangian) material fluid volume moves along with the flow (and possibly deforms) such that all fluid particles that were initially inside this volume remain inside the volume at all times. In contrast, the (continuum) Eulerian control volume is fixed in space allowing fluid particles to freely move in and out of the volume.

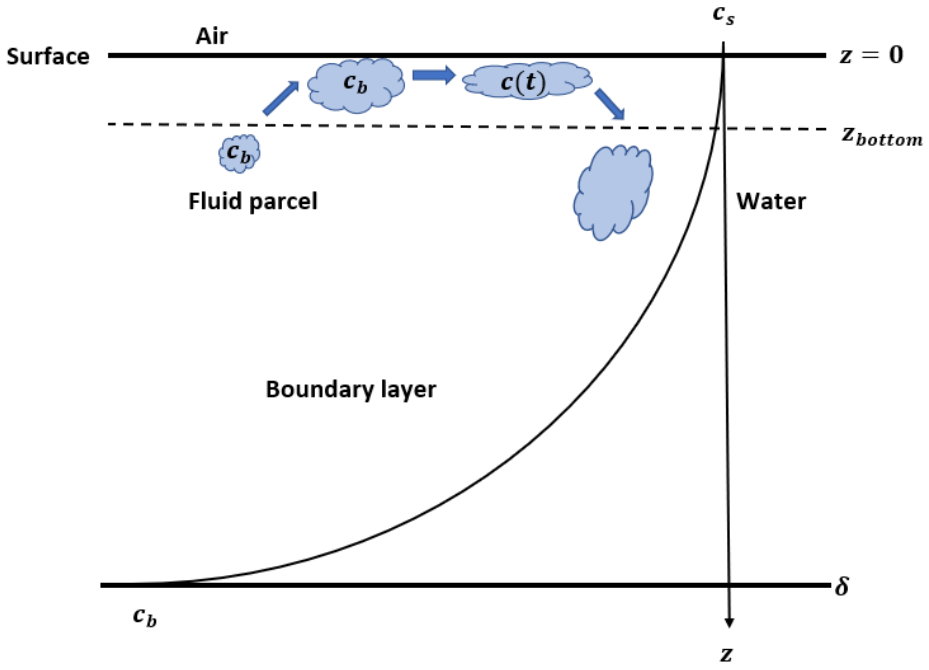

Figure 4.2: Schematic showing a cross section of the concentration boundary layer adjacent to the surface and the deformation of fluid parcel

Figure 4.2 shows a cross section of the concentration boundary layer adjacent to the surface. At the surface, the flow is assumed to be fully saturated ($c = c_s$), while at the bottom of the boundary layer the flow is initially fully unsaturated ($c = c_b$). The domain

considered in our calculations only consists of a small section of the concentration boundary layer adjacent to the surface. This section is bounded by $z = 0$ and $z = z_{bottom}$. In this section, the 3D velocity field can be reconstructed quite accurately from a 2D interfacial velocity field, similar to what was presented in Section 3.1.1. In contrast to the Lagrangian particle tracking method, the fluid parcels employed here in the continuum method can deform, so that positive surface divergence will result in enlargement of the surface area of the parcel, while negative surface divergence will make it smaller. This extra degree of freedom is the main difference between the Lagrangian and the continuum approach.

4.2 Numerical Aspects

In the continuum method, the convection of the surface age was calculated using the 5^{th} order WENO-Z scheme proposed by Borges *et al.* [8], which is an improved version of the original WENO scheme developed by Liu *et al.* [58]). For the time integration the total variation diminishing scheme (TVD) presented in Shu & Osher [79] was used.

In the following section, the WENO-Z scheme is applied to different test problems with the purpose to predict the accuracy of the method on uniform meshes.

4.2.1 WENO-Z scheme in a 1D test problem

First the implementation of the WENO-Z scheme is tested for convection in one-dimension using a uniform mesh. As in the three-dimensional calculation of surface age, any diffusion is neglected as this would interfere with determining the accuracy

of the WENO-Z scheme (and also we would like to use the continuum method as a alternative to the Lagrangian method in which diffusion does not play any role). The 1D convection equation,

$$\frac{\partial \tau}{\partial t} + \frac{\partial \tau}{\partial z} = 0, \tag{4.1}$$

was discretized on $0 \leq z \leq 1$ using periodic boundary conditions (see Figure 4.3). To obtain a smooth distribution of the variable τ, it was initialized by

$$\tau(z, 0) = \tau_0(z) = \frac{1}{2}\left(1 - \cos(2\pi z)\right) \tag{4.2}$$

The advantage of having such a smooth distribution is that it is relatively easy to accurately resolve it in the discretization that is employed, a non-smooth distribution would result in non-physical oscillations (wiggles) in the simulation. Here we determine the minimum number of points RZ (RZ is the refinement of each grid cell in z-direction) needed to obtain a good resolution of the initial surface age distribution, while also verifying the order of accuracy

$$\mathrm{p} = \frac{ln|\epsilon_{(z=0.5)_1}| - ln|\epsilon_{(z=0.5)_2}|}{lnh_1 - lnh_2} = \frac{ln\left|\frac{\epsilon_{(z=0.5)_1}}{\epsilon_{(z=0.5)_2}}\right|}{ln(h_1/h_2)} = \frac{ln\left|\frac{\epsilon_{(z=0.5)_1}}{\epsilon_{(z=0.5)_2}}\right|}{ln(RZ_2/RZ_1)} \tag{4.3}$$

of the WENO-Z scheme, which theoretically should be fifth-order accurate. If $\tau(z_i, t)$ and τ_{exact} are the numerical and exact solutions, respectively, at (z_i, t), the maximum absolute error ϵ is given by

$$\epsilon = \max_{1 \leq i \leq RZ} |\tau(z_i, t) - \tau_{exact}(z_i, t)| \tag{4.4}$$

Table 4.1: The maximum absolute error MAE in τ and the order of accuracy p

RZ	7	10	22	61
ϵ	0.0329	0.0055	1.0818×10^{-4}	6.4372×10^{-7}
p	-	5.01	4.98	5.02

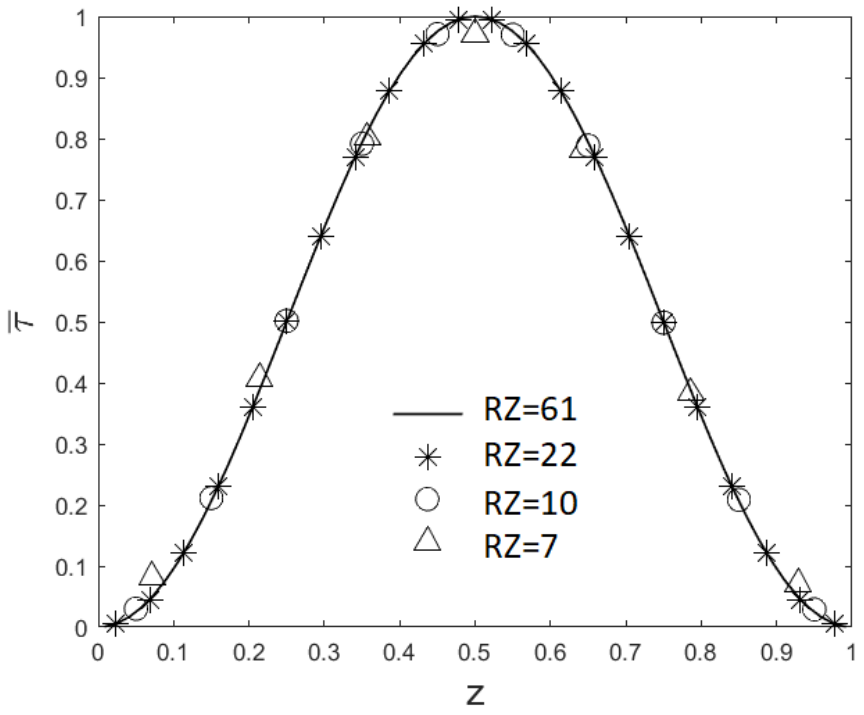

Figure 4.3: Effect of refinement in z-direction (1D periodic box)

Figure 4.3, generally shows a very good agreement between the results obtained after one time-unit of simulation. Only a slight underestimation of the peak at $z = 0.5$ can be seen for $RZ = 7$, while for $RZ = 10$ the approximation and the exact solution completely overlap. For completeness, the order of accuracy p of the method is also

verified for this 1D convection problem. It can be seen that the theoretical order of accuracy $p = 5$ is very nearly obtained in all three refinement steps.

4.2.2 Grid refinement studies in 3D

To assess the quality of the results for the mean surface age $\overline{\tau}$ obtained with the continuum method, a number of grid refinement studies was performed. In figure 4.4, the initial distribution of the surface age density (which is integrated in time to calculate the mean surface age) is shown for several values of N. It can be seen that when N increases the relative width of the initial surface age distribution reduces. Compared to the upper part of the computational domain, this with exactly $N-1$ times smaller when $N > 1$. Also, the larger N is, the smaller the error in $\overline{\tau}$ will be. In the first refinement study (see Table 4.2), $N = 7$ grid points were used in the z-direction and each grid cell was refined in the x and y direction by a factor of $RXY = 5$. While keeping the above parameters fixed, the refinement of each grid cell in the z-direction, RZ was varied to study its influence on the accuracy of the results approximating the weighted mean surface age of simulation BT10 at $t = 20$ s in Table 4.2. Note that the distribution in z of the surface age density is basically the same as the initial distribution used in the 1D convection problem investigated in Section 4.2.1. Based on that we would expect that for $RZ = 10$ a good approximation of $\overline{\tau}$ should be obtained. The results of refinement of cells in z-direction study can be seen in Table 4.2. It can be seen that already at $RZ = 10$ the error in $\overline{\tau}$ is less than 1% (assuming the result obtained for $RZ = 42$ is exact).

To also study the dependence of the results on the refinement in the x and y di-

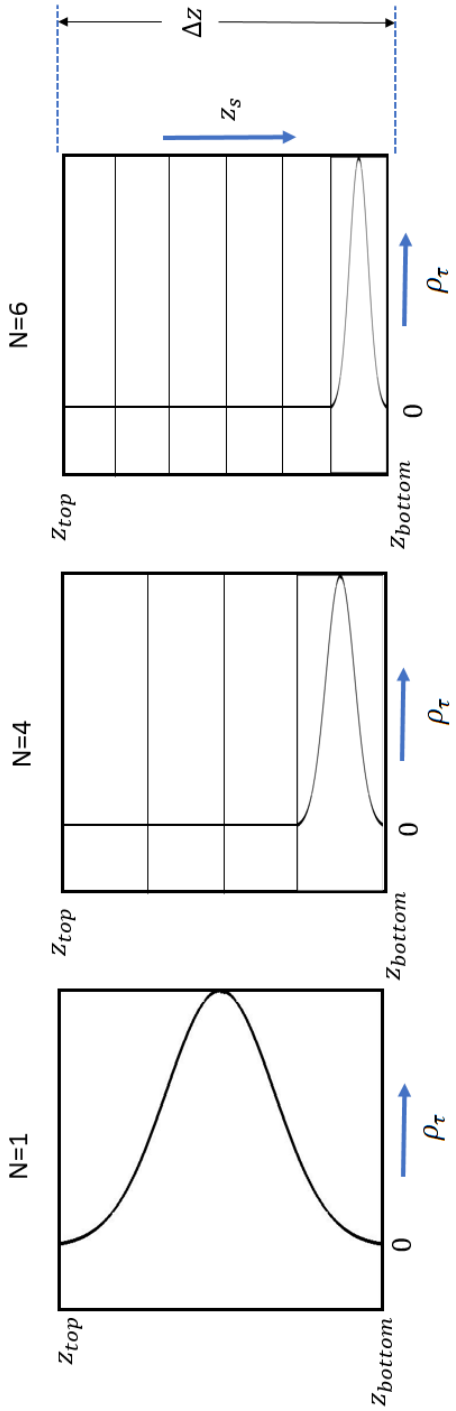

Figure 4.4: Schematic illustration of the width of $(\Delta z/N)$ of the initial surface age density distribution ρ_τ. N represents the number of mesh cells in the z-direction. Δz is the depth of the computational domain and $\rho_\tau > 0$ only in the mesh cell at the bottom. Note that $z_{top} = 0$ corresponds to the surface.

rections, Table 4.3 shows the results obtained when using $N = 7$ grid points in the z-direction, combined with a refinement in z of $RZ = 10$ to calculate the mean surface age of simulation BT10 at $t = 20$ s. Here it can be seen that refining the grid cells in the x, y-directions by $RXY = 3$ does give a noticeable improvement in the approximation of $\overline{\tau}$, with a reduction in error from approximately 3% to less than 0.3% (assuming that the result at $RXY = 7$ is exact).

Table 4.2: Refinement of cells in z direction for simulation BT10 using $N = 7$ and $RXY = 5$

RZ	$\overline{\tau}$
10	7.505
18	7.535
24	7.555
42	7.559

Based on the above, in order to obtain accurate results for $\overline{\tau}$, it was decided to use a refinement of the grid cells in z-direction of $RZ = 10$, combined with a refinement of $RXY = 5$ in the x and y directions to study the effect of increasing the number of grid cells N in the z-direction.

Table 4.3: Refinement of cells in the x, y directions for simulation BT10 using N=7 and RZ=10

RXY	$\overline{\tau}$
1	7.734
3	7.523
5	7.505
7	7.503

The effect of the number of mesh cells N in the z-direction on the initial distribution of ρ_τ is shown in Figure 4.4. It can be seen that with increasing N, the initial surface age density distribution ρ_τ becomes increasingly concentrated around the single location and becomes increasingly narrow. The fact that it has on the mean surface age ($\overline{\tau}$) is shown in Table 4.4, where it can be seen that with increasing N, $\overline{\tau}$ decreases and gradually converges. For more information on the influence of N, see Section 4.4.

Table 4.4: Influence of N on mean surface age $\overline{\tau}$ for simulation BT10, BT20 and BY10 with the refinement of RXY=5 and RZ=10

N	$\overline{\tau}$		
	BT10	BT20	BY10
2	9.011	15.596	5.630
4	8.213	14.043	5.426
8	7.870	13.335	5.320
16	7.732	13.003	5.260
32	7.694	12.847	5.238

4.3 Modelling used in the continuum method

The base mesh used for the calculation of the surface age with the continuum method was identical to the DNS mesh in the x, y directions. In the z-direction a uniform mesh was employed with N layers of grid cells between $z = 0$ and $z = z_{bottom}$. Note that z_0 identifies the z-location of the middle of the grid cells adjacent to z_{bottom} (see figure 4.5).

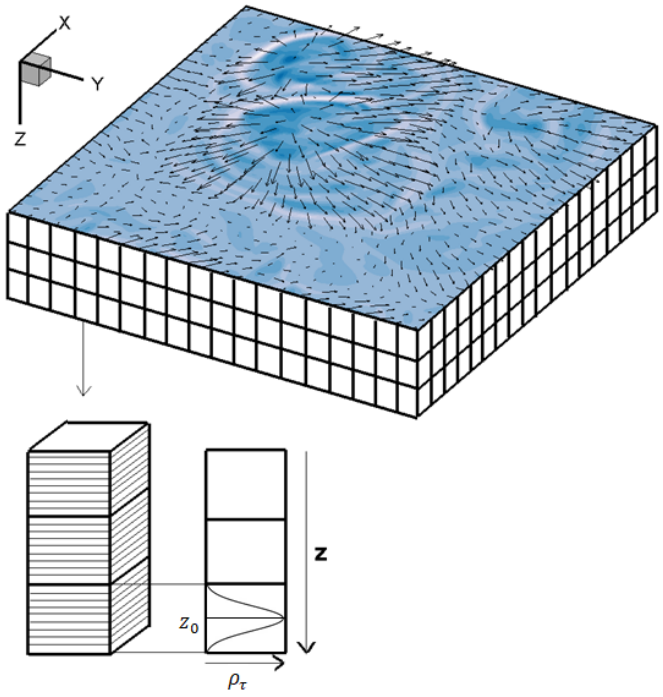

Figure 4.5: Schematic of continuum method, using $N = 3$ cells in the z-direction and a refinement in z of $RZ = 10$.

As already mentioned in section 3.1.1, at the surface of the computational domain a free-slip boundary condition was employed, while periodic boundary conditions were used in the horizontal directions. At the bottom of the computational domain, the

reconstructed velocity field (as explained in section 3.1.1) was used as boundary condition. As the vertical velocity scales linearly with z, the calculation of the surface age is independent of the actual mesh size in that direction. To estimate the mean surface age, a continuous surface age density $\rho_\tau = \rho_\tau(x, y, z, t)$, where t denotes time, was introduced to replace the point particles used in the Lagrangian method discussed in a section 3.1.2. To obtain a smooth initial density distribution $\rho_\tau \geq 0$ on the uniform base mesh in the z-direction, the number of mesh cells N were used in the z-direction. At the start of the calculations $\rho_\tau = \rho_\tau(x, y, z, 0)$ was initialised to be positive only in regions with upward flow, so that

$$\rho_\tau(x, y, z, 0) = \begin{cases} \Omega(x, y)(1 + \cos(\frac{2(z_0 - z)\pi}{\delta z})) & \text{if } w(x, y, z_0) < 0 \text{ and } z_b - \delta z \leq z \leq z_b \\ 0 & \text{otherwise} \end{cases}, \tag{4.5}$$

where δz is the size of the bottom most mesh cell in the z-direction, $z_b = z_{bottom}$, $z_0 = z_b - \frac{1}{2}\delta z$ is the centre of the grid cells adjacent to z_b, and Ω is defined by either $\Omega(x, y) = C$ for the non-weighted method or $\Omega(x, y) = C|w(x, y, z_0)|$ for the weighted method, with the constant C determined so that at $t = 0$

$$I_\tau(t) = \int_V \rho_\tau(x, y, z, t) dV = 1. \tag{4.6}$$

On the refined base mesh, an unsteady 3D convection equation for the surface age density

$$\frac{\partial(\rho_\tau)}{\partial t} + \frac{\partial(u\rho_\tau)}{\partial x} + \frac{\partial(v\rho_\tau)}{\partial y} + \frac{\partial(w\rho_\tau)}{\partial z} = 0, \tag{4.7}$$

was solved using the fifth-order-accurate WENO-Z scheme for the convective terms

combined with a third-order Runge-Kutta method [8] for the time-integration. For the surface age density, ρ_τ, a symmetry boundary condition was used at the surface, while in the lower part of the computational domain (for $z > z_{bottom}$), ρ_τ was set to zero, to model that the fluid left the near surface region. The mean surface age $\bar{\tau}$ was calculated using both the time step δt and (4.6), giving

$$\bar{\tau} = \int_0^\infty I_\tau(t)dt \approx \sum_{n=1}^{\infty} I_\tau(n\delta t)\delta t, \tag{4.8}$$

where $t = n\delta t$. Note that the calculation was stopped as soon as $I_\tau(t) < \varepsilon$, with $\varepsilon \sim 10^{-4}$. Based on the above, we can calculate the cumulative distribution of the mean surface age

$$C_\tau(t) = 1 - I_\tau(t) \tag{4.9}$$

and verify that it approximately has a log-normal distribution. The probability density of the log-normal distribution is given by

$$\rho(t) = \frac{d}{dt}C_\tau = \frac{e^{-(\ln t - \mu)^2/2\sigma^2}}{t\sigma\sqrt{2\pi}}. \tag{4.10}$$

Where σ the standard deviation of the log of the distribution and μ is the mean of the log of the distribution. Results are shown in the following section for commulative distribution and the log normal distribution of surface age.

4.3.1 Probability density distributions of surface age

Dankwerts considered the distribution of the surface ages of all particles that were present at the surface in a snapshot taken at the random time t. It is known, that in this case, the surface ages of these particles would be exponentially distributed [14]. However, when using the Lagrangian particle tracking method, for each particle that moves upwards, we determine the surface age by following the particle in time along the surface until it moves down again. The distribution of the surface ages of these particles would be a log normal distribution. In the continuum method, we use a particle density as a replacement for the individual particles. As can be seen below, this method allows for an easy determination of the underlying log normal distribution. Figures 4.6, 4.7 and 4.8 show the cumulative probability distributions of the surface age density and the corresponding instantaneous probability distribution obtained by taking its time derivative. The cumulative distributions for BT10, BT20 and BY10 were obtained from Eq. 4.9.

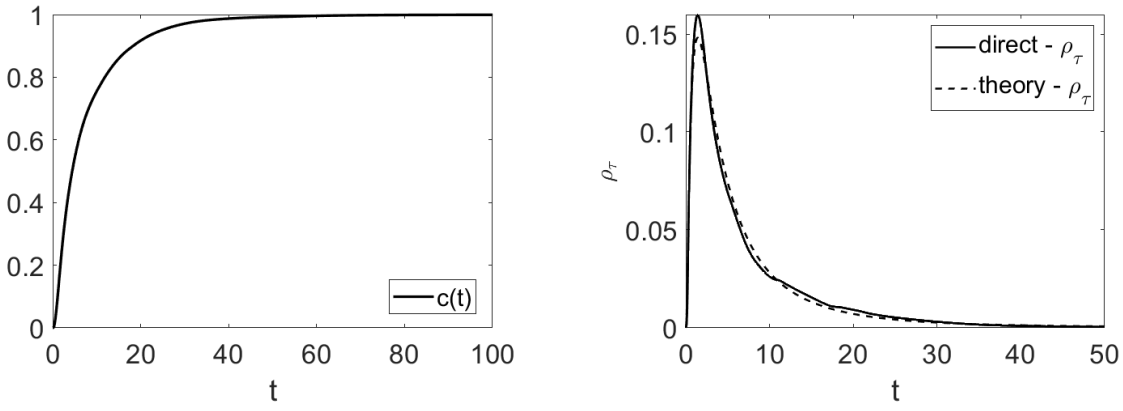

(a) (b)

Figure 4.6: (a) Cumulative distribution and (b) comparison between the instantaneous probability distribution calculated directly from the continuum method (direct-ρ_τ) and lognormal distribution (theory-ρ_τ) of the surface age (for BT10 simulation at $t = 100\,\mathrm{s}$ for N=32, RZ=10, RXY=5, using $\mu = 1.495$ and $\sigma^2 = 1.137$).

Part (b) of the Figures not only shows the instantaneous probability distribution calculated directly from the continuum method but also the closest matching lognormal distribution. It can be seen that a good agreement is obtained between the shapes of the calculated distribution and the shape of the theoretical distribution. This gives us an alternative way to estimate the mean surface age $\overline{\tau} = e^{\mu+\sigma^2/2}$, where μ is the mean of the instantaneous surface age $\ln \tau$ and σ^2 is the variance of $\ln \tau$.

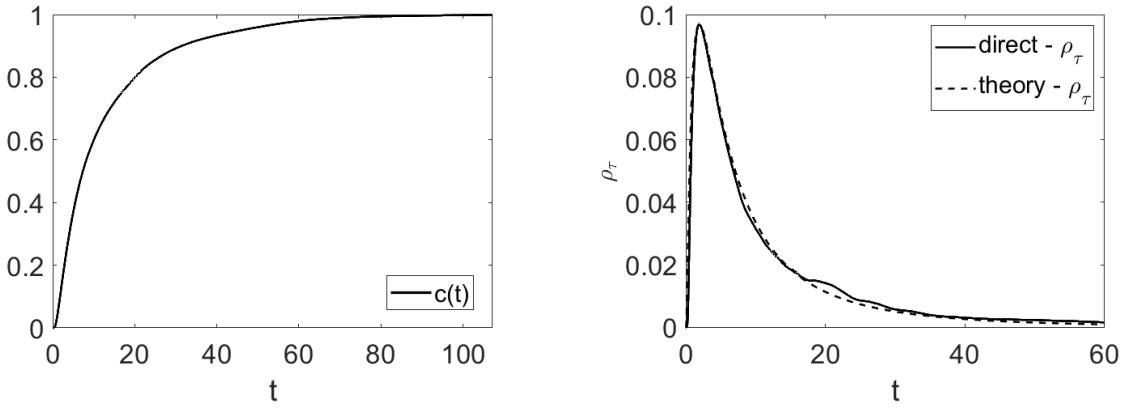

(a) (b)

Figure 4.7: (a) Cumulative distribution and (b) comparison between the instantaneous probability distribution calculated directly from the continuum method (direct-ρ_τ) and lognormal distribution (theory-ρ_τ) of the surface age (for BT20 simulation at $t = 31.73\,\mathrm{s}$ for N=16, RZ=10, RXY=5, using $\mu = 1.930105$ and $\sigma^2 = 1.262667$).

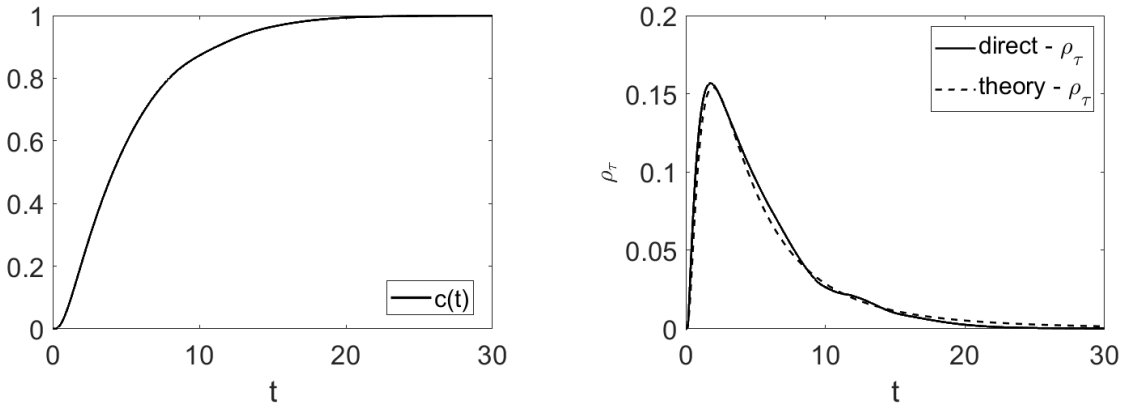

(a) (b)

Figure 4.8: (a) Cumulative distribution and (b) comparison between the instantaneous probability distribution calculated directly from the continuum method (direct-ρ_τ) and lognormal distribution (theory-ρ_τ) of the surface age (for BY10 simulation at $t = 90\,\mathrm{s}$ for N=16, RZ=10, RXY=5, using $\mu = 1.46187$ and $\sigma^2 = 0.80147$).

4.4 Overestimation of surface age

While the surface age density remains inside the domain $0 < z < z_b$ it is taken into account while calculating the integral in Eq. 4.6. As soon as it is transported outside of this domain it is put to zero so it does not contribute to the calculation anymore. Because of the fact that the initial surface age density was not defined at $z = z_b$ but was distributed over the bottom grid cells, the surface age will always be overestimated. Making some simplifying assumptions, the error made can be estimated.

For this, we first assume that there is one interval ($N = 1$) and model any dependencies on the vertical coordinate by a dependency on time, while ignoring the homogeneous horizontal directions. We start by defining the average vertical velocity as a function of time

$$w(t) = a\left(\frac{\tau}{2} - t\right) \tag{4.11}$$

where τ is the surface age, t is time and a is a constant of proportionality. Based on the definition in Eq. 4.11 we can calculate the average z location

$$z(t) = \int_0^t w(t')dt' = \int_0^t a\left(\frac{\tau}{2} - t'\right)dt' = \frac{a}{2}(t\tau - t^2) \tag{4.12}$$

as a function of time. Note that $z(0) = z(\tau) = 0$ and the maximum z-location that is reached is $z(\tau/2) = a(\tau^2/8)$.

Next, we assume that the above is valid for the calculation of the surface age for particles originating at $z(0) = 0$. In the simulation such particles are tracked until they reach the z-location $z(t) = -a(\tau^2/8)$.

By writing $t = c\tau$, we obtain the equation $\frac{a}{2}(c\tau^2 - c^2\tau^2) = a\frac{\tau^2}{8}$ which has one relevant

solution $c = -\frac{1}{2} + \frac{1}{\sqrt{2}}$. Note that c is, in fact, the factor by which the approximated surface age overestimates the real surface age.

In the simulation, however, the particle can originate at any location $z(0) \in \left(-a\frac{\tau^2}{8}, a\frac{\tau^2}{8}\right)$. To model this, we represent the z-location of such a particle by

$$z(t) = \frac{\gamma a}{2}(t\tau - t^2) + a(1-\gamma)\frac{\tau^2}{8}, \tag{4.13}$$

where $0 < \gamma < 2$. Note that $\gamma = 1$ corresponds to the situation discussed above.

We now solve

$$z(t) = \frac{\gamma a}{2}(t\tau - t^2) + a(1-\gamma)\frac{\tau^2}{8} = -a\frac{\tau^2}{8} \tag{4.14}$$

and again substitute $t = c\tau$ in Eq. 4.14 to obtain the relevant solution $c = \frac{1}{2} + \frac{1}{\sqrt{2\gamma}}$.

To approximate the average factor $\bar{c}$ by which the surface in the calculation with one interval is overestimated we need to calculate

$$\bar{c} = \frac{1}{2}\int_0^2 \left(\frac{1}{2} + \frac{1}{\sqrt{2\gamma}}\right)(1 - \cos(\pi\gamma))\, d\gamma \approx 1.2559 \tag{4.15}$$

To improve the estimation of the surface age we then calculate $\tau = \frac{\tau_{approx}}{\bar{c}}$. When there are N intervals, the situation slightly changes.

In this case, the particle can originate at any location $z(0) \in \left(-a\frac{\tau^2}{8N}, a\frac{\tau^2}{8N}\right)$, to model this, we again represent the z-location of such a particle by

$$z(t) = \frac{\gamma a}{2}(t\tau - t^2) + a(1-\gamma)\frac{\tau^2}{8}, \tag{4.16}$$

where $1 - \frac{1}{N} < \gamma < 1 + \frac{1}{N}$. Note that $N = 1$ corresponds to the situation discussed

above. We now solve

$$z(t) = \frac{\gamma a}{2}(t\tau - t^2) + a(1-\gamma)\frac{\tau^2}{8} = -a\frac{\tau^2}{8N} \tag{4.17}$$

and again substitute $t = c\tau$ in Eq. 4.14 to obtain the relevant solution

$$c(\gamma, N) = \frac{1}{2} + \frac{\sqrt{\gamma\left(1+\frac{1}{N}\right)}}{2\gamma}. \tag{4.18}$$

and average factor $\overline{c}(N)$ by which the surface in the calculation with N intervals is overestimated can be found from

$$\overline{c} = \frac{N}{2}\int_{1-\frac{1}{N}}^{1+\frac{1}{N}} \left(\frac{1}{2} + \frac{\sqrt{\gamma\left(1+\frac{1}{N}\right)}}{2\gamma}\right)(1-\cos(N\gamma\pi))\,d\gamma. \tag{4.19}$$

The aim of the above model is to show that the overestimation of surface age would reduce by increasing N. Figure 4.9a shows the overestimation of surface age for simulation BY10 by using the above theory $\overline{c}$(theory) and the results of surface age obtained by the continuum method c(direct). It can be seen that the error significantly decreases between the two with increasing N.

Finally, we assume that the upward and downward velocities differ (but are both constant). First we take

$$w(t) = a(b\tau - t), \text{if } \; t < b\tau \qquad (0 < b < 1) \tag{4.20}$$

$$w(t) = \frac{ab^2}{(b-1)^2}(b\tau - t), \text{if } \; t > b\tau \tag{4.21}$$

where a is a constant of proportionality and $b^2/(b-1)^2$ represents the ratio between the magnitudes of the mean downward velocity and the mean upward velocity.

Based on the definition Eq. 4.20 we can calculate the average z-location

$$z(t) = \int_0^t w(t')dt' = \int_0^t a(b\tau - t')dt' = \frac{a}{2}(2b\tau t - t^2), \text{if } t \leq b\tau \tag{4.22}$$

$$\begin{aligned} z(t) =& \frac{1}{2}ab^2\tau^2 + \int_{b\tau}^t w(t')dt' \\ =& \frac{1}{2}ab^2\tau^2 + \frac{ab^2}{(b-a)^2}\int_{b\tau}^t (b\tau - t') \\ =& \frac{1}{2}ab^2\tau^2 + \frac{ab^2}{(b-1)^2}\left[b\tau t - \frac{1}{2}t^2 - \frac{1}{2}b^2\tau^2\right], \text{if } t > b\tau \end{aligned} \tag{4.23}$$

as a function of time. Note that $z(0) = z(\tau) = 0$ and the maximum z-location that is reached is $z(b\tau) = \frac{1}{2}ab^2\tau^2$. To estimate of the over prediction, we need to solve:

$$\frac{1}{2}ab^2\tau^2 + \frac{ab^2}{(b-1)^2}\left[b\tau t - \frac{1}{2}t^2 - \frac{1}{2}b^2\tau^2\right] = -\frac{1}{2}ab^2\tau^2 \implies \tag{4.24}$$

$$ab^2\tau^2 + \frac{ab^2}{(b-1)^2}\left[b\tau t - \frac{1}{2}t^2 - \frac{1}{2}b^2\tau^2\right] = 0 \implies$$

Using $t = c\tau$

$$\frac{(c-b)^2}{(b-1)^2} = 2 \implies c = b + \sqrt{2}(1-b) \tag{4.25}$$

In the simulation, however, the particle can originate at any location $z(0) \in \left(-\frac{1}{2}ab^2\tau^2, \frac{1}{2}ab^2\tau^2\right)$. To model this, we represent the z-location of such a particle by

$$z(t) = \frac{\gamma a}{2}(2b\tau t - t^2) + \frac{1}{2}a(1-\gamma)b^2\tau^2, \quad (\text{for } t \leq b\tau) \tag{4.26}$$

$$z(t) = \frac{1}{2}ab^2\tau^2 + \frac{\gamma ab^2}{(b-1)^2}\left(b\tau t - \frac{1}{2}t^2 - \frac{1}{2}b^2\tau^{"}\right), \quad (\text{for } t > b\tau) \tag{4.27}$$

where $0 < \gamma < 2$. Note that $z(\tau) = z(0) = \frac{1}{2}a(1-\gamma)b^2\tau^2$. We now solve

$$z(\tau) = \frac{1}{2}ab^2\tau^2 + \frac{\gamma ab^2}{(b-1)^2}\left[b\tau t - \frac{1}{2}t^2 - \frac{1}{2}b^2\tau^2\right] = -\frac{1}{2}ab^2\tau^2 \tag{4.28}$$

and again substitute $t = c\tau$ in Eq. 4.28 to obtain;

$$c = b + (1-b)\sqrt{2/\gamma} \tag{4.29}$$

To approximate the average factor $\overline{c}$ by which the surface in the calculation with one interval is overestimated we need to calculate

$$\overline{c} = \frac{1}{2}\int_0^2 (b + (1-b)\sqrt{2/\gamma})(1 - \cos(\pi\gamma)d\gamma) \implies \tag{4.30}$$

$$\overline{c} = b + (1-b)\frac{1}{2}\int_0^2 \sqrt{2/\gamma})(1 - \cos(\pi\gamma)d\gamma) = b + 1.5117(1-b)$$

So that for $b = 0.4335$ an average factor $\overline{c} = 1.2899$ is obtained. When there are N intervals, the situation slightly changes. In this case, the particle can originate at any location $z(0) \in \left(-\frac{1}{2N}ab^2\tau^2, \frac{1}{2N}ab^2\tau^2\right)$, to model this we again represent the z-location of such a particle by

$$z(t) = \frac{\gamma a}{2}(2b\tau t - t^2) + \frac{1}{2}a(1-\gamma)b^2\tau^2, \quad (\text{for } t \leq b\tau) \tag{4.31}$$

$$z(t) = \frac{1}{2}ab^2\tau^2 + \frac{\gamma ab^2}{(b-1)^2}\left[b\tau t - \frac{1}{2}t^2 - \frac{1}{2}t^2\tau^2\right], \quad (\text{for } t > b\tau) \tag{4.32}$$

where $1-\frac{1}{N} < \gamma 1+\frac{1}{N}$.. Note that $N = 1$ corresponds to the situation discussed above. We now solve

$$z(t) = \frac{1}{2}ab^2\tau^2 + \frac{\gamma ab^2}{(b-1)^2}\left[b\tau t - \frac{1}{2}t^2 - \frac{1}{2}t^2\tau^2\right] = -\frac{1}{2N}ab^2\tau^2 \tag{4.33}$$

So that after substituting $t = c\tau$ we obtain

$$N + \frac{1}{N}\frac{\gamma(c-b)^2}{(b-1)^2} \implies c = b + \sqrt{\frac{N+1}{\gamma N}}(1-b) \tag{4.34}$$

and the average factor $\overline{c}(N)$ by which the surface in the calculation with N intervals is

$$\overline{c} = b + (1-b)\frac{N}{2}\int_{1-\frac{1}{N}}^{1+\frac{1}{N}} \sqrt{\frac{N+1}{\gamma N}}(1-\cos(N\gamma\pi))\,d\gamma. \tag{4.35}$$

In Figure, 4.9b, clearly a much better approximation can be seen by assuming the different velocities and overestimation reduces with increasing N.

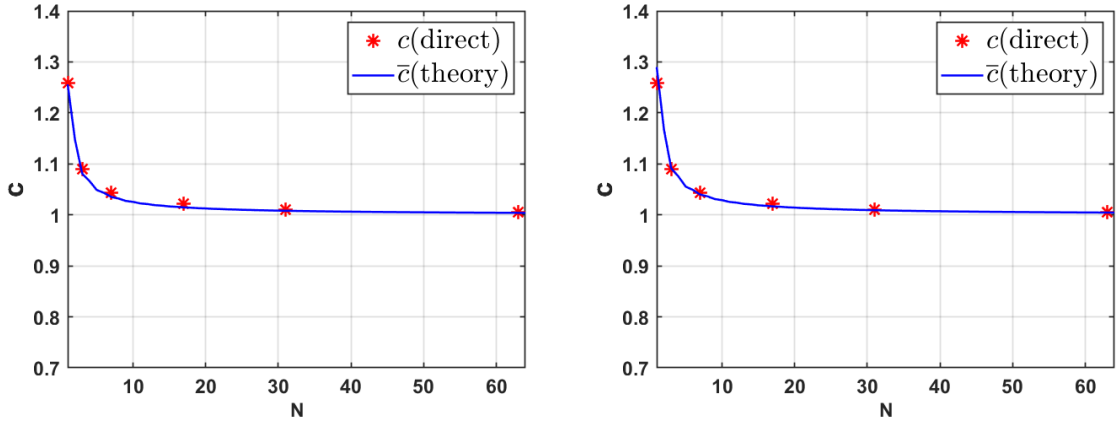

(a) (b)

Figure 4.9: Overestimation of surface age by assuming the (a) upward and downward velocities are the same and (b) upward and downward velocities differ for simulation BY10.

Note that the non-weighted surface age τ_{nw} is assumed in the above model. While, the weighted surface age τ_w is used to calculate the overestimation from continuum method. To justify this, we have already showed in section 3.4 that the accuracy of τ_{nw} and τ_w behaves very similar to each other. Thus, we conclude that the presented model has quite good approximation of overestimation of surface age.

4.5 Results and discussions

A smooth initial density distribution on the uniform base mesh in the z-direction can be obtained by increasing the values of N as discussed in section 4.2.2. Note that, in Figure 4.10, $\overline{\tau}$ corresponds to mean weighted surface age as it is already discussed in section 3.4 that accuracy of weighted and non-weighted surface age behaves similar.

Figure 4.10a represents the mean surface age $\overline{\tau}$ (solid line) with several values of N. Dashed line represents the mean surface age $\overline{\tau}$ obtained from Lagrangian method using 1024×1024 point particles. It can be seen that $\overline{\tau}$ converges with increasing number of N. Figure 4.10b and 4.10c shows a convergence of mean surface age with increasing N, where the mean surface age obtained from Lagrangian method (dashed line) is at $\overline{\tau} = 12.6991$ and 5.2022, respectively. The number of mesh cells N used in BT10, BT20 and BY10 are $2, 4, 8, 16$ and 32 at time $t = 16.7, 31.73, 90$s, respectively.

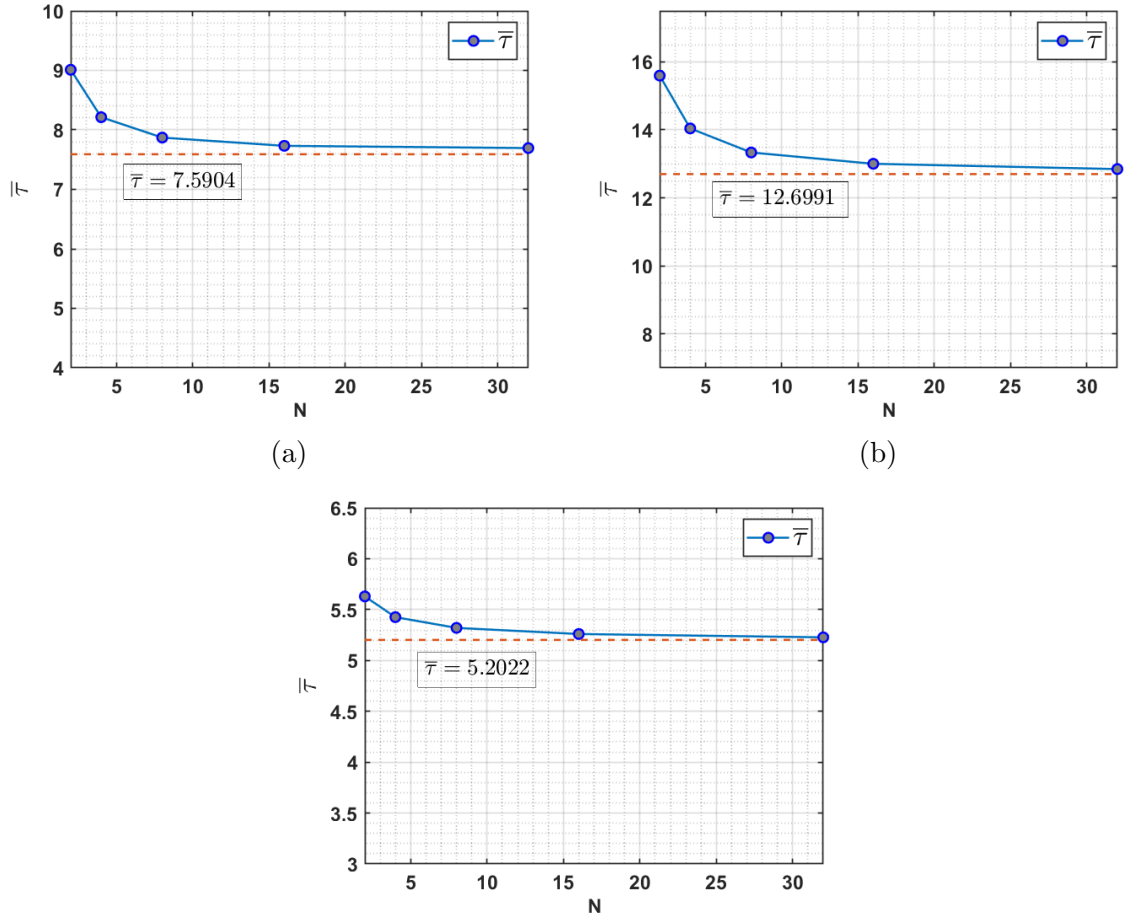

Figure 4.10: Effect of N on mean surface age $\overline{\tau}$ using Rz=10 and RXY=5 for simulation (a) BT10 at $t = 16.7$s, (b) BT20 at $t = 31.73$s and (c) BY10 at $t = 90$s.

The error was calculated between the mean weighted surface age $\overline{\tau}$ calculated directly from continuum method and the mean surface age obtained from Lagrangian method. An averaged relative error (ARE), calculated for $\overline{\tau}$ is given by

$$ARE(\overline{\tau}) = \frac{1}{N}\sum_{i=1}^{N}\left(\frac{|\overline{\tau_L}(i) - \overline{\tau_C}(i)|}{\overline{\tau_L}(i)} \times 100\right), \tag{4.36}$$

where, $\overline{\tau_L}$ and $\overline{\tau_C}$ represents the results of $\overline{\tau}$ obtained from Lagrangian and continuum method, respectively. In Table 4.5, it can be seen that for large N, the absolute error AE significantly decreases and reaches a minimum of 0.2733%, 0.2325% and 0.0964% for simulation BT10, BT20 and BY10, respectively. The gas transfer K_L was calculated

Table 4.5: Averaged relative error of mean surface age $\overline{\tau}$

Simulations	N				
	2	4	8	16	32
BT10	3.7417 %	1.6408 %	0.7377 %	0.3730 %	0.2733 %
BT20	4.5604 %	2.1160 %	1.0020 %	0.4784 %	0.2325 %
BY10	1.6430 %	0.8579 %	0.4532 %	0.2218 %	0.0964 %

using Danckwerts model. Note that, for the continuum method, K_L was calculated only for the weighted mean surface age using sequences of snapshots of velocity fields employing time integration forward in time.

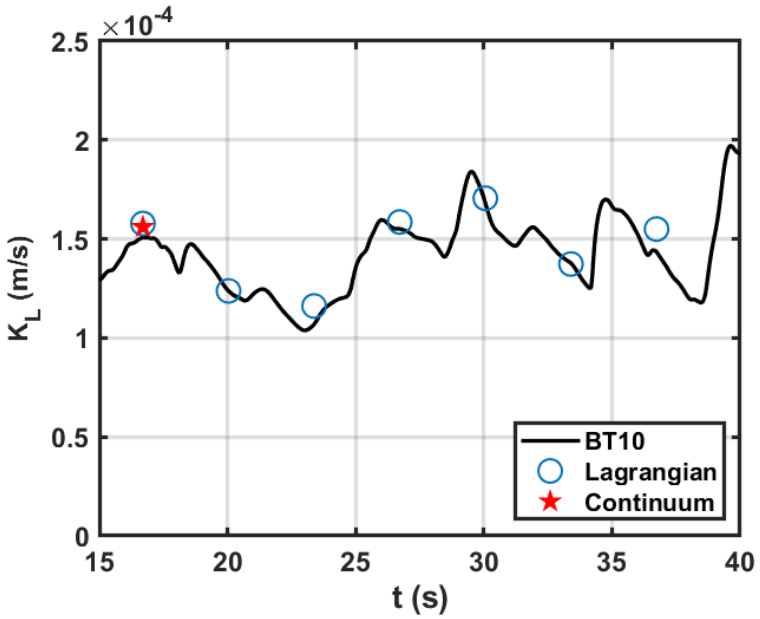

Figure 4.11: Gas transfer velocity K_L in time at $t = 16.7$s for simulation BT10 using RZ=10, RXY=5 and N=32.

Figures 4.11, 4.12 and 4.13 compares the gas transfer velocity K_L obtained using the continuum method, the Lagrangian method and the 3D DNS (reference) of simulations BT10, BT20 and BY10, respectively. While the Lagrangian results are shown for several instances in time, from continuum results are only shown for one instance in each of the figures. For BT10 and BT20, the Lagrangian and continuum were found to be in good agreement with the DNS results. For BY10, on the other hand, the results obtained in the Lagrangian and continuum method were found to more significantly overestimate the DNS results. A more quantitative discussion using the errors displayed in Table 4.6 can be found below.

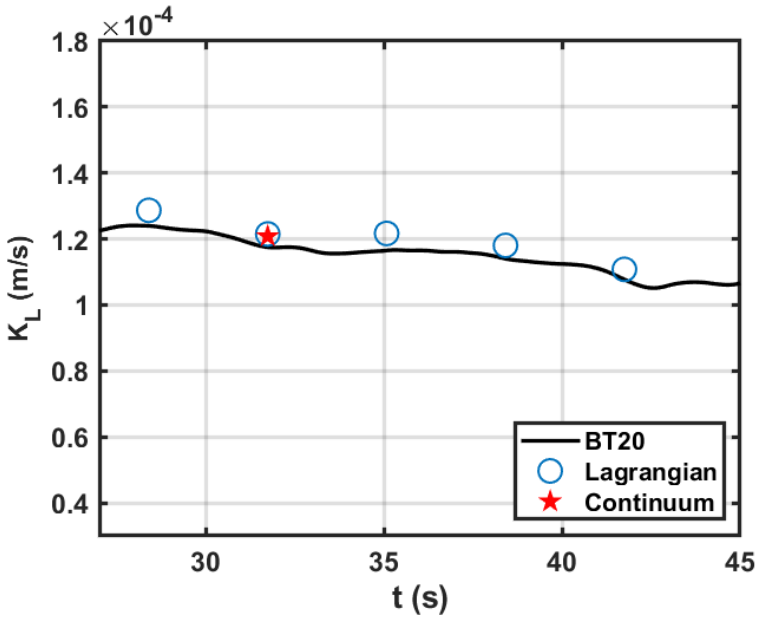

Figure 4.12: Gas transfer velocity K_L in time at $t = 31.73$s for simulation BT20 using RZ=10, RXY=5 and N=32.

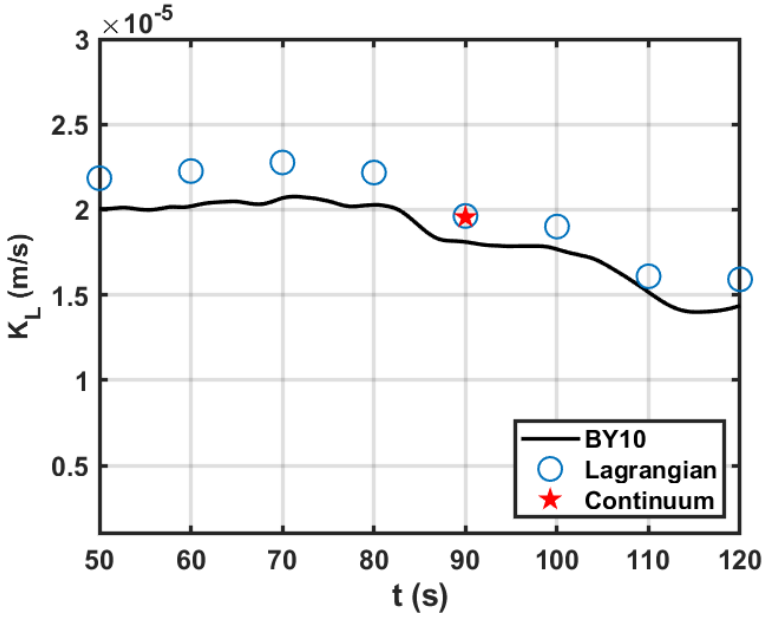

Figure 4.13: Gas transfer velocity K_L in time at $t = 90$s for simulation BY10 using RZ=10, RXY=5 and N=32.

Table 4.6: Relative error in the gas transfer velocity K_L

Simulations	RE(CL)	RE(CR)	RE(LR)
BT10	1.08 %	3.55 %	4.68 %
BT20	0.58 %	2.83 %	3.12 %
BY10	0.36 %	8.00 %	8.39 %

Table 4.6 represents the relative error,

$$RE(K_L) = \frac{|K_L(i) - K_{L(\overline{\tau})}(i)|}{K_L(i)} \times 100, \tag{4.37}$$

in the gas transfer velocity K_L. RE(CL) shows the error between the continuum and the Lagrangian method, RE(CR) is the error between the continuum method and the existing DNS, while RE(LR) is the error between the Lagrangian method and the existing DNS. It can be seen that RE(CR) is smaller than RE(LR) for all three simulations. At the same time, if we compare the results obtained with the continuum method to Lagrangian method, the error is significantly smaller than the error between either of the methods in the DNS (reference) results. The reason for the difference between the reference results and the continuum/Lagrangian results is either due to inaccuracies in Danckwerts' model or due to the fact that the velocity field used was not allowed to develop in time. It can be concluded that results of the gas transfer velocity K_L obtained using the mean surface age from the continuum method are in better agreement with the DNS results than the results from the Lagrangian method.

Chapter 5

Marangoni forces

In this chapter, a series of runs are presented and the results are analysed in order to study the effects of Marangoni forces on the instantaneous development of a buoyant convective instability for several Sc-numbers per simulation.

5.1 Introduction

Marangoni effects occur when surface tension is no longer constant due to differences in e.g. temperature or concentration along the surface. Such differences in surface tension may induce flow. For instance, when the surface tension gradient is produced by variations in temperature, the induced flow is usually known as thermocapillary flow (or thermal Marangoni effects). Whereas, when the surface tension gradient is produced by local differences changes in solute concentration, the resultant phenomenon is known as solute Marangoni effects, e.g., 'tears of wine'. In this chapter, the (horizontal) surface tension gradient was generated due to a buoyant instability generated by an unstable

vertical surface temperature gradient.

5.2 Methodology

Generally, the incompressible flow of a Newtonion fluid is described by the Navier-Stokes equations, which consist of the continuity equation

$$\frac{\partial u_i}{\partial x_i} = \frac{\partial u_1}{\partial x_1} + \frac{\partial u_2}{\partial x_2} + \frac{\partial u_3}{\partial x_3} = 0, \tag{5.1}$$

and the scalar momentum equations

$$\frac{\partial u_i}{\partial t} + \frac{\partial (u_i u_j)}{\partial x_j} = -\frac{\partial P}{\partial x_i} + \nu \frac{\partial^2 u_i}{\partial x_j \partial x_j} - \alpha \left(T_{b,0} - T\right) g \, \delta_{i3} \qquad i = 1, 2, 3, \tag{5.2}$$

where $u_1, u_2, u_3 = u, v, w$ are the components of velocity in the $x_1, x_2, x_3 = x, y, z$-directions, respectively, P is the generalised pressure (defined as a ratio of the static pressure and the constant density), t is time and ν is the kinematic viscosity. x_1, x_2 are in the horizontal directions, whereas x_3 is in the vertical direction. In the present work, the Navier-Stokes equations were non-dimensionalised by using a characteristic length scale L and velocity scale $U = \kappa/L$. The dimensionless terms were denoted by $(.^*)$ as ${x_j}^* = x_j/L$, ${u_j}^* = u_j L/\kappa$, $t^* = t\kappa/L^2$, $p^* = PL^2/\kappa^2$. The following replacement of the rescaled variables in the above equation 5.2 can be written as

$$\frac{\kappa^2}{L^3}\frac{\partial {u_i}^*}{\partial t^*} + \frac{\kappa^2}{L^3}\frac{\partial ({u_i}^* {u_j}^*)}{\partial {x_j}^*} = -\frac{\kappa^2}{L^3}\frac{\partial p^*}{\partial {x_i}^*} + \nu \frac{\kappa}{L^3}\frac{\partial^2 {u_i}^*}{\partial {x_j}^* \partial {x_j}^*} - \alpha \, \Delta T \, T^* \, g \, \delta_{i3} \qquad i = 1, 2, 3, \tag{5.3}$$

By dividing both sides of the above equation by κ^2/L^3, the dimensionless Navier-Stokes equations

$$\frac{\partial u_i{}^*}{\partial t^*} + \frac{\partial (u_i{}^* u_j{}^*)}{\partial x_j{}^*} = -\frac{\partial p^*}{\partial x_i{}^*} + Pr \frac{\partial^2 u_i{}^*}{\partial x_j{}^* \partial x_j{}^*} - Ra_L \, Pr \, T^* \, \delta_{i3} \qquad i = 1, 2, 3, \tag{5.4}$$

are obtained. The last term on the right-hand side in Eq. 5.4 represents the buoyancy force in z-direction where

$$Pr = \frac{\nu}{\kappa} \tag{5.5}$$

is the non-dimensional Prandtl number $Pr = 7$ corresponding to the ratio of momentum and thermal diffusivities of water at 293.15 K^{-1}. The temperature T was non-dimensionalised to obtain T^* by

$$T^* = \frac{T_{b,0} - T}{\Delta T}, \tag{5.6}$$

where $T_{b,0}$ is the temperatures in the bulk and $\Delta T = 1$ K. Note that the temperature at the surface is time dependent because of the prescribed constant heat flux at the surface. δ_{i3} is the Kronecker delta and the non-dimensional Rayleigh number is given by,

$$Ra_L = \frac{\alpha \Delta T g L^3}{\kappa \nu} \tag{5.7}$$

in which g is the gravitational acceleration, α is the thermal expansion factor in K^{-1} and ΔT is the temperature difference. The transport equation of the temperature T is

modelled by the convection-diffusion equation

$$\frac{\partial T}{\partial t} + \nabla.(T\vec{u}) = \kappa \nabla^2 T, \tag{5.8}$$

where κ is the thermal diffusion and ∇ and $\vec{u}$ are defined by

$$\nabla = \begin{bmatrix} \frac{\partial}{\partial x_1} \\ \frac{\partial}{\partial x_2} \\ \frac{\partial}{\partial x_3} \end{bmatrix}, \vec{u} = \begin{bmatrix} u_1 \\ u_2 \\ u_3 \end{bmatrix}. \tag{5.9}$$

Applying Einstein's summation convention to Eq. 5.8, implying summation over repeated indices, Eq. 5.8 can be expressed as

$$\frac{\partial T}{\partial t} + \frac{\partial (T u_j)}{\partial x_j} = \kappa \frac{\partial^2 T}{\partial x_j \partial x_j} \qquad j = 1, 2, 3. \tag{5.10}$$

As in the non-dimensionalisation of the Navier-Stokes equations, to obtain the dimensionless quantities $t^*, {x_i}^*$ and ${u_j}^*$, characteristic length L and velocity $U = \kappa/L$ scales are used,

$$\frac{\kappa}{L^2}\frac{\partial T^*}{\partial t^*} + \frac{\kappa}{L^2}\frac{\partial T^* {u_j}^*}{\partial {x_j}^*} = \frac{\kappa}{L^2}\frac{\partial^2 T^*}{\partial {x_j}^* \partial {x_j}^*} \qquad j = 1, 2, 3. \tag{5.11}$$

Note that to obtain Eq. 5.11, $T_{b,0}$ was subtracted from T (this is allowed because $\frac{\partial (T - T_{b,0})}{\partial t} = \frac{\partial T}{\partial t}$, $\frac{\partial^2 (T - T_{b,0})}{\partial x_j \partial x_j} = \frac{\partial^2 T}{\partial x_j \partial x_j}$ and $\frac{\partial (T - T_{b,0}) u_j}{\partial x_j} = \frac{\partial T u_j}{\partial x_j} - T_{b,0}\frac{\partial u_j}{\partial x_j} = \frac{\partial T u_j}{\partial x_j}$ as $\frac{\partial u_j}{\partial x_j} = 0$), and subsequently all terms in Eq. 5.10 were multiplied by the constant $-1/\delta T$. By dividing both sides of the above equation by κ/L^2, the dimensionless Navier-Stokes

equations can be written as

$$\frac{\partial T^*}{\partial t^*} + \frac{\partial T^* {u_j}^*}{\partial {x_j}^*} = \frac{\partial^2 T^*}{\partial {x_j}^* \partial {x_j}^*} \qquad j = 1, 2, 3. \tag{5.12}$$

Similarly, the transport mechanism of the dissolved scalar concentration C in a fluid is governed by the dimensionless 3D convection-diffusion equation of the non-dimensional scalar concentration C^*,

$$\frac{\partial C}{\partial t} + \frac{\partial C u_j}{\partial x_j} = D \frac{\partial^2 C}{\partial x_j \partial x_j} \qquad j = 1, 2, 3, \tag{5.13}$$

$$\frac{\kappa}{L^2}\frac{\partial C^*}{\partial t^*} + \frac{\kappa}{L^2}\frac{\partial C^* {u_j}^*}{\partial {x_j}^*} = \frac{D}{L^2}\frac{\partial^2 C^*}{\partial {x_j}^* \partial {x_j}^*} \qquad j = 1, 2, 3, \tag{5.14}$$

By dividing both sides of the above equation by κ/L^2, the dimensionless scalar transport equation can be written as

$$\frac{\partial C^*}{\partial t^*} + \frac{\partial C^* {u_j}^*}{\partial {x_j}^*} = \frac{D}{\kappa}\frac{\partial^2 C^*}{\partial {x_j}^* \partial {x_j}^*} \qquad j = 1, 2, 3, \tag{5.15}$$

Note that

$$\frac{D}{\kappa} = \frac{D}{\nu} \times \frac{\nu}{\kappa} = \frac{Pr}{Sc}, \tag{5.16}$$

where $Sc = \frac{\nu}{D}$ is the Schmidt number and $Pr = \frac{\nu}{\kappa}$ is the Prandtl number. Finally, the non-dimensional scalar transport equation

$$\frac{\partial C^*}{\partial t^*} + \frac{\partial C^* {u_j}^*}{\partial {x_j}^*} = \frac{Pr}{Sc}\frac{\partial^2 C^*}{\partial {x_j}^* \partial {x_j}^*} \qquad j = 1, 2, 3, \tag{5.17}$$

is obtained. Where

$$C^* = \frac{C - C_{b,0}}{C_s - C_{b,0}}, \tag{5.18}$$

with $C_{b,0}$ and C_s are the concentrations in the bulk and at the surface, respectively. Characteristic length (L) and velocity (U) scales that are used in the present study are $L = 0.01$ m and $U = \kappa/L$ m/s. Where $\kappa = 1.43 \times 10^{-6}$ m^2/s is the thermal diffusivity of water at 293.15 K [4, 92]. Using the characteristic velocity U defined above and the non-dimensionalisation of T shown in Eq: 5.6, the non-dimensional surface heat flux is defined by

$$\phi_T = - \left. \frac{\partial T^*}{\partial z^*} \right|_i . \tag{5.19}$$

Initially, the temperature and concentration were initialised by their respective exact solutions when only considering pure diffusion (given that the surface boundary condition for the temperature was a constant flux $-\partial T^*/\partial z^*$, while for the concentration constant value of $C^* = 1$ was prescribed at the surface), so that

$$T^*(\zeta^*, t^*) = - \left. \frac{\partial T^*}{\partial z^*} \right|_i \left[2\sqrt{\frac{t^*}{\pi}} \exp\left(\frac{-\zeta^{*2}}{4t^*} \right) - \zeta^* \mathrm{erfc}\left(\frac{\zeta^*}{2\sqrt{t^*}} \right) \right], \tag{5.20}$$

and

$$C^*(\zeta^*, t^*) = \mathrm{erfc}\left(\zeta^* \sqrt{\frac{Sc}{4\, Pr\, t^*}} \right), \tag{5.21}$$

respectively, where $\zeta^* = (L_z/L) - z^*$ is the non-dimensional distance to the surface and $z^* = x_3^*$. A thermal expansion factor $\alpha = 0.000207$ K^{-1} was employed, which is typical for water at 293.15 K. Initially, the velocity field was set to zero at $t = 0$. In the remainder, the star notation will be dropped and non-dimensionality will be implicitly

assumed.

5.3 Boundary conditions

In the simulation, periodic boundary conditions were employed in the horizontal direction for all variables. In the vertical direction, at the bottom, a free-slip boundary condition was used for the velocity to avoid fluid from leaving the computational domain. This boundary condition is given by

$$\begin{cases} \frac{\partial u}{\partial z} &= 0 \\ \frac{\partial v}{\partial z} &= 0 \\ w &= 0 \end{cases} . \tag{5.22}$$

At the top, the boundary condition for the velocity is given by

$$\begin{cases} \frac{\partial u}{\partial z} &= -Ma \left.\frac{\partial T}{\partial x}\right|_i \\ \frac{\partial v}{\partial z} &= -Ma \left.\frac{\partial T}{\partial y}\right|_i \\ w &= 0 \end{cases} , \tag{5.23}$$

where the non-dimensional Marangoni number Ma is defined as

$$Ma = \frac{-(\partial\sigma/\partial T)\Delta T L}{\mu\kappa}. \tag{5.24}$$

Vargaftik *et al.* [89] showed that the surface tension of water depends on the temperature and that this relation is approximately linear (see Fig. 5.1). From this we can

conclude that $\partial\sigma/\partial T$, and hence the Marangoni number, is approximately constant.

The values for the surface tension of water for the temperature ranging between $0-374°$C, given in Vargaftik's reference book [88] has been widely used in recent years. Fig. 5.1 shows a linear relationship between surface tension σ and temperature T. In the present work, the water temperature was set to 20° C.

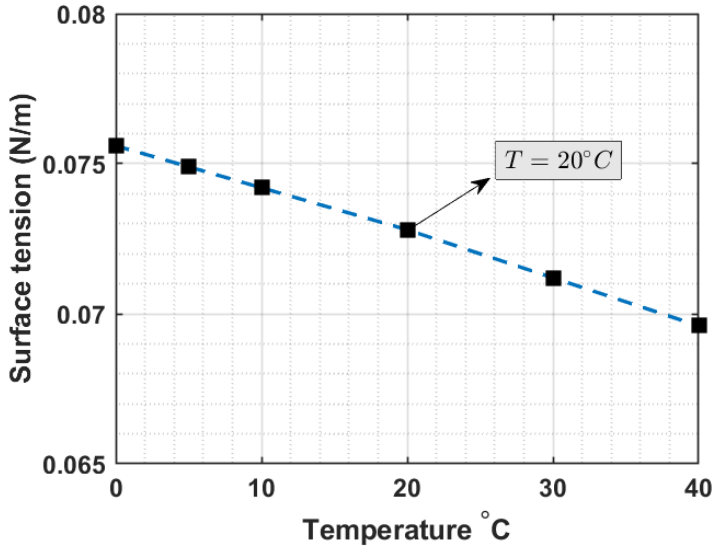

Figure 5.1: Surface tension of water, data taken from [89]

5.4 Overview of the simulations

An overview of the simulations is provided in Table 5.1. The governing equations introduced above were solved on a non-uniform staggered mesh (where all scalars are defined in the middle of the mesh cells, while the velocities are defined at the faces) using the in house KCFlo code as described in Kubrak *et al.* [49]. This code was especially developed to allow for an accurate simulation of low diffusivity scalar transport on a

sufficiently fine mesh, while using a coarser mesh for the flow simulation. The transport of low solubility (in water) atmospheric gases across the air-water interface is controlled by a very thin concentration boundary layer on the water side. To accurately resolve scalar convection a fifth order WENO scheme was employed [58], while a fourth order central finite difference scheme was used for the diffusive terms. For the time integration the three stage Runge-Kutta method as described in Liu *et al.* [58] was employed.

For the flow solver, the convective terms were solved using fourth order kinetic energy conserving discretization described in [91], while the diffusive term was solved using the fourth order central scheme. After substituting the descritized momentum equations into the continuity equation a Poison equation for the pressure was obtained. This Poison equation for the pressure was solved using the conjugate gradient method with simple diagonal decomposition. Time integration was performed using the second order Adams-Bashforth method.

In the present direct numerical simulation (DNS) a $L_x \times L_y \times L_z = 5L \times 5L \times 5L$ computational domain was employed. Simultaneously with the flow, five scalar convection diffusion equations were solved. The first scalar, the temperature, is non passive as it affects the flow through buoyancy forces. The other scalars are passive and represent the transport of atmospheric gases. The Prandtl number for the temperature was $Pr = 7$ and the Schmidt numbers for the mass transport were $Sc = 16, 50, 100, 200$. The latter simulations will allow a non biased comparison of the affect of Schmidt number on the gas transfer velocity K_L. The setup of the computational simulations was inspired by the experiments carried out by Jirka *et al.* [41]. A $200 \times 200 \times 252$ baseline mesh was employed to solved both the flow, temperature and the scalar transport

equation at $Sc = 16$. For the scalar transport equations at higher Schmidt numbers ($Sc = 50, 100, 200$) the basemesh was refined by a factor of two in all directions.

The mesh is stretched in the z-direction in order to obtain a much finer resolution near the air-water interface. The node distribution is given by

$$z(k) = \left[1 - \frac{\tanh(z_\phi)}{\tanh(z_1)}\right] z(0) + \left[\frac{\tanh(z_\phi)}{\tanh(z_1)}\right] z(N_z), \tag{5.25}$$

for $k = 1, ..., N_z - 1$, with

$$z_1 = \frac{\psi}{2}, \tag{5.26}$$

$$z_\phi = \frac{k z_1}{N_z}, \tag{5.27}$$

where N_z is the number of nodes in the z-direction. The mesh stretching is governed by the parameter ψ, which is set to $\psi = 3$ in all simulation.

Table 5.1: Overview of simulations. In all simulations the Prandtl number Pr was set to 7 typically for water at 293.15 K, 5L × 5L × 5L Domain and 200 × 200 × 252 base mesh size is used. The Kolmogorov scale is denoted by η.

				L_B				
Case	Ma	ϕ_T	η	$Pr = 7$	$Sc = 16$	$Sc = 50$	$Sc = 100$	$Sc = 200$
MB01	0	0.777	0.2546	0.096	0.064	0.036	0.025	0.018
MB02	0	1.5	0.2010	0.076	0.050	0.028	0.020	0.014
MB03	0	2.33	0.1746	0.066	0.044	0.025	0.0175	0.012
MB11	70	0.777	0.1945	0.074	0.049	0.028	0.019	0.014
MB12	70	1.5	0.1465	0.055	0.037	0.021	0.015	0.010
MB13	70	2.33	0.1301	0.049	0.033	0.018	0.013	0.009
MB51	350	0.777	0.1055	0.040	0.026	0.015	0.011	0.007
MB52	350	1.5	0.0814	0.031	0.020	0.012	0.008	0.006
MB53	350	2.33	0.0741	0.028	0.019	0.010	0.007	0.005
MB10	1049	2.33	0.0517	0.020	0.013	0.007	0.005	0.004

The simulations were performed on a massively parallel super computer using 256 processing cores. Parallelisation was performed by dividing the computational mesh into blocks of equal size. Each block was given its own processing core. Communication between the processes was performed using the standard Message Passing Interface (MPI) protocol.

5.5 Grid refinement study

A grid refinement study has been carried out to assess the adequacy of the resolution used for the base mesh. For this purpose three simulations were performed using exactly the same boundary and initial conditions (including the same disturbance added to the

temperature field). The simulations were performed on different meshes, where MB10 was carried out on the base mesh while the other two simulations (MB20 and MB30) were carried out on refined meshes (see Table 5.2).

The choice of grid spacing in the upper part of the computational domain was based on the Grötzbach criterion [26]. There are two requirements to fulfill this criterion. The first requirement is that the vertical grid resolution near the air-water interface is fine enough to resolve the Batchelor scale L_B. The second requirement is that in the upper part of the computational domain, the geometric mean of the grid cells $\overline{\Delta}$ is smaller than πL_B, i.e.

$$\overline{\Delta} = (\Delta x \times \Delta y \times \Delta z)^{1/3} \leq \pi L_B. \tag{5.28}$$

To further ensure an accurate resolution of all near-surface details of the buoyant instability down to the Batchelor scale, a grid refinement study was performed for the base mesh. To deal with this, in a separate simulation, similar to MB20 (see Table 5.2), random disturbances were added to the temperature field at $t = 10\,\mathrm{s}$. This simulation was subsequently run for a further 2 s. After which the resulting temperature field was saved and used as the initial condition for the temperature in MB10, MB20 and MB30. Between $t = 12\,\mathrm{s}$ and $t = 90\,\mathrm{s}$ the disturbance was allowed to develop so that falling plumes were obtained. This method allowed a direct comparison of the instantaneous temperature and flow fields calculated on different meshes using various Schmidt numbers. MB10 has the coarsest mesh with $200 \times 200 \times 252$ points, compared to the coarsest mesh, the mesh used in MB20 was refined by a factor of approximately $1.3 - 1.5$ times in each direction, while the mesh used in MB30 was refined by a factor of 2 in the x and y-directions and a factor of 1.6 in the z-direction (see Table 5.2). Note that the

temperature with $Pr = 7$ and the concentration with the smallest Schmidt number ($Sc = 16$) were solved on the base mesh, while the concentrations with larger Schmidt numbers ($Sc = 50, 100, 200$) were solved on a mesh that was refined by a factor of 2 in all directions.

Table 5.2: Grid refinement study, domain size= 5L × 5L × 5L, $Ma = 1049$, $\pi \mathrm{L}_{B,Sc=16} = 0.041$, $\pi \mathrm{L}_{B,Sc=200} = 0.0116$.

Simulation	Grid ($Pr = 7, Sc = 16$)	Grid ($Sc = 50 - 200$)	$\overline{\Delta}_{Sc=16}$	$\overline{\Delta}_{Sc=50-200}$
MB10	200 × 200 × 252	400 × 400 × 504	0.0155	0.0078
MB20	296 × 296 × 330	592 × 592 × 660	0.0109	0.0055
MB30	400 × 400 × 402	800 × 800 × 804	0.0083	0.0042

The results of the grid refinement study for the velocity are shown in Figures 5.2, 5.3 and 5.4, where profiles of the instantaneous u, v and w velocities at $t = 80$s, $z/L = 4.5$ and at $y/L = 2.5$ and $x/L = 2.5$ in parts (a) and (b) of the above figures, respectively.

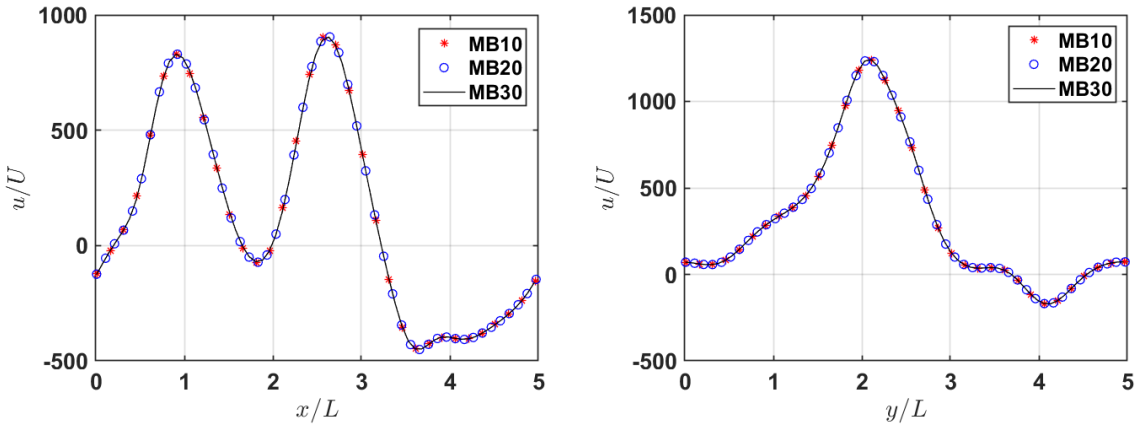

(a) (b)

Figure 5.2: u-velocity component profile after $t = 80$s at $z/L = 4.5$ using different grid sizes. Only every sixth data point is shown.

The velocities were all normalised using the velocity scale $U = \kappa/L$. All profiles were found to be in excellent agreement. The largest difference observed between the velocities in the various simulations was less than 10^{-8}, which is negligibly small.

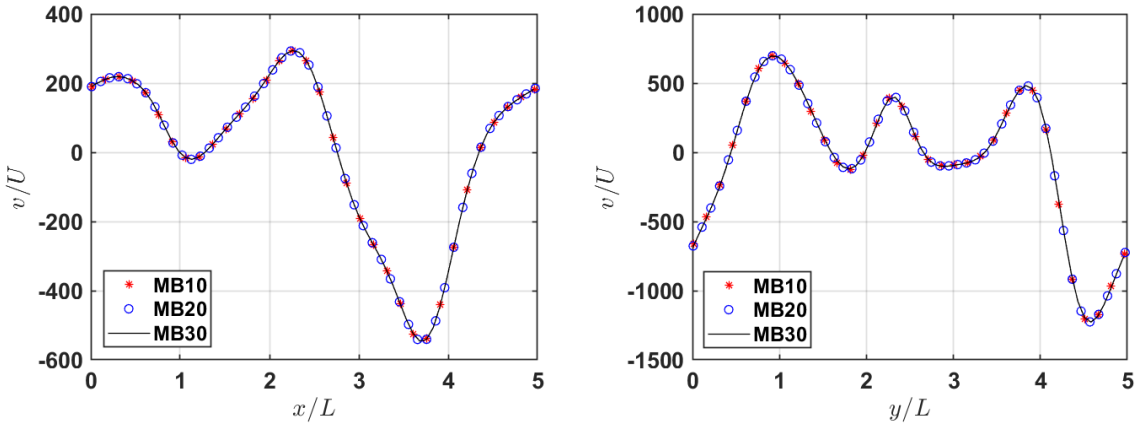

(a) (b)

Figure 5.3: v-velocity component profile after $t = 80$s at $z/L = 4.5$ using different grid sizes. Only every sixth data point is shown.

Based on the similarities between the results obtained on three meshes, it can be concluded that the mesh size used in MB10 was sufficiently fine to accurately resolve the buoyant instability.

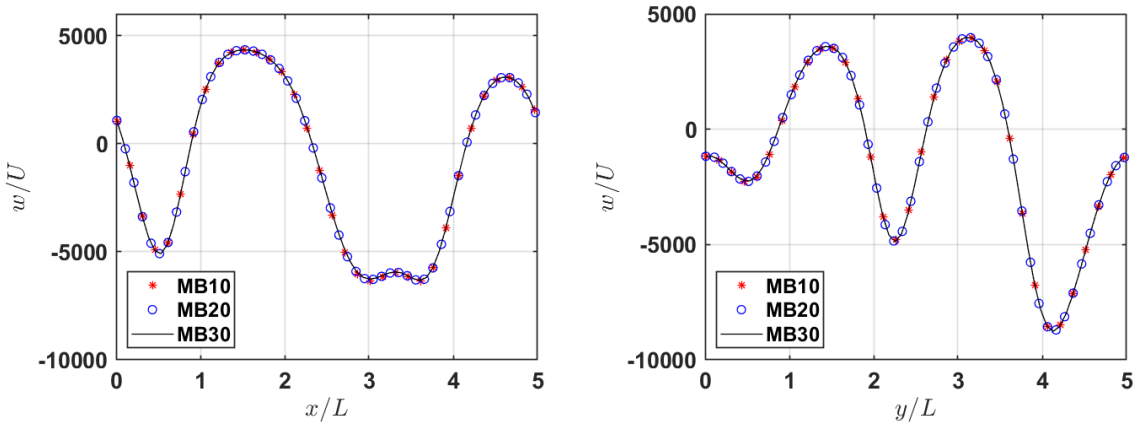

(a) (b)

Figure 5.4: w-velocity component profile after $t = 80$s at $z/L = 4.5$ using different grid sizes. Only every sixth data point is shown.

Profiles of the temperature obtained in MB10, MB20, MB30 at $t = 80$s and $z/L = 4.5$ are shown in Figure 5.5. Figure 5.5a shows the profiles at $y/L = 2.5$, while (b) shows the profiles at $x/L = 2.5$. It can be seen that in both plots the temperature profiles are in excellent agreement so that we can conclude that the base mesh of MB10 is also sufficiently fine to fully resolve the temperature field.

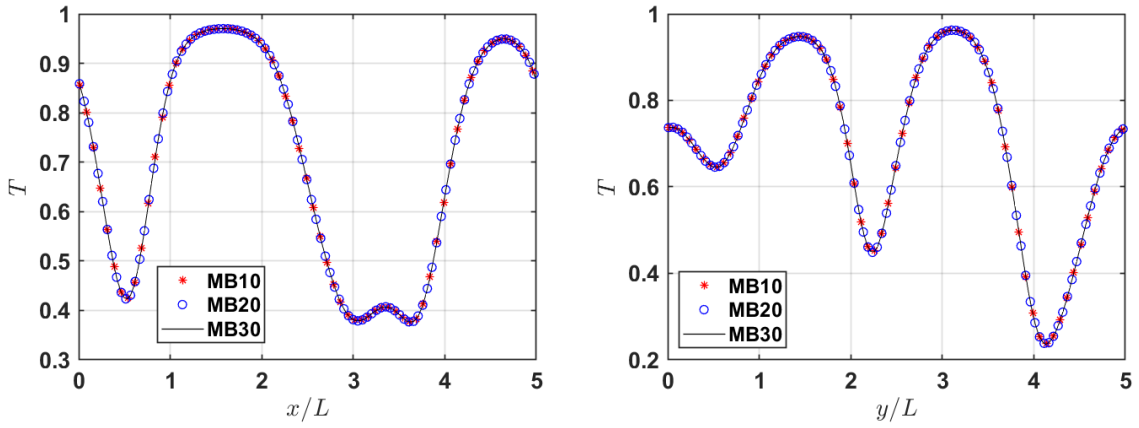

(a) (b)

Figure 5.5: Temperature profile ($Ma = 1049$) after $t = 80$s showing (a) T at the center line $y/L = 2.5$ and (b) at $x/L = 2.5$ and $z/L = 4.5$ obtained using different grid sizes (see Table. 5.2). Only every third data point is shown.

Similar to the temperature plot above, in Figure 5.6, the scalar concentration profiles of MB10, MB20 and MB30, obtained on the base mesh at $Sc = 16$, $t = 80$s and $z/L = 4.5$ are compared. Also for this quantity, an improvement of the resolution across the entire computational domain in MB20 and MB30 did not lead to any further (noticeable) improvements in the results obtained on the MB10 mesh. Based on that it can be concluded that the base mesh of MB10 was sufficiently fine to resolve scalars up to $Sc = 16$. This implies that on the refined meshes (which are refined by a factor of 2 in all directions) we can fully resolve scalars up to $Sc = 64$. Based on the fact that above the Grötzbach criterion was shown to be valid in the upper part of the computational domain for all scalars up to $Sc = 200$ we believe that the grid refinement study for the refined meshes would also show a good agreement for the scalar concentrations of the higher Schmidt numbers.

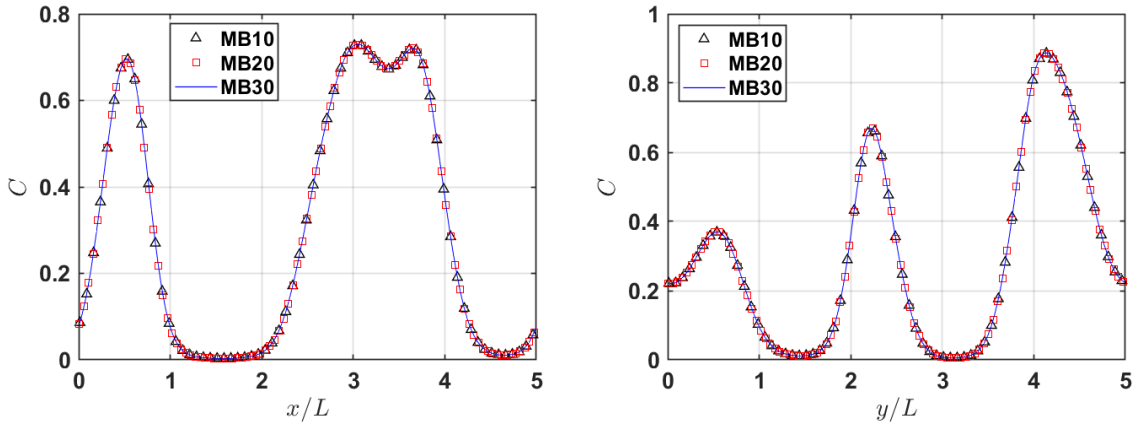

(a) (b)

Figure 5.6: Concentration profile ($Ma = 1049$) after $t = 80\,\mathrm{s}$ showing (a) C at the center line $y/L = 2.5$ and (b) at $x/L = 2.5$ and $z/L = 4.5$ from simulations with different scalar grid refinement factors (see Table. 5.2). Only every third data point is shown.

Hence, grid MB10 with refinement factor 2 was used in the remainder of this chapter to obtain results at higher Schmidt numbers.

5.6 Flow field

The Marangoni effect on the turbulent flow statistics was evaluated for a range of Marangoni numbers ($Ma = 0, 70, 350$) and $\phi_T = 0.777$ at time $t = 150$s. The horizontal velocity fluctuations, displayed in Figure 5.7, were obtained by averaging the horizontal velocity components in time and in homogeneous (horizontal) directions. Both the horizontal and vertical velocity fluctuation level change due to the Marangoni effect. For $Ma = 0$ (case MB01), at the surface u_{rms} has a local maximum and zero gradient. Further below, u_{rms} eventually reduces with distance to the surface until it becomes

virtually independent of z. For $Ma = 70$ (case MB11), the Marangoni effect causes the gradient of u_{rms} at the surface to be non-zero. With distance to the surface u_{rms} keeps on decreasing until $z \approx 4.3L$ after which it becomes independent of depth. Finally, the case with the largest Marangoni number of $Ma = 350$ (case MB51) behaves very similar to the case MB11. It can be seen that also for this case u_{rms} gradually reduces with distance to the surface until it becomes independent of depth. Note that with increasing Marangoni number the horizontal fluctuations at the surface were found to increase. This is the direct consequence of the Marangoni forces acting at the surface to promote Rayleigh instability.

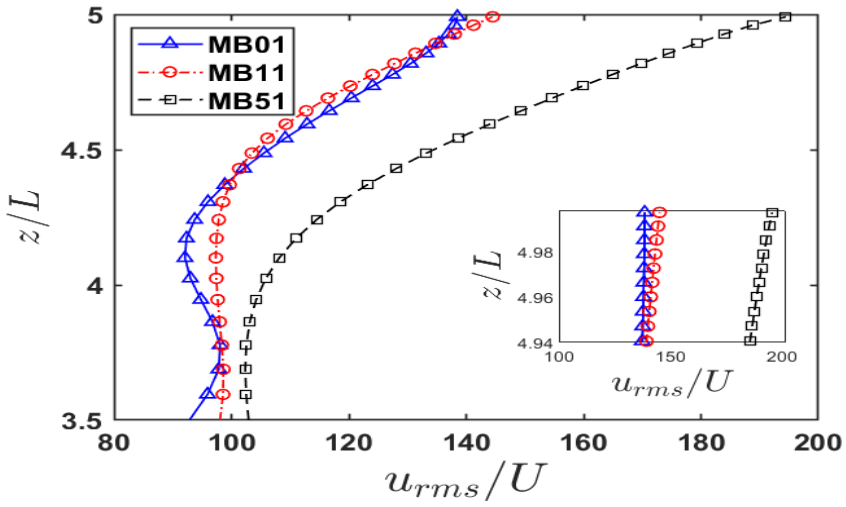

Figure 5.7: Marangoni effects on u_{rms} at time $t = 150$s. Only every fifth data point is shown.

In Figure 5.8, it can be seen that near the surface w_{rms} decreases linearly with distance to the surface for all Marangoni numbers. Further away from the surface this increase slowly reduces. In the insert can be seen that, very close to the surface, the

gradient of the w_{rms} becomes steeper with increasing Marangoni number, which may promote the vertical mixing of concentration and temperature. Note that the non-dimensional surface heat flux in Figures 5.7 and 5.8 was fixed to a value of $\phi_T = 0.777$ and u_{rms}, w_{rms} were normalised using the velocity scale $U = \kappa/L$.

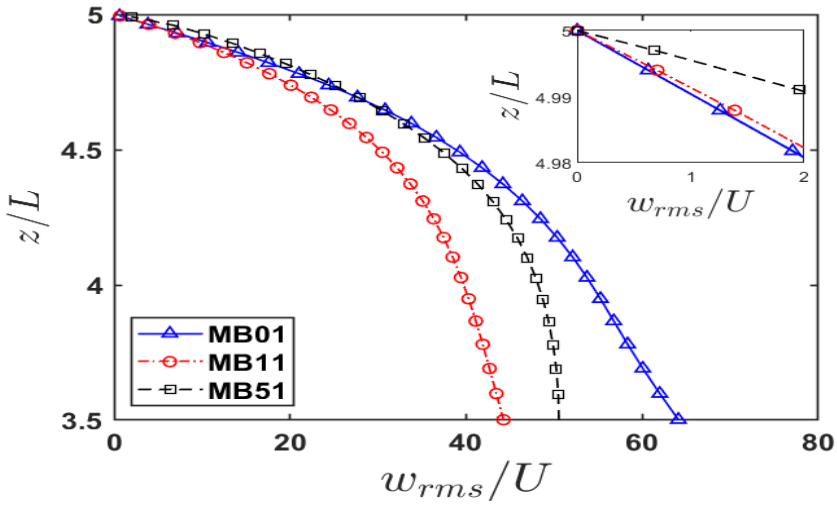

Figure 5.8: Marangoni effects on w_{rms} at time $t = 150$s. Only every fifth data point is shown.

Figure 5.9 shows that the integral length scales tend to grow in time, which is in agreement with growth in time of the convection cells shown in Figure 5.14. The integral length scale was obtained using two point correlations of the surface divergence

$$\beta = \partial u/\partial x + \partial v/\partial y, \tag{5.29}$$

which is directly related to the strength of the Rayleigh instability at the surface. In the Figure 5.9 it can be seen that the size of the integral length scale initially tends to increase in all simulations. In simulation MB03, where $Ma = 0$, this increase is

most significant. With increasing Marangoni number it can be seen that the increase in integral length scale becomes smaller and smaller. For the highest Marangoni number, after the initial increase, the integral length scale remains virtually constant for a significant time period of more than 90 s. It can be concluded that the Marangoni forces tend to limit the growth of the integral length scale. As shown in [92] such small integral length scales (corresponding to small convection cells) tend to have a relatively large gas transfer velocity compared to larger convection cells. All integral length scales show a small dip immediately after plumes of cold water start to fall down, these dips can be seen at $t \approx 20$ for MB53, at $t \approx 55$ for MB13 and at $t \approx 78$ for MB03.

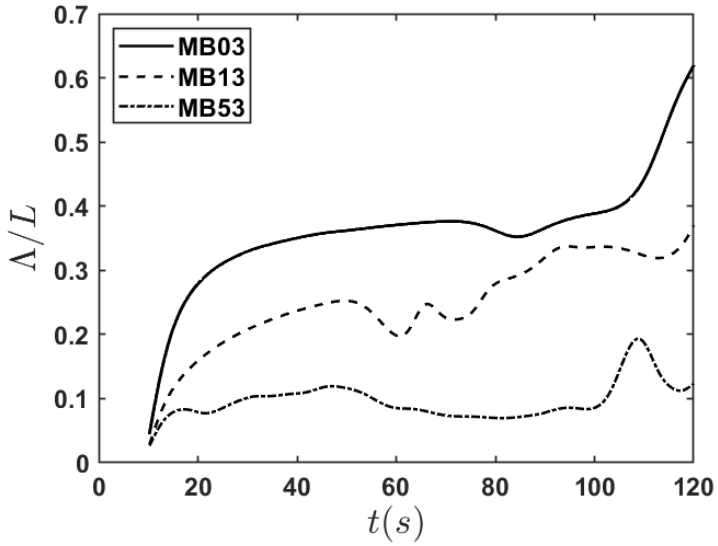

Figure 5.9: Influence of Marangoni number $Ma = 0, 70, 350$ on integral length scale.

The contour maps in Figure 5.10 show the effects of Marangoni forces on the surface divergence β by comparing simulations at a fixed non-dimensional surface heat flux of 2.33 at two Marangoni numbers, $Ma = 0$ (case MB03) and $Ma = 70$ (case MB13).

The underlying mechanism play a role in the exchange of heat and saturated fluid between the bulk and the surface is best illustrated in Figure 5.10b. The yellow areas correspond to positive surface divergence β (see Eq: 5.29) and indicate upwelling of unsaturated fluid from the bulk, which upon reaching the surface spreads out along the surface in radial directions. While it travels along the surface the fluid cooled down and becomes more and more saturated. Towards the sides of the convection cells the fluid has cools down so much that it sinks down back into the bulk, forming sheets of falling saturated fluid. The later is indicated by the dark blue boundaries of the convection cells, corresponding to negative surface divergence. Compared to Figure 5.10b, where $Ma = 70$, at $Ma = 0$ (shown in part (a)) the convection cells are not fully formed yet, indicating a much reduced heat and gas exchange between the surface and the bulk. Hence, it can be concluded that the Maragoni forces tend to aid the Rayleigh instability that drives buoyant convection.

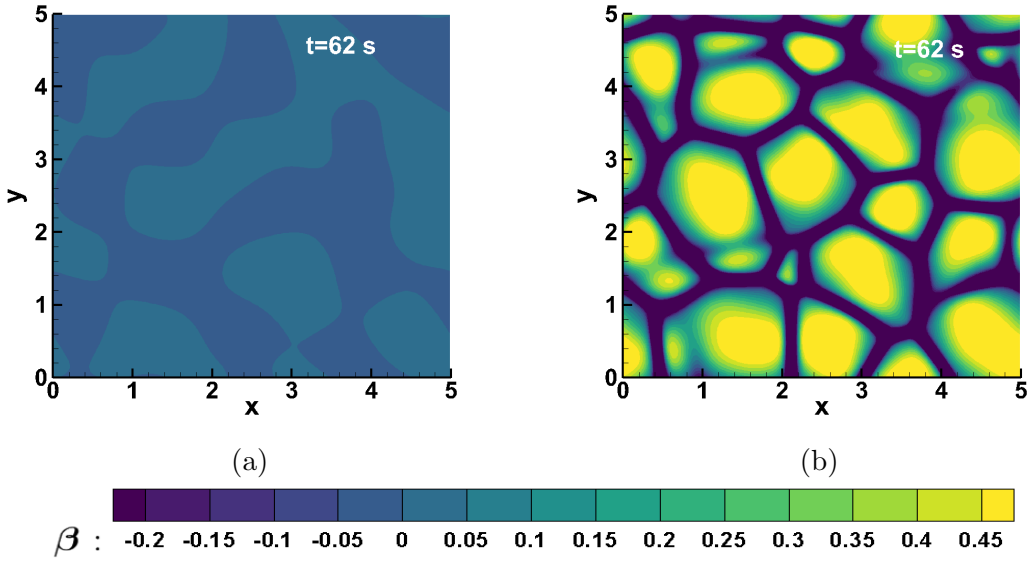

Figure 5.10: Surface divergence contours from simulation (a) MB03 and (b) MB13

Above it can be seen that the formation of the convection cells at $Ma = 0$ just started at $t = 62$s. As can be seen in Figure 5.11, at $t = 78$s the convection cells become much stronger and clear areas of strong upwelling and downwelling can be seen. At the same time, the simulation MB13 at $Ma = 70$ the average size of the convection cells can be seen to increase as the instability develops. At $t = 96$s convection cells for $Ma = 0$ are well defined as can be seen in Figure 5.12a. Also, in this figure we can see that for the simulation with $Ma = 70$, the size of the convection cells further increased. Finally, in Figure 5.12c also the development of the convection cells at $Ma = 1049$ is shown. Here it can be seen that the size of the convection cells are much smaller than in the other two simulations and also their shapes have become quite irregular.

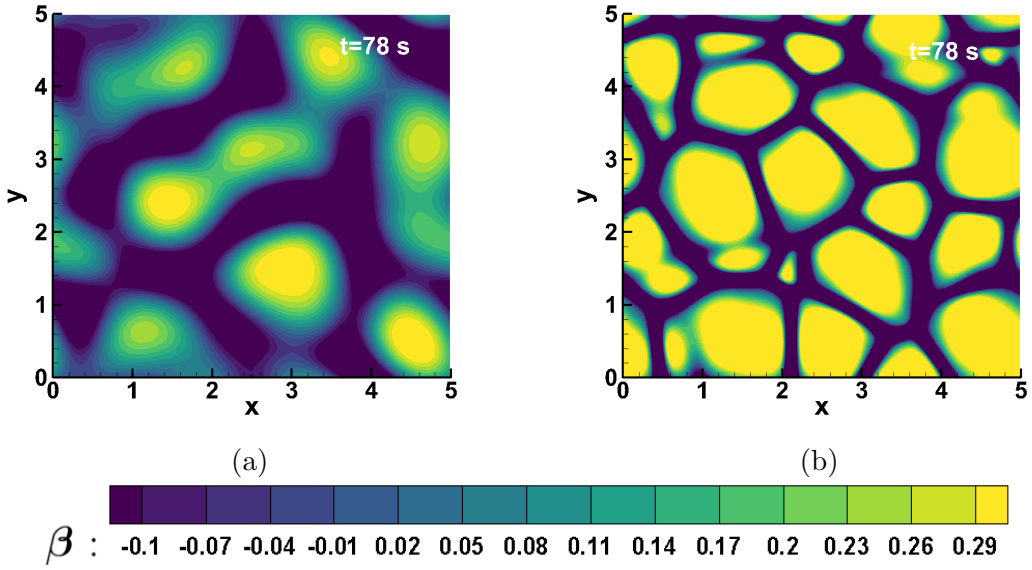

Figure 5.11: Snapshots of instantaneous surface divergence contours from simulation (a) MB03 and (b) MB13

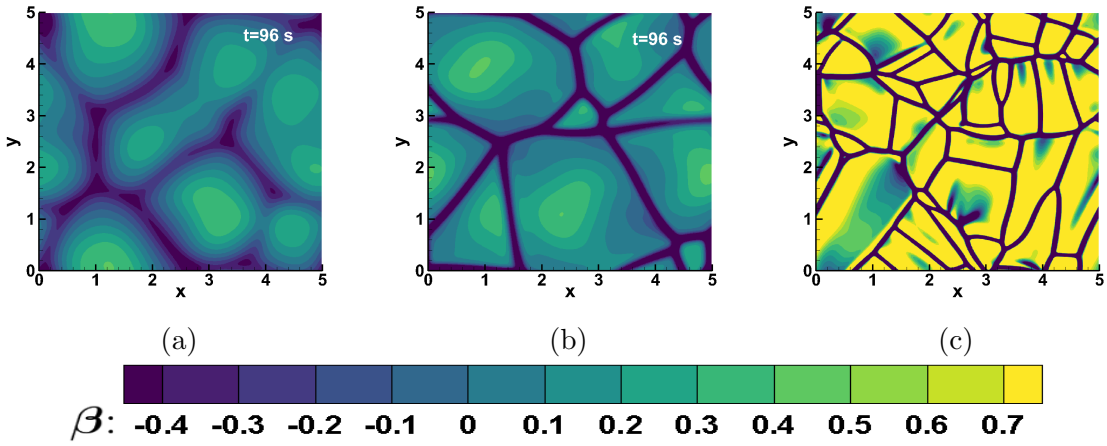

Figure 5.12: Surface divergence contours from simulation (a) MB03, (b) MB13 and (c) MB10

5.6.1 Instantaneous scalar structures near the surface

For a fixed non-dimensional surface heat flux of $\phi_T = 1.5$, Figure 5.13 compares the Marangoni effect by showing colour contours of the instantaneous interfacial gas concentration at $Sc = 50$ and $t = 77$s for (a) $Ma = 0$ (case MB03) and (b) $Ma = 70$ (case MB13). The high gas concentration areas (in yellow) identify saturated fluids that is transported downwards from the surface, while the low concentration areas (in blue) identify unsaturated fluid that is washed up from the bulk. Compared to $Ma = 0$ at $Ma = 70$, the saturation at the top of the convection cells is significantly lower and the convection cells are separated from each other by much smaller areas of fully saturated flow.

To study the effect of Marangoni number on the temperature distribution at the surface, in Figure 5.14 colour contours are plotted of the instantaneous temperature at $t = 87$s for the cases MB03 ($Ma = 0$), MB13 ($Ma = 70$) and MB10 ($Ma = 1049$). It can be seen that the Marangoni effect promotes the buoyant (Rayleigh) instability so that, compared to $Ma = 0$, at $Ma = 70$ the convection cells are much clearer defined and also slightly larger in number, while at $Ma = 1049$ a very large number of convection cells can be seen with a quite irregular shape and size distribution.

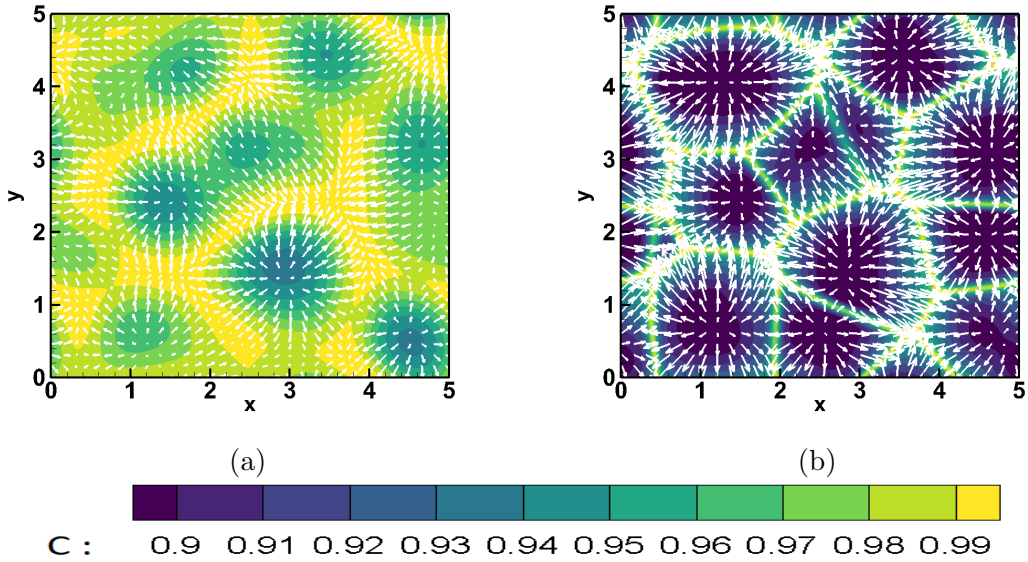

Figure 5.13: Velocity vectors and magnitude (contours) of scalar distribution for $Sc = 50$ at the surface. Snapshots taken at time $t = 77$ s from simulation (a) MB03 and (b) MB13.

As compared to the above explanation, in Figure 5.16 and 5.18, for $Ma = 350$, a strong Marangoni effect can be seen at the surface in temperature and concentration distribution, respectively.

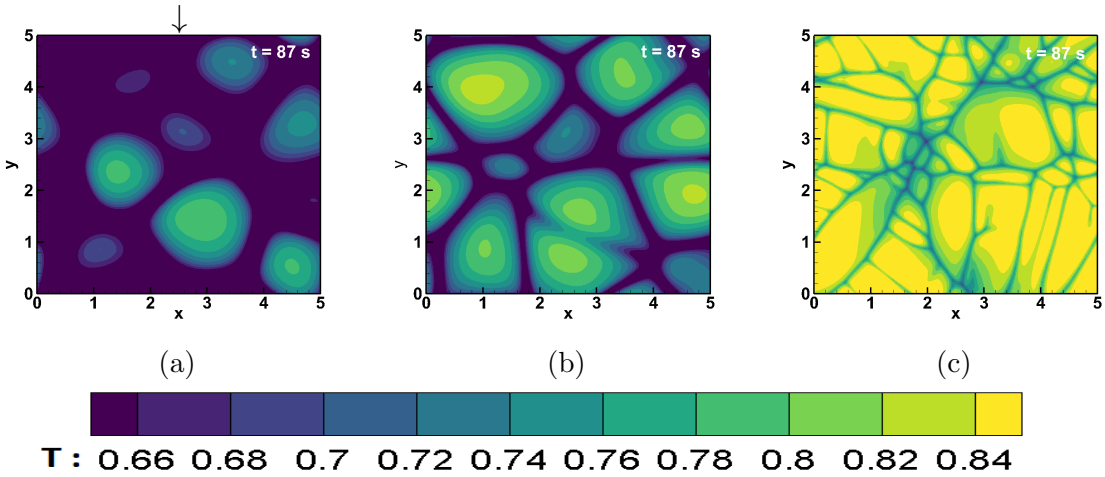

Figure 5.14: Temperature distribution at the surface from simulation (a) MB03 (b) MB13 and (c) MB10.

Rayleigh instability is promoted due to the Marangoni forces and the buoyancy instability does not becomes stronger (when the fluid plumes plunges down), so that the plumes does not penetrate deeper into the bullk very far as compared to $Ma = 0$ (see Figures 5.16 and 5.18). This is due to the fact that there is not much cold water at the surface being transported down, resulting in convection to be more limited close to the surface before it diffuses.

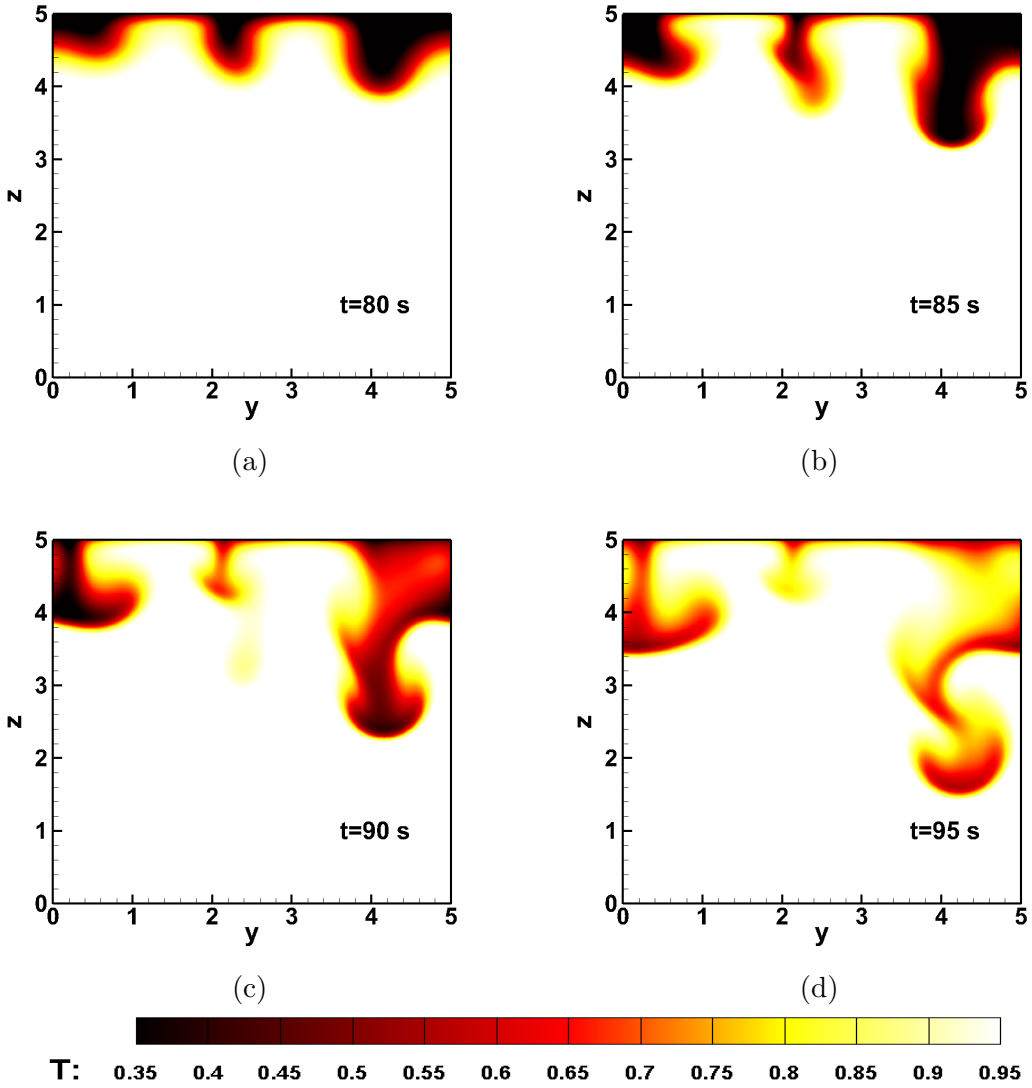

Figure 5.15: Temperature contours in the cross section at $x/L = 2.5$ (identified by the arrow in Fig. 5.14a) of simulation MB03.

Figures 5.15 and 5.16 show contours of the temperature in the plane $x/L = 2.5$ illustrating the initial development of the falling plumes at $Ma = 0$ (Figure 5.15) and $Ma = 350$ (Figure 5.16).

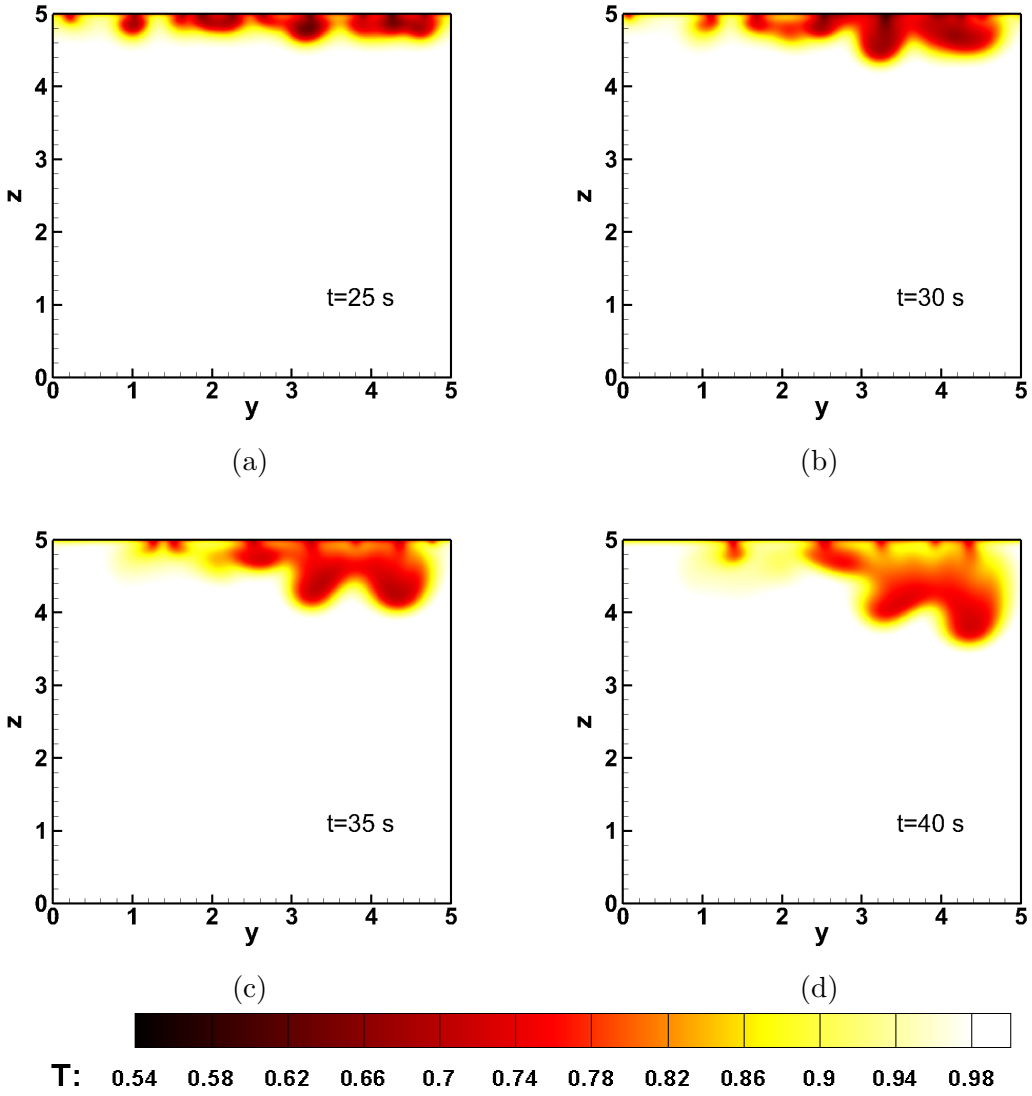

Figure 5.16: Temperature visualization from the simulation MB53.

As already noticed above, the Marangoni forces tend to promote the buoyant instability, which is confirmed by the much earlier formation of plumes at $Ma = 350$ in comparison to $Ma = 0$. Because of this, the amount of heat lost at the surface before

plumes start falling down becomes less with increasing Marangoni number.

As a result, the buoyancy force underneath the surface that is responsible for the plumes to penetrate into the bulk becomes less. This can clearly be seen by the limited penetration depth of the plumes at $Ma = 350$, which tend to remain relatively close to the surface (in a period of 15s) it only reaches depth of $\Delta z/L \approx 1.5$. The plumes at $Ma = 0$ which start to fall much later, on the other hand, penetrate much deeper into the bulk with $\Delta z/L \approx 3.5$. Also, because of the much higher penetration velocity at $Ma = 0$ the thermal plumes a typical mushroom shape which is related to the formation of a toroidal vortex around the head of the falling plume. At $Ma = 350$ because of the low penetration velocity combine with the relatively high diffusion no such mushroom shapes are observed.

At the same time instances used in the comparison of the temperature field of the falling plumes in Figures 5.15 and 5.16, in Figures 5.17 and 5.18 the contours of the scalar concentration at $Sc = 100$ are compared for $Ma = 0$ and $Ma = 350$. The main differences between the scalar concentration and the temperature are the boundary condition at the surface and the ratio of the thermal/scalar diffusivity to the kinematic viscosity, i.e. $Pr = 7$ versus $Sc = 100$. While the effect of the different boundary condition is not very crucial, the effect of the much smaller diffusivity of the gas concentration (compared to the temperature) leads to much finer gas concentration structures that partially overlap with the thermal plumes.

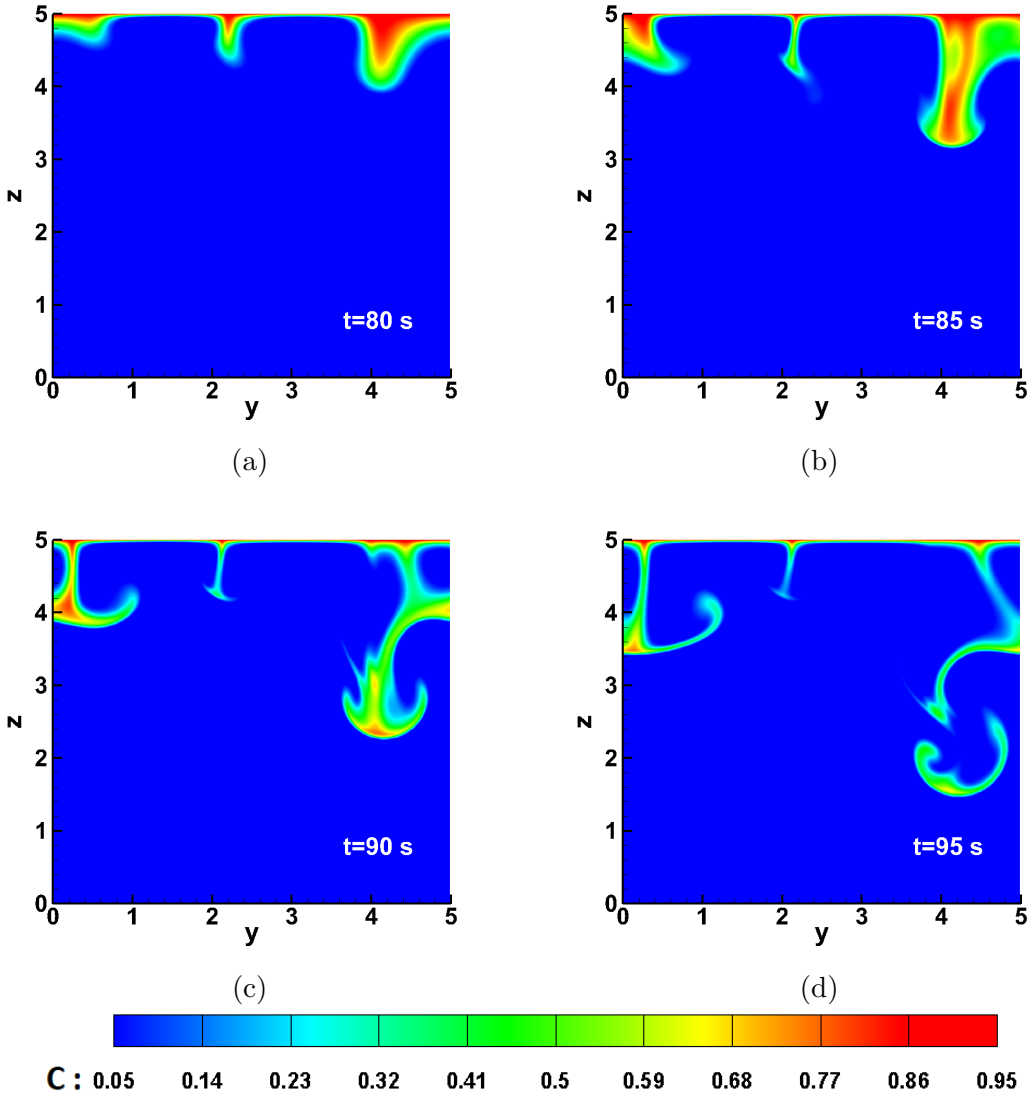

Figure 5.17: Visualization of scalar transport for $Sc = 100$ from the simulation MB03.

The reason for this is that the buoyancy forces that cause the plumes to form and fall down are completely determined by the temperature. At the moment the plumes fall down the thermal boundary layer at the surface is much thicker than the concentration

boundary layer at $Sc = 100$. When the cold fluids plunges down it also takes gas-saturated fluid from the upper part of the boundary layer (close to the surface) with it. This is a further reason why the gas concentration structures introduced into the bulk by the falling plumes tend to be much finer than the thermal structures.

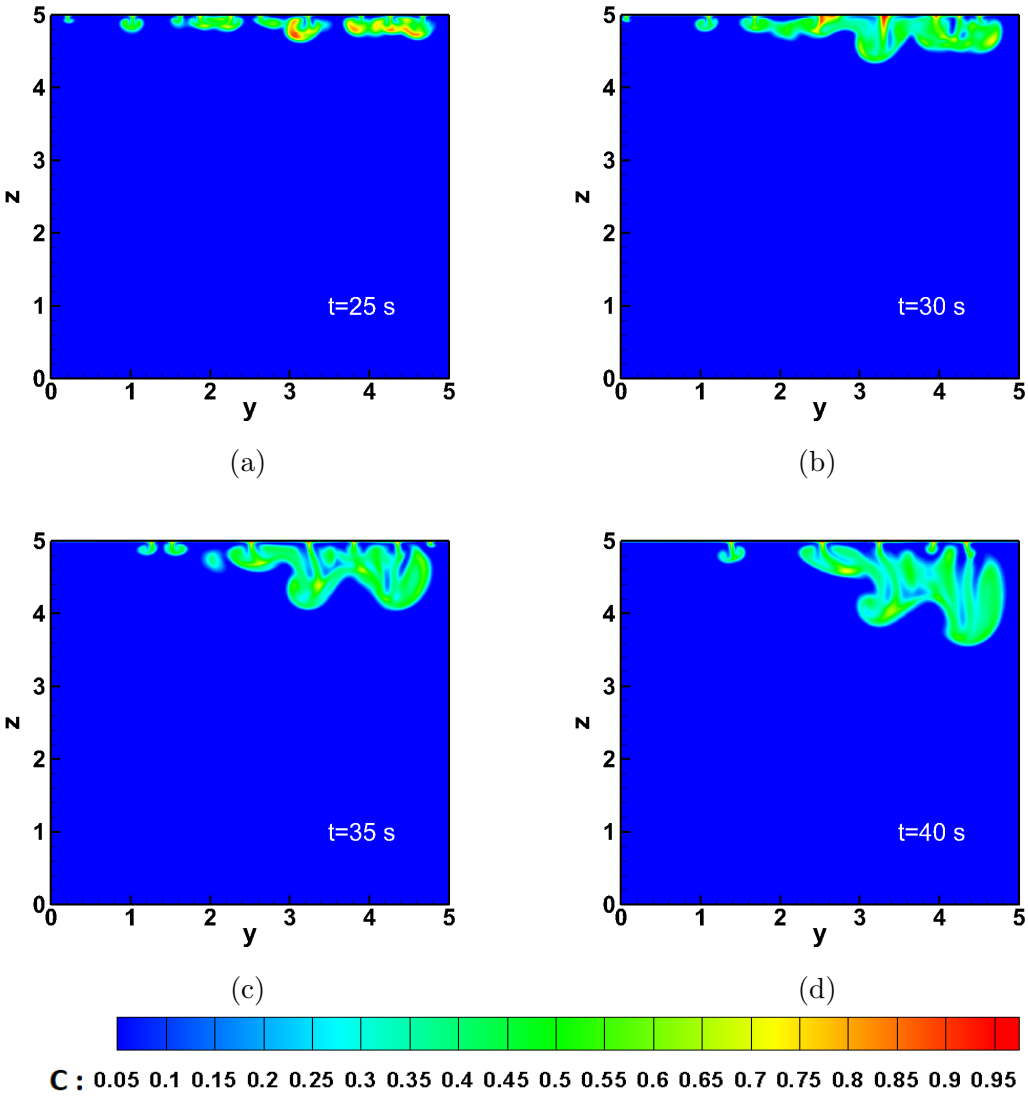

Figure 5.18: Visualization of scalar transport for $Sc = 100$ from the simulation MB53.

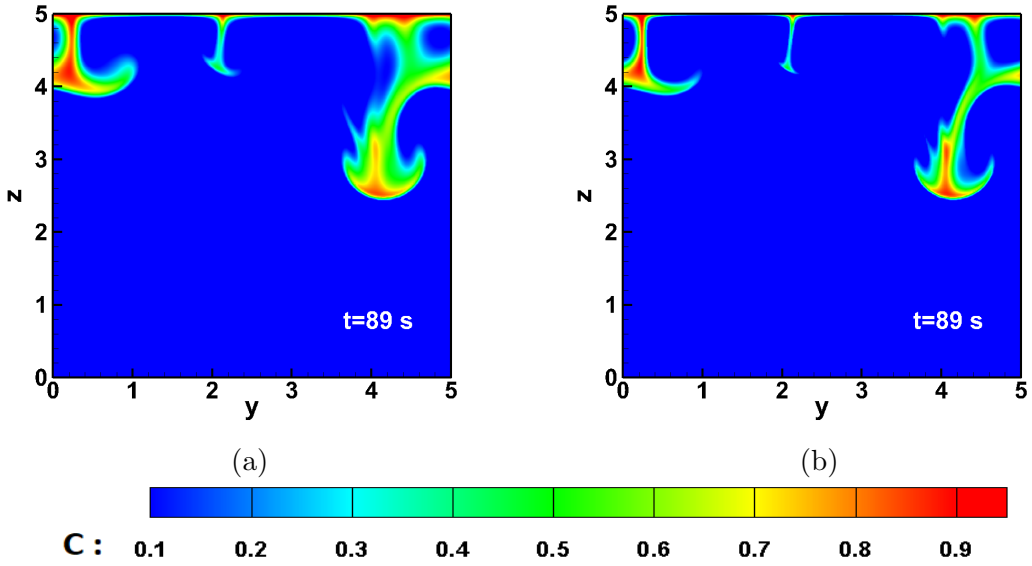

Figure 5.19: Visualization of scalar transport from the simulation MB03 for the cases (a) $Sc = 16$ and (b) $Sc = 200$. The thickness of boundary layer reduces with increasing Schmidt number.

Figure 5.19 compares contours of the scalar distribution for $Sc = 16$ and 200 in the cross-section at $x/L = 2.5$ from the simulation MB03. The snapshots show the distribution of the scalar concentration at $t = 89$s. As mentioned above, the plumes of cold water plunge down into the bulk take saturated flow with them from the upper part of the boundary layer. As the concentration boundary layer at $Sc = 16$ is much thicker than the boundary layer at $Sc = 200$, relatively more saturated fluid is transported into the bulk. As a consequence the mushroom structures at $Sc = 16$ are thicker than the very fine structures observed in $Sc = 200$. In the corresponding contour plot of the temperature (see e.g. Fig. 5.15c), because of the increased diffusivity, the cold water plumes are even thicker than the high concentration plumes at $Sc = 16$.

5.7 Scalar transport

5.7.1 Concentration boundary layer

Figure 5.20a shows the growth of boundary layer (BL) thickness for various values of the non-dimensional surface heat flux $\phi_T = 0.777, 1.5, 2.33$ with a fixed $Ma = 0$.

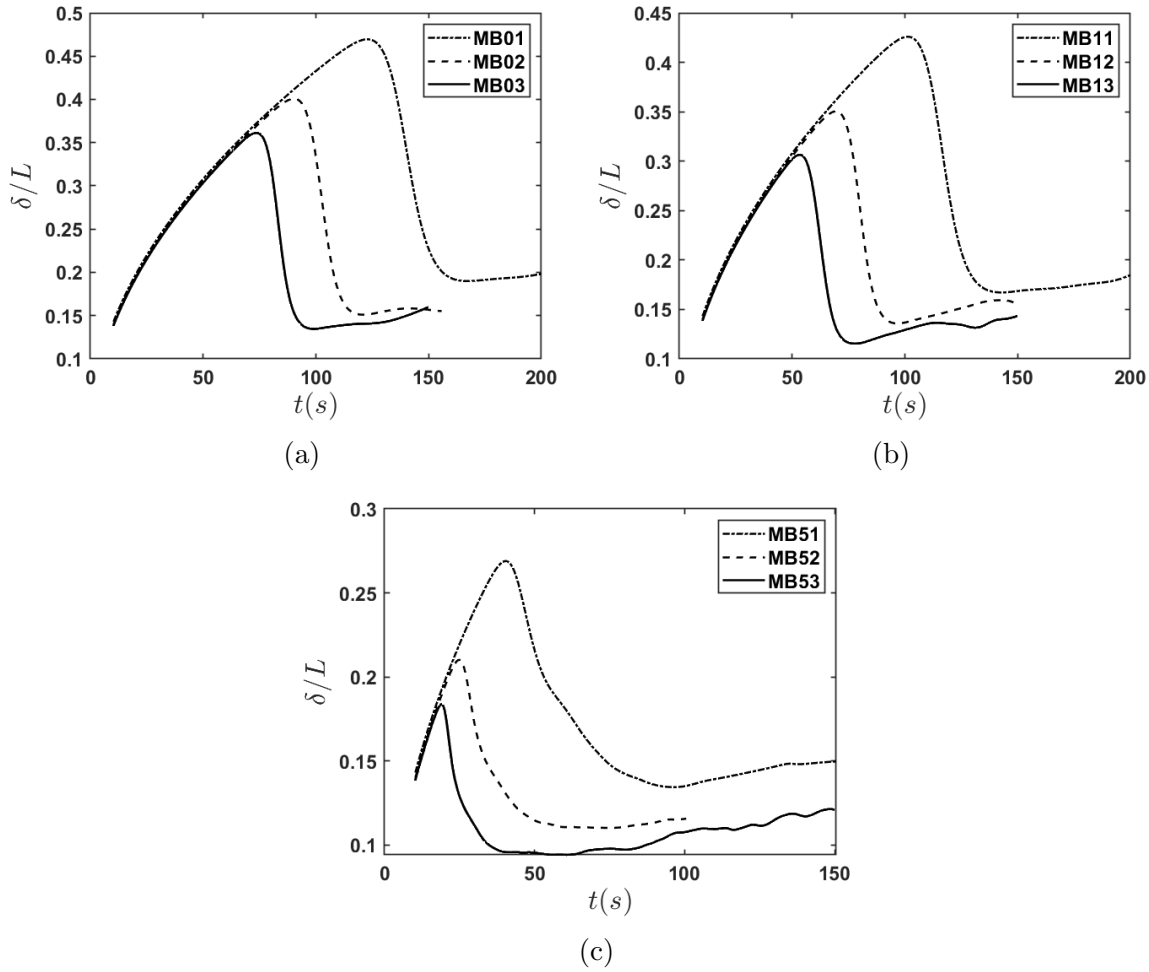

Figure 5.20: Growth of the boundary layer thickness for various values of the non-dimensional surface heat flux for Marangoni number (a) $Ma = 0$ (b) $Ma = 70$ and (c) $Ma = 350$.

Initially, in the upper bulk, when the heat flux is dominated by diffusion, resulting in a gradual increase in boundary layer (BL) thickness. It can be seen that the instability of BL thickness reaches quickly with the increasing ϕ_T, resulting in a earlier transition to turbulence in the bulk when cold water plumes starts plunges down at $t \approx 55$s for $\phi_T = 0.777$ and at $t \approx 97$s for $\phi_T = 1.5$, while for $\phi_T = 2.33$ it takes until $t \approx 132$s. This shows that an increase in ϕ_T promotes instantaneous development of instability. Similar results can be seen for $Ma > 0$. The boundary layer thickness increases with time before it starts decreasing and the either fluctuates (MB13 and MB53) or gradually decreases (MB11, MB12, MB51 and MB52) in time. It can also be seen that the instability of boundary layer thickness appears to reach more rapidly with increasing Marangoni number. For $Ma = 0$ (case MB03), it already appears at $t \approx 55$s, for $Ma = 70$ (case MB13) at $t \approx 49$s and for $Ma = 350$ (case MB53) at $t \approx 22$s.

5.7.2 Horizontally averaged temperature and concentration profiles

The effect of Marangoni forces on the horizontally averaged surface temperature is shown in Figure 5.21. In all simulations, a constant non-dimensional heat flux of $\phi_T = 1.5$ was applied. In all cases, initially the turbulent boundary layer thickens due to diffusion dominating the transfer process. As soon as thermal plumes start to fall down relatively cold water from the surface is transported towards the bulk. Simultaneously, warm fluid from the bulk is brought up resulting in an increased surface temperature.

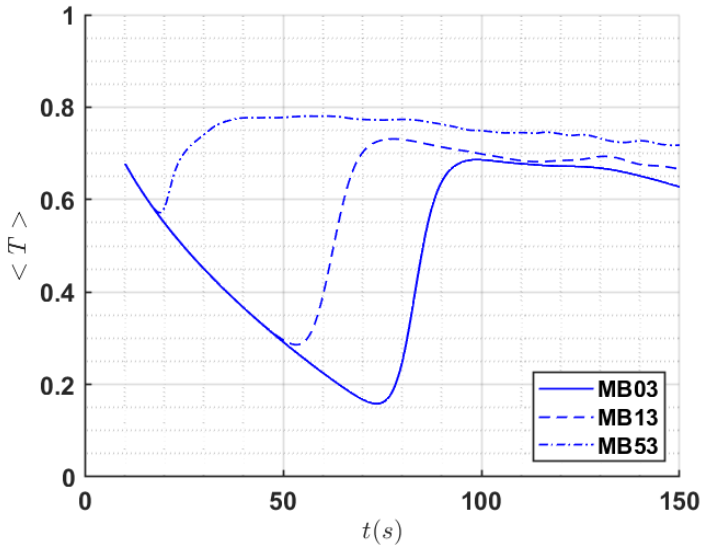

Figure 5.21: Influence of different values of Marangoni $Ma = 0, 70, 350$ on the horizontally averaged surface temperature in the presence of a constant value of the non-dimensional surface heat flux of $\phi_T = 1.5$.

The falling plumes cause the flow underneath the surface to become turbulent, so that heat transfer in that region will becomes dominated by turbulent convection. Once the flow turned turbulent, the continuous turbulent convection of heat from the bulk to the surface can be seen to result in a virtually constant surface temperature. It can be seen at $t = 150\,\mathrm{s}$ the surface temperature becomes higher with increasing Marangoni numbers, so that the difference with the bulk temperature decreases. It is remarkable that even though the Marangoni effect results in an increased gas transfer it simultaneously causes a reduction in the temperature difference between the bulk and the surface. At $t = 150\,\mathrm{s}$ temperature differences between the bulk and the surface of $\Delta T = 0.37, 0.33$ and 0.28 K were observed for $Ma = 0, 70$ and 350, respectively. In Figure 5.22 the horizontally averaged temperature profiles obtained in MB03 ($Ma = 0$)

and MB53 ($Ma = 350$), both having a surface heat flux of $\phi_T = 2.33$, are compared. In simulation MB03 the temperature has the surface was found to be smaller than in MB53. This is a direct result of the increase in Marangoni number from $Ma = 0$ to $Ma = 350$ enhancing the transport of temperature from the surface to the bulk (improve mixing).

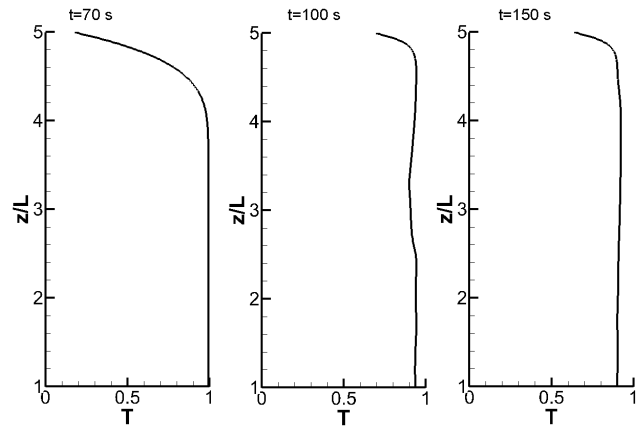

(a)

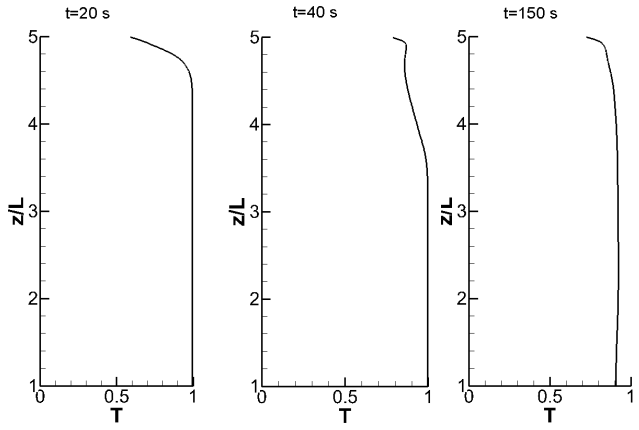

(b)

Figure 5.22: Non-dimensional horizontally averaged temperature profiles for simulation (a) MB03 and (b) MB53.

It can also be seen that the thermal boundary layer in MB03 at $t = 70$ s is very thick and entirely diffusion dominated with a very low temperature at the surface. At $t = 100$ and 150 s, the temperature at the surface is much reduced indicating the presence of turbulent heat flux, generated by the buoyant instability causing cold water plumes to plunge down. In MB53, at $t = 20$ s the thermal boundary layer is fully dominated by diffusion and at $t = 40$ s, though the buoyant instability started to generate turbulence in the upper bulk, the thermal boundary layer still shows characteristics of purely diffusive boundary layer with a relatively low temperature at the surface. At $t = 150$ s the turbulence has fully developed resulting in a thinner boundary layer in a lower surface temperature.

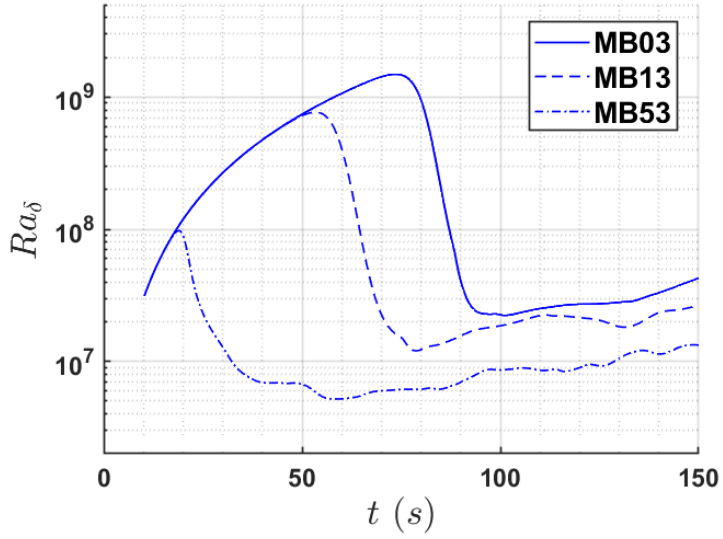

Figure 5.23: Marangoni effects on the instantaneous Rayleigh number Ra_δ in the presence of a constant non-dimensional surface heat flux of $\phi_T = 1.5$.

Figure 5.23 shows the Marangoni effect on the instantaneous Rayleigh number Ra_δ in a presence of a fixed non-dimensional surface heat flux of $\phi_T = 1.5$. Ra_δ was calcu-

lated using the boundary layer thickness $\delta = T_s/(\partial T/\partial z)$. Initially, while the vertical turbulent heat flux is still negligibly small, the heat flux in the upper bulk is still dominated by diffusion, resulting in a gradual increase in both δ and Ra_δ. With increasing Marangoni number, the Rayleigh instability gets more and more enhanced resulting in a earlier transition to turbulence in the upper bulk which is clearly visible in the figure where plumes of cold water starts falling down already at $t \approx 20$ s for $Ma = 350$ (MB53) and at $t \approx 54$ s for $Ma = 70$, while for $Ma = 0$ it takes until $t \approx 74$ s. Also, it can be seen that after the vertical turbulence heat flux is established in the upper bulk, in all simulations the temperature at the surface is much reduced. Here, induced mixing that results from the Marangoni effect causes a surface temperature that reduces with increasing Marangoni number. The Rayleigh number Ra_δ increases with time before it starts decreasing and then either fluctuates (MB53) or gradually decreases (MB03 and MB13) in time.

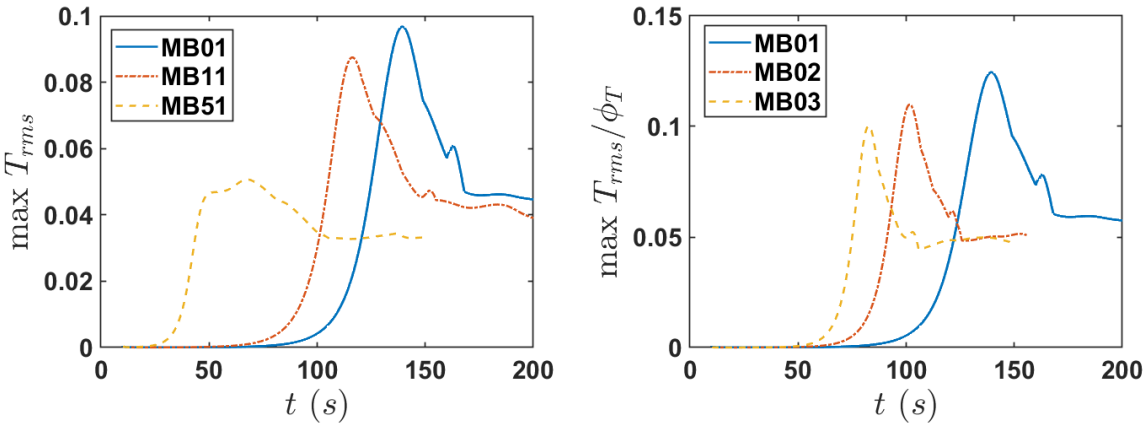

Figure 5.24: Maximum of T_{rms} in time to observe the effects of (a) Marangoni forces and (b) non-dimensional surface heat flux.

In Figure 5.24a the effect of the Marangoni forces on the maximum of the horizontal averaged temperature fluctuations in the bulk is shown at a surface heat flux of $\phi_T = 0.777$ for $Ma = 0, 70, 350$. An increase in the maximum T_{rms} indicates transition to turbulence in the upper bulk. It can be seen that the transition happens much earlier at higher Marangoni numbers. For instance, at $Ma = 350$ the sharp increase in T_{rms} already starts at $t \approx 25$ s at $Ma = 70$ it starts at $t \approx 60$ s, while at $Ma = 0$ it starts at $t \approx 80$ s. It is interesting to see that the maximum T_{rms} level in the bulk, once the flow has become fully turbulence, reduces with increasing Marangoni number. This indicates that the Marangoni forces tend to promote mixing, resulting in a reduced variance in temperature in the bulk. The effect of the surface heat flux on the maximum T_{rms} in the bulk is shown in Figure 5.24b for $Ma = 0$. The maximum T_{rms} is normalised by the non-dimensional surface heat flux. Increases in heat flux result in increases in Rayleigh number, so it is to be expected that larger heat fluxes result in earlier transition to turbulence. For instance at $\phi_T = 2.33$ (MB03) the onset of transition is at about $t \approx 50$s, at $\phi_T = 1.5$ (MB02) it is at $t \approx 65$, while at $\phi_T = 0.777$ (MB01) it is at $t \approx 80$ s. Once the upper bulk is fully turbulent the normalised T_{rms} values can be seen to be approximately equal, indicating that these maximum values scale linearly with the surface heat flux.

Figure 5.25 compares the Marangoni effect on the horizontally-averaged T_{rms} distribution as a function of the z-coordinate at $t = 101.25$ s for various surface heat fluxes, $\phi_T = 0.777, 1.5$ and 2.33. For small heat fluxes and small Marangoni numbers it takes quite a long time before the Rayleigh instability causes cold water plumes to plunge down. For instance, in figure 5.25 (a), with a heat flux of 0.777, the Rayleigh instability

in simulation MB01 ($Ma = 0$) is very slow to develop so that nonzero T_{rms} can only be found in the upper bulk while further down it is mostly zero.

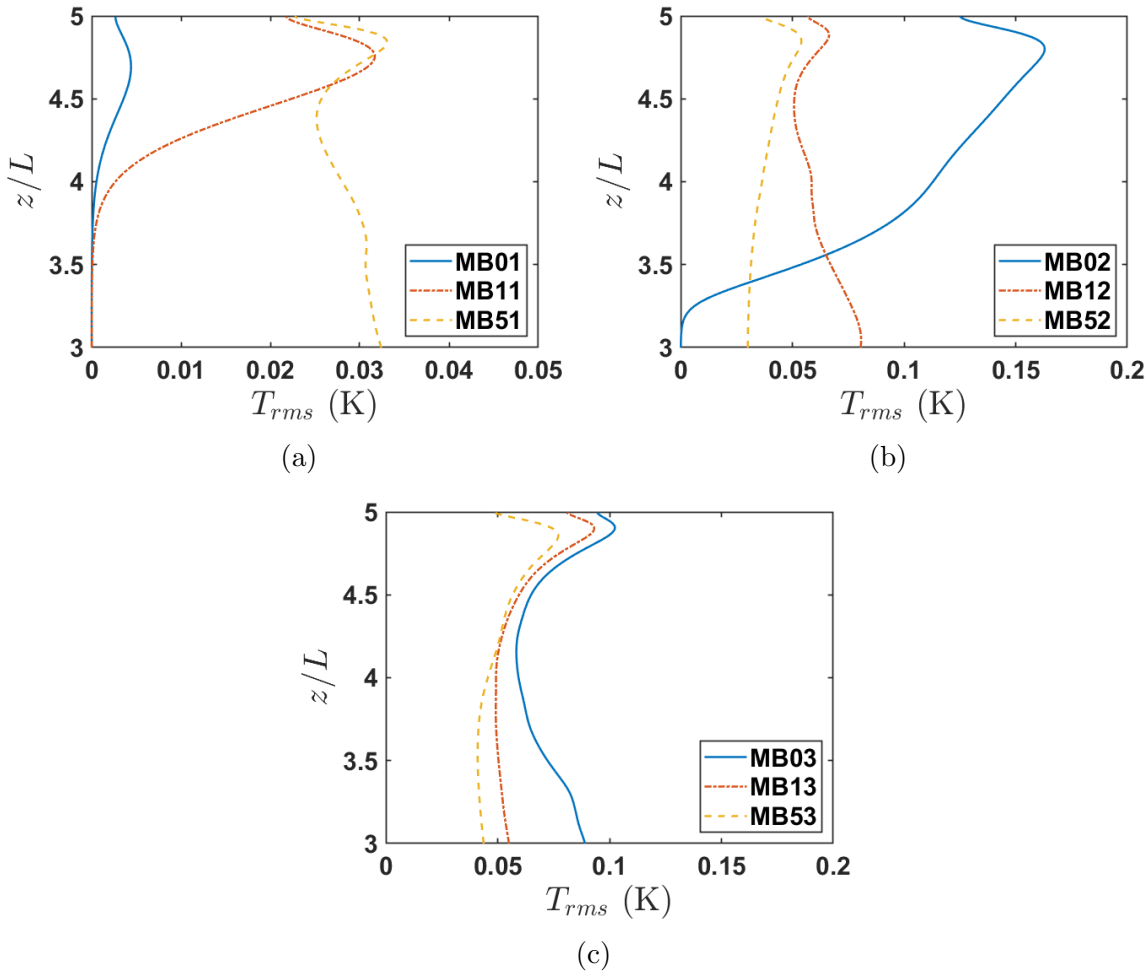

Figure 5.25: Marangoni effects on horizontally averaged T_{rms} distribution using the Schmidt number $Sc = 16$ at $t = 101.25$s for various non-dimensional surface heat flux of ϕ_T (a) 0.777, (b) 1.5 and (c) 2.33.

In MB11 ($Ma = 70$), the Rayleigh instability is somewhat enhanced by the Marangoni effects so that much larger values of T_{rms} are obtained in the upper bulk, though, also

here, deeper down into the bulk it is still zero. Only at $Ma = 350$ (MB51), the enhancement of the Rayleigh instability has been so strong that also deeper into the bulk nonzero values of T_{rms} are found.

Very similar results can be seen for the scalar concentration at $Sc = 16$, shown in Figure 5.26a . Also here, for the lowest surface heat flux of 0.777, only for the highest Marangoni number a nonzero C_{rms} is obtained in the bulk. For higher surface heat fluxes the Rayleigh instability becomes stronger and, also for lower Marangoni numbers, at $t = 101.25$ s, the instability is much more developed resulting in the introduction of more turbulence in the bulk. As shown in Figure 5.26b, at $\phi_T = 1.5$ the Rayleigh instability at $Ma = 0$ (MB02) is more developed than at $\phi_T = 0.777$ resulting in a much larger peak in T_{rms} even though the T_{rms} is still zero deeper down. At larger Marangoni numbers the instability has developed further as can be seen by the higher values of T_{rms} further down into the bulk. The main reason that the largest peak in T_{rms} in the upper bulk is reached at the lowest Marangoni number (MB02) is because in this simulation the cold plumes started to plunge down for the first time relatively recently causing a large variation in temperature in the upper bulk. Compared to the MB52, in MB12 the T_{rms} values obtained around $z/L = 3$ are found to be larger. Again, this is due to the slower development of the Rayleigh instability (enhanced by Marangoni forces with $Ma = 70$ rather than $Ma = 350$) so that the turbulent mixing in the bulk is not very well developed. Note here that in a very well mixed turbulent flow, the T_{rms} value would be almost zero. Again, the results obtained at a scalar concentration at $Sc = 16$ and a surface heat flux of $\phi_T = 1.5$, shown in Figure 5.26b, are quite similar. Also here C_{rms} is zero in the deeper bulk only for the simulation with $Ma = 0$ (MB02),

while at the same time the fresh plumes in the upper bulk cause the largest values of C_{rms} in the upper bulk. The other two simulations show a much deeper penetration of both the scalar and the turbulence in the bulk.

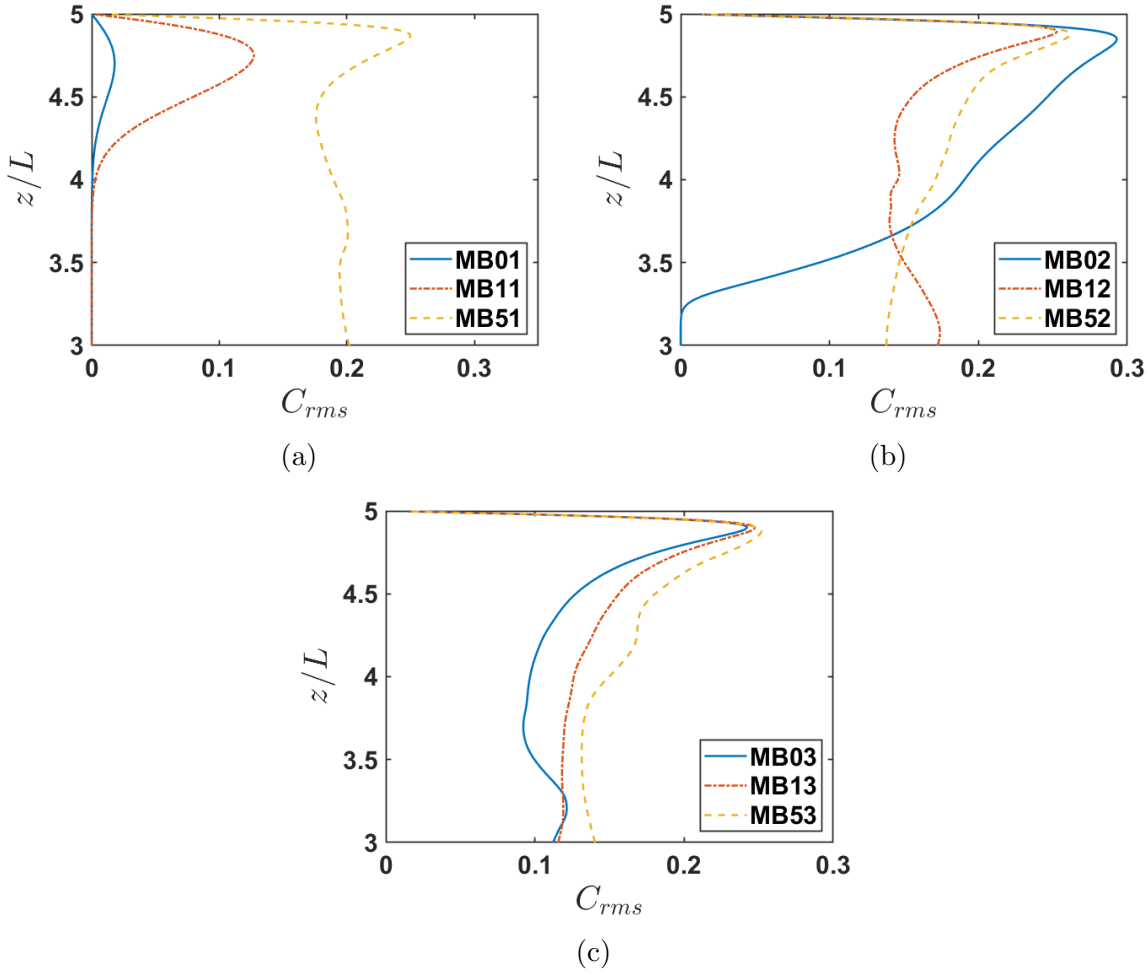

Figure 5.26: Marangoni effects on horizontally averaged C_{rms} distribution at $t = 101.25$s for various non-dimensional surface heat flux of ϕ_T (a) 0.777, (b) 1.5 and (c) 2.33.

Figure 5.25c shows the T_{rms} distribution for the highest surface heat flux $\phi_T = 2.33$. Here, in all simulations the Rayleigh instability is quite well developed as can be seen

by the nonzero values of T_{rms} for all $z/L > 3$. This figure allows us to compare the Marangoni effect for a developed Rayleigh instability. It can be seen that with increasing Marangoni number, T_{rms} tends to reduce for all z even though the surface heat flux in these simulation is exactly the same. This implies that turbulence, and hence mixing, increases with increasing Marangoni forces (that promote the Rayleigh instability). In contrast, as displayed in Figure 5.26c, despite the improved mixing the scalar concentration C_{rms} at $Sc = 16$ and a surface heat flux of $\phi_T = 2.33$ was found to slightly increase with Ma. This can be explained by an increasing scalar flux through the surface, which will tend to increase C_{rms}. That this is indeed the case will be shown in Section 5.7.4.

5.7.3 Mass flux

To determine the total mass flux, it is important to know both the convective (turbulent) and diffusive mass fluxes (see section 2.1). In Figure 5.27a and 5.27b the variation of time-space-averaged diffusive ($D\partial\overline{c}/\partial z$) and convective ($c'w'$) mass fluxes with depth carried out for $Sc = 16 - 100$ are presented for simulation MB01 and MB13. The ordinate represents the depth which was normalised with the viscous layer thickness. These figures clearly shows the influence of Schmidt number Sc on the mass fluxes. At low Sc, the region where molecular diffusion is dominant is relatively thick. However, at $Sc = 100$, the contribution of the convective fluxes is already of the order $D\partial\overline{c}/\partial z$ almost immediately below the surface. Note that the non-dimensional surface heat flux is fixed to 0.777 for all profiles. Thus, with larger Schmidt number, the convective and diffusive fluxes meet together almost immediately below the surface, as compared to

smaller Schmidt number.

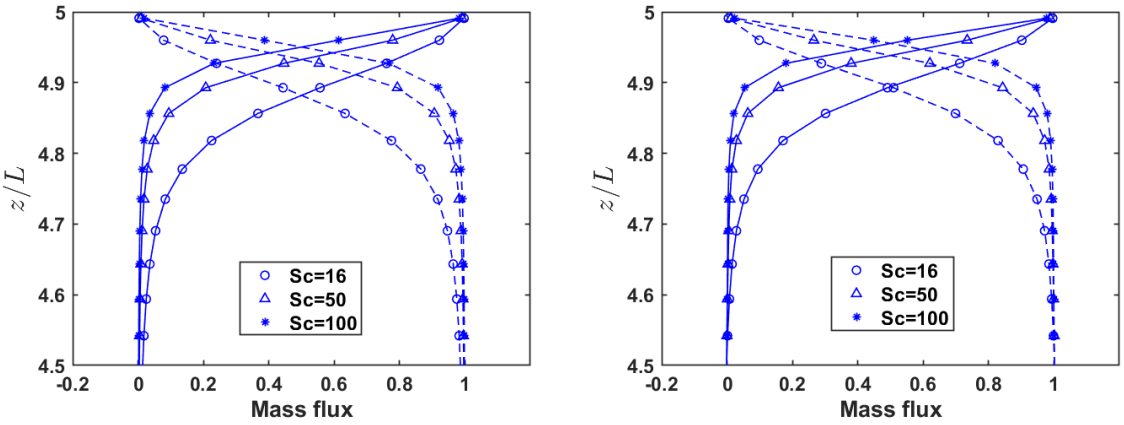

Figure 5.27: Variation of mass flux with depth at $t = 200$s using a non-dimensional heat flux of $\phi_T = 0.777$. The mass fluxes are normalised with total flux ($D\partial\overline{c}/\partial z + < c'w' >$). Diffusive $-D\partial\overline{c}/\partial z$ (solid lines) and convective $< c'w' >$ (dashed lines) mass fluxes plotted against z/L at various Sc numbers for (a) $Ma = 0$ (MB01) and (b) $Ma = 70$ (MB11). Only every fifth data point is shown.

Effect of two different Marangoni numbers on normalised mass flux profiles are shown in Figure 5.29. At the surface, the convective mass fluxes are zero as any convective transport vanishes in the immediate region of the water surface. In this region, the contribution of the diffusive flux to the transfer mechanism is maximum but reduces rapidly to 50% at around $4.94z/L$ (see Figure 5.29b). After this point, the importance of the convective mass transfer increases quickly and beyond $z \leq 4.6L$ it becomes almost completely dominant. A detailed plot is shown in Figure 5.29b. It shows that in simulation MB01 with $Ma = 0$, the region diffusive flux is dominant is relatively thick as compared to simulation MB13 with $Ma = 70$.

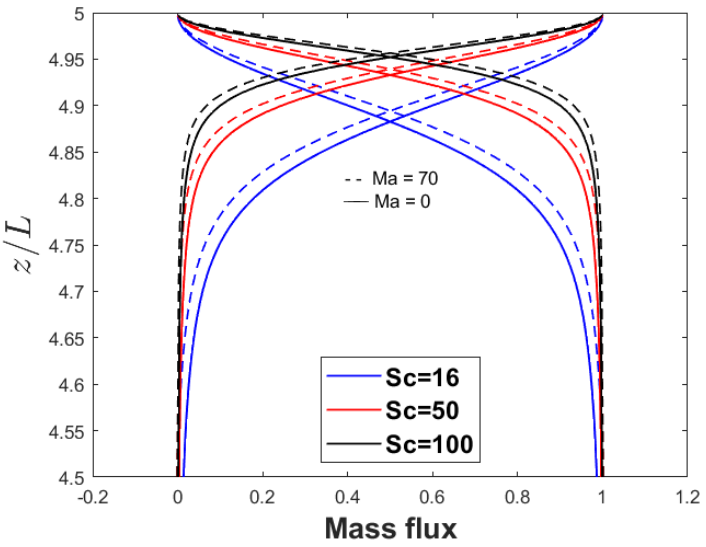

Figure 5.28: Variation of mass flux with depth z/L at various Sc numbers for $Ma = 0$ (MB01) and $Ma = 70$ (MB11) with a fixed non-dimensional heat flux $\phi_T = 0.777$ at $t = 200$s. The mass fluxes are normalised with total flux ($D\partial\overline{c}/\partial z + < c'w' >$).

We conclude that, with the smaller Marangoni number, the convective and diffusive fluxes meet together almost immediately below the surface, as compared to the larger Marangoni number.

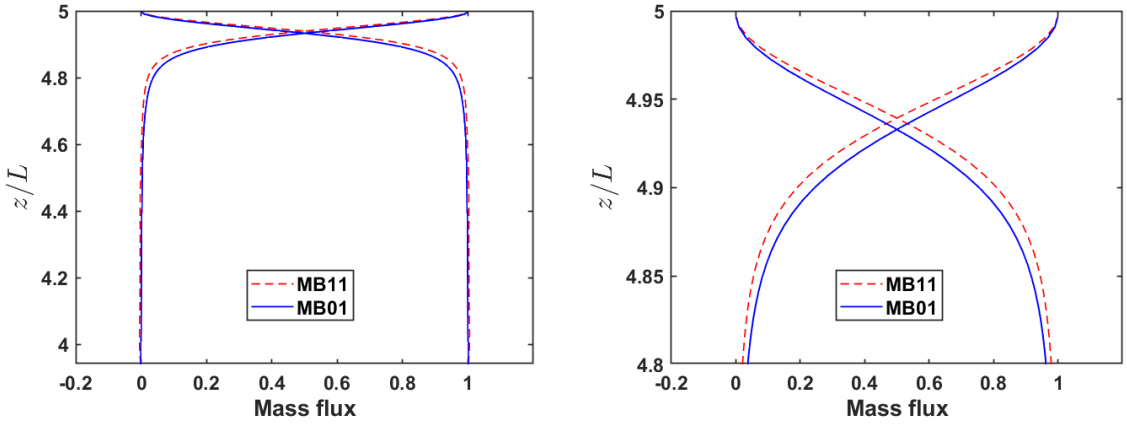

Figure 5.29: Variation of mass flux with depth for two different Marangoni numbers (a) $Ma = 0$ (blue line) and $Ma = 70$ (red line) with a constant Schmidt number $Sc = 50$ at $t = 200$s. (b) Detailed plot of variation of mass flux with depth for $Ma = 0$ and 70 with $Sc = 50$ and $\phi_T = 0.777$.

5.7.4 Gas transfer velocity

The instantaneous gas flux j at the interface is dominated by diffusion and can be written as

$$j = D\frac{\partial C}{\partial z}\Big|_i. \tag{5.30}$$

Subsequently, the averaged gas transfer K_L can be determined using the expression

$$\overline{j} = K_L(C_s - C_b) = D\frac{\partial \overline{C}}{\partial z}\Big|_i \tag{5.31}$$

where C_b and C_s are the saturated concentration in the bulk and at the interface, respectively. Figure 5.30 shows the influence of Marangoni numbers $Ma = 0, 70, 350$ on the gas transfer velocity K_L. The gas transfer velocity K_L was normalised using the

velocity scale $U = \kappa/L$. For each simulation performed at a fixed combination of Ma and heat flux, several convection diffusion equations for scalar transport were solved simultaneously for Schmidt numbers $Sc = 16, 50, 100, 200$. In Figure 5.30, the gas transfer velocity K_L was shown as a function of the Schmidt number for three different Marangoni numbers, $Ma = 0$ (MB01), 70 (MB11), 350 (MB51). The interpolating curves (M1, M2 and M3) were produced by assuming the theoretical relation

$$K_L = \frac{1}{\sqrt{Sc}}, \tag{5.32}$$

which is derived from Danckwerts' model [14] (see Section 2.4.1.3). It can be seen that, also for $Ma > 0$, Danckwerts' model still provides a very good interpolation of the results. The Marangoni forces do not appear to effect the validity of the model.

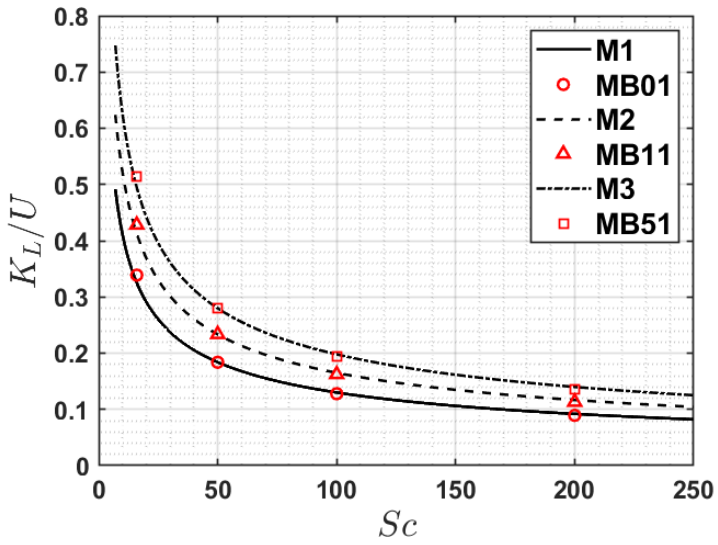

Figure 5.30: Variation of transfer velocity K_L with Schmidt number $Sc = 16, 50, 100, 200$ at time $t = 150$s.

In Figure 5.31, a comparison of the gas transfer velocity K_L (normalised with velocity scale $U = \kappa/L$) is shown with the non-dimensional surface heat flux ϕ_T. K_L(DNS) results were obtained from existing DNS. While, K_L(SDM) results were calculated using the surface divergence model.

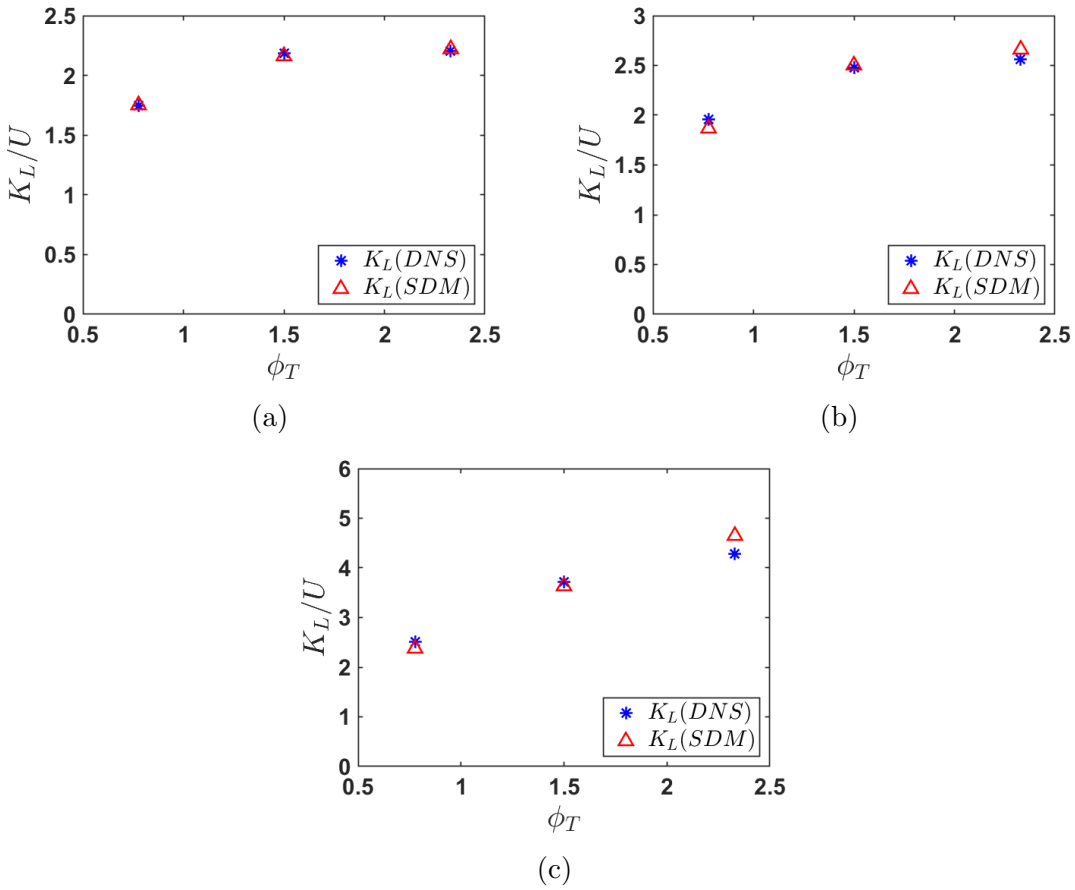

Figure 5.31: Comparison of the gas transfer velocity K_L obtained by using the surface divergence model (SDM) and the direct numerical simulation (DNS) with the non-dimensional surface heat flux for Marangoni forces (a) $Ma = 0$, (b) $Ma = 70$ and (c) $Ma = 350$.

The SDM was discussed previously in Section 2.4.1.6. This model used the rms of

the divergence of the horizontal velocity at the surface and is defined by

$$K_L = c\sqrt{D\beta'}. \tag{5.33}$$

The importance of surface divergence model (SDM) for interfacial gas transfer was shown in the study of McCready *et al.* [63]. Apart from this, many researchers further verified the model using both numerical and experimental data [32, 92, 62, 44].

In Figure 5.31, the constant of proportionality c used in SDM depends on the Marangoni number. It can be seen that the value of c slightly decreases with increasing Marangoni number. For $Ma = 0, 70$ and 350, c was fixed to $0.5956, 0.5236$ and 0.4226, respectively. For case ($Ma = 0$) in Figure 5.31a, a good agreement was found between K_L(DNS) and K_L(SDM), while in part (b) and (c) the actual quality of the surface divergence model becomes worse when Marangoni number increases from zero. Figure 5.32 shows the Marangoni effects on the gas transfer velocity K_L in time for a constant value of the non-dimensional surface heat flux $\phi_T = 0.777$. K_L was normalised using the velocity scale $U = \kappa/L$. Initially, it was found that the transfer velocity smoothly decreases with time before it sharply increases and then either fluctuates about a plateau (MB53) or slowly decreases in time (MB03 and MB13). The initial decrease in K_L corresponds to the period in which gas transfer is completely dominated by diffusion. As the concentration boundary layer becomes thicker and thicker, its gradient at the surface reduces resulting in a lower K_L value. The sudden increase in K_L happens when plumes of saturated flow start to plunge down. The falling plumes significantly reduce the thickness of the concentration boundary layer at the surface, resulting in a larger concentration gradient at the surface, and hence in a larger K_L value.

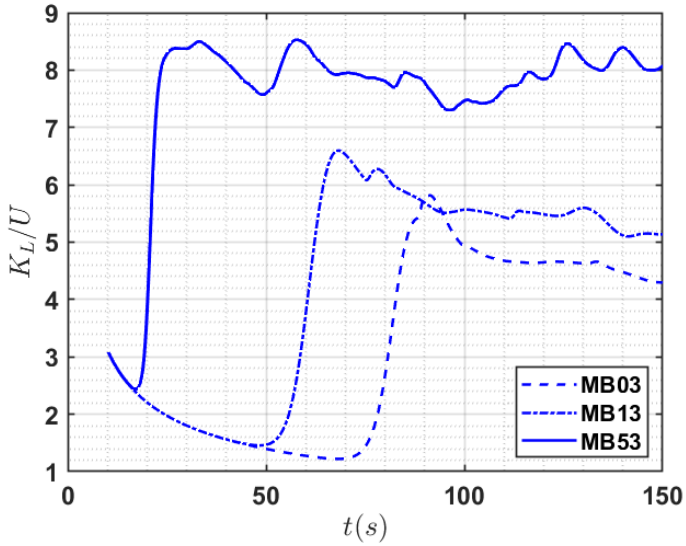

Figure 5.32: Effect of Marangoni $Ma = 0, 70, 350$ on the gas transfer velocity K_L.

After the initial phase of plumes plunging down, the near-surface flow gradually becomes turbulent, resulting in a continuous turbulent convective transfer of saturated flow from the surface to the bulk. At $Ma = 0$ and $Ma = 70$ (no or a relatively small Marangoni effect) the gas transfer in the final phase gradually reduces in time while for the higher Marangoni number, $Ma = 350$ (MB53), the gas transfer velocity remains more or less constant. As the heat transfer gradient in the three simulations was exactly the same, any differences in K_L are the result of differences in Marangoni number. At $t = 150\,\mathrm{s}$, compared to $Ma = 0$, at $Ma = 70$ the gas transfer velocity was found to increase by about 21%, while at $Ma = 350$ this increase was approximately 90%. This illustrates the effectiveness of temperature induced Marangoni forces in promoting interfacial gas transfer.

5.8 Conclusion

The aim of the research presented in this chapter was to investigate the importance of surface temperature-gradient-induced Marangoni forces when simulating the development of a buoyant convective instability driven by a fixed temperature-gradient at the surface (to model cooling). It was found that the Marangoni forces significantly promote the buoyant (Rayleigh) instability and not only lead to a much faster development of the instability but also result in a more intense turbulent mixing in the upper bulk. The increased turbulent mixing in the upper bulk results in a more effective transport of heat from the surface downwards. Comparing simulations with the same, fixed, surface temperature gradient the Marangoni-induced increased transport of heat away from the surface results in a reduced difference between surface and bulk temperature. With further increases in Marangoni number, this difference between surface and bulk temperature was found reduce even further. Finally, the Marangoni-induced increase in turbulent mixing in the bulk, also resulted in a significant increase in air-water gas transfer.

Chapter 6

Conclusion and suggestions for future work

6.1 Conclusion

In the present study, the mean surface age was approximated by two different approaches: i) The Lagrangian particle tracking approach and ii) The continuum approach. Generally in fluid mechanics, Lagrangian methods (with the frame of reference moving with the flow) and Eulerian methods (with fixed frame of reference) can both be used to calculate fluid flow.

The Lagrangian particle tracking method is based on tracking trajectories of discrete fluid particles so that the surface age of each individual particle can be determined directly. After determining the mean surface age from tracking the trajectories of a large number of particles, the gas transfer velocity K_L is usually calculated using (a

possibly modified version of) Danckwerts' model. The simultaneous tracking of huge quantities of particles is the main disadvantage of the Lagrangian method as it requires extensive book keeping. Hence, to introduce this tracking of huge numbers of individual particles in traditional Eulerian codes (in which the continuum assumption is employed) extensive modifications are required, especially in massively parallel codes. A more natural way to calculate the mean surface age in such codes is to use a continuum approach and replace the individual particles by a surface age density distribution.

In contrast to the Lagrangian particle tracking method, the fluid parcels employed in the continuum method can deform, so that positive surface divergence will result in enlargement of the surface area of the parcel, while negative surface divergence will make it smaller. This extra degree of freedom is the main difference between the Lagrangian and the continuum approach. The latter was found to be a good predictor of the gas transfer velocity (with a maximum error of about 8%).

A series of direct numerical simulations (DNS) was performed to study the effects of Marangoni forces on the instantaneous development of a buoyant convective instability for several Sc-numbers per simulation. For the flow solver, the convective terms were solved using a fourth order kinetic energy conserving discretization described in [91], while the diffusive term was solved using the fourth order central scheme. After substituting the descritized momentum equations into the continuity equation a Poison equation for the pressure was obtained. This Poison equation for the pressure was solved using the conjugate gradient method with simple diagonal decomposition. Time integration was performed using the second order Adams-Bashforth method. Simultaneously with the flow, five scalar convection diffusion equations were solved. The first

scalar, the temperature, is non passive as it affects the flow through buoyancy forces. The other scalars are passive and represent the transport of atmospheric gases. The Prandtl number for the temperature was $Pr = 7$ and the Schmidt numbers for the mass transport were $Sc = 16, 50, 100, 200$. The simultaneous calculation of the four transport equations for the scalar concentration allows a non biased comparison of the effect of Schmidt number on the gas transfer velocity K_L. The setup of the computational simulations was inspired by the experiments carried out by Jirka *et al.* [41]. A $200 \times 200 \times 252$ baseline mesh was employed to solved both the flow, temperature and the scalar transport equation at $Sc = 16$. For the scalar transport equations at higher Schmidt numbers ($Sc = 50, 100, 200$) the basemesh was refined by a factor of two in all directions.

A grid refinement study was performed to assess the adequacy of the resolution used for the base mesh. The results shows that all velocity profiles were in excellent agreement. The largest difference observed between the velocities in the various simulations was less than 10^{-8}, which is negligibly small. Based on the similarities between the results obtained on the three refined meshes, it was concluded that the mesh size used in MB10 (see Table 5.2) was sufficiently fine to accurately resolve the buoyant instability.

Furthermore, The Marangoni effect on the turbulent flow statistics was evaluated for a range of Marangoni number ($Ma = 0, 70, 350$) at time $t = 150$s. Both horizontal and vertical velocity fluctuation level change due to the Marangoni effect. Note that with increasing Marangoni number the horizontal fluctuations at the surface were found to increase, which is the direct consequence of the Marangoni forces acting at the surface

to promote Rayleigh instability.

A study of gas transfer velocity was carried out for four Schmidt numbers ranging from $Sc = 16$ to $Sc = 200$. For $Ma = 0$, the gas transfer velocity shows a very good Schmidt number scalability with $Sc^{-1/2}$, the scaling as used in Danckwerts' model.

The variation of diffusive and convective mass fluxes were estimated for a range of Schmidt numbers $Sc = 16$-100. With increasing Schmidt number the location where the convective (turbulent) and diffusive gas fluxes were found to balance was observed to get closer and closer to the surface. This is directly related to reductions with Schmidt number in the thickness of the concentration boundary layer adjacent to the surface.

We conclude that, the Marangoni forces that promote the Rayleigh instability result in significant increase in the amount of atmospheric gases transferred across the air-water interface and, hence, should not be neglected.

6.2 Suggestions for future work

So far the continuum method was only used to estimate the mean surface age and to calculate the gas transfer velocity K_L from the mean surface age, Danckwerts' model was subsequently employed. More investigation will be needed to be able to directly calculate the gas transfer velocity using the continuum method.

As the continuum method is especially suited to calculate the mean surface age without the need to track a huge number of particle paths, it would be nice to see it implemented inside the main flow solver. The advantage of this would be that the accuracy of the mean surface age calculations would improve by the availability of the time dependent 3D velocity field near the surface (avoiding the need to either interpolate

between snapshots of the interfacial velocity or use a frozen velocity assumption).

It is unlikely that the assumption of a constant heat flux at the surface is a completely accurate model for evaporative heat transfer. This needs to be further investigated, for instance by explicitly resolving not only the water side but also the air above the water surface. In this way, the rate of evaporation can be directly calculated and continuity can be ensured that the diffusive fluxes at the surface (on the air side and the water side). Based on the results obtained in Chapter 5, it is likely that Marangoni effects due to temperature gradients at the surface will persist to play an important role in interfacial gas transfer.

The enhancement found of the interfacial gas transfer velocity by the surface temperature gradient induced Marangoni effect shows that the role of buoyancy induced turbulence on interfacial mass transfer might be much more important than previously thought. It would be worthwhile to assess this by performing simulations of air-water gas transfer driven by, for instance, buoyancy induced and bottom shear induced turbulence and perhaps also study the relative importance of buoyancy induced turbulence compared to wind shear induced turbulence at lower wind speeds.

Bibliography

[1] Ahlers, G., Grossmann, S. and Lohse, D. (2009), 'Heat transfer and large scale dynamics in turbulent rayleigh-bénard convection', *Reviews of modern physics* **81**(2), 503.

[2] Ali, F., Wissink, J. G. and Herlina, H. (2018), 'Modeling air-water heat transfer induced by buoyant convection', *International Journal of Computational Physics Series* **1**(2), 15–16.

[3] Atmane, M. A. and George, J. (2002), 'Gas transfer across a zero-shear surface: a local approach', *Washington DC American Geophysical Union Geophysical Monograph Series* **127**, 255–259.

[4] Balachandar, S. (1992), 'Structure in turbulent thermal convection', *Physics of Fluids A: Fluid Dynamics* **4**(12), 2715–2726.

[5] Balachandar, S., Maxey, M. and Sirovich, L. (1989), 'Numerical simulation of high rayleigh number convection', *Journal of Scientific Computing* **4**(2), 219–236.

[6] Balsara, D. S. and Shu, C. W. (2000), 'Monotonicity preserving weighted essen-

tially non-oscillatory schemes with increasingly high order of accuracy', *Journal of Computational Physics* **160**(2), 405–452.

[7] Banerjee, S., Scott, D. and Rhodes, E. (1968), 'Mass transfer to falling wavy liquid films in turbulent flow', *Industrial & Engineering Chemistry Fundamentals* **7**(1), 22–27.

[8] Borges, R., Carmona, M., Costa, B. and Don, W. S. (2008), 'An improved weighted essentially non-oscillatory scheme for hyperbolic conservation laws', *Journal of Computational Physics* **227**(6), 3191–3211.

[9] Brubaker, J. M. (1987), 'Similarity structure in the convective boundary layer of a lake', *Nature* **330**(6150), 742–745.

[10] Brumley, B. (1988), 'Air-water transfer of slightly soluble gases: Turbulence, interfacial processes and conceptual models', *Physicochemical hydrodynamics* **10**(3), 295–319.

[11] Brumley, B. H. and Jirka, G. H. (1988), 'Air-water transfer of slightly soluble gases: turbulent interfacial processes and conceptual models', *Physico Chemical Hydrodynamics* **10**(3), 295–319.

[12] Chung, B. T., Fan, L. and Hwang, C. (1971), 'Surface renewal and penetration models in the transient state', *AIChE Journal* **17**(1), 154–160.

[13] Curry, J. H., Herring, J. R., Loncaric, J. and Orszag, S. A. (1984), 'Order and disorder in two-and three-dimensional benard convection', *Journal of Fluid Mechanics* **147**, 1–38.

[14] Danckwerts, P. V. (1951), 'Significance of liquid-film coefficients in gas absorption', *Industrial & Engineering Chemistry* **43**(6), 1460–1467.

[15] De Angelis, V., Lombardi, P. and Banerjee, S. (1997), 'Direct numerical simulation of turbulent flow over a wavy wall', *Physics of Fluids (1994-present)* **9**(8), 2429–2442.

[16] Deane, A. E. and Sirovich, L. (1991), 'A computational study of rayleigh–bénard convection. part 1. rayleigh-number scaling', *Journal of fluid mechanics* **222**, 231–250.

[17] Deardorff, J. W. (1972), 'Numerical investigation of neutral and unstable planetary boundary layers', *Journal of the Atmospheric Sciences* **29**(1), 91–115.

[18] Deardorff, J. W. (1974), 'Three-dimensional numerical study of the height and mean structure of a heated planetary boundary layer', *Boundary-Layer Meteorology* **7**(1), 81–106.

[19] Donelan, M. A. and Wanninkhof, R. (2002), 'Gas transfer at water surfaces—concepts and issues', *Washington DC American Geophysical Union Geophysical Monograph Series* **127**, 1–10.

[20] Enmore, H. and Weat, W. (n.d.), Effects of water temperature on stream reaeration, j sanitary engrg div, *in* 'Proc. ASCE', Vol. 87, pp. 59–71.

[21] Eugster, W., Kling, G., Jonas, T., McFadden, J. P., Wüest, A., MacIntyre, S. and Chapin III, F. S. (2003), 'Co2 exchange between air and water in an arctic

alaskan and midlatitude swiss lake: Importance of convective mixing', *Journal of Geophysical Research: Atmospheres* **108**(D12).

[22] Fan, L., Shen, B. and Chou, S. (1993), 'The surface-renewal theory of interphase transport: a stochastic treatment', *Chemical engineering science* **48**(23), 3971–3982.

[23] Fortescue, G. and Pearson, J. (1967), 'On gas absorption into a turbulent liquid', *Chemical Engineering Science* **22**(9), 1163–1176.

[24] Graham, N. and Barnett, T. (1987), 'Sea surface temperature, surface wind divergence, and convection over tropical oceans', *Science* **238**(4827), 657–659.

[25] Grötzbach, G. (1982), 'Direct numerical simulation of laminar and turbulent bénard convection', *Journal of Fluid Mechanics* **119**, 27–53.

[26] Grötzbach, G. (1983), 'Spatial resolution requirements for direct numerical simulation of the rayleigh-bénard convection', *Journal of computational physics* **49**(2), 241–264.

[27] Gulliver, J. S. and Halverson, M. J. (1989), 'Air-water gas transfer in open channels', *Water Resources Research* **25**(8), 1783–1793.

[28] Harrington, L., Prisk, G. K. and Darquenne, C. (2006), 'Importance of the bifurcation zone and branch orientation in simulated aerosol deposition in the alveolar zone of the human lung', *Journal of Aerosol Science* **37**(1), 37–62.

[29] Harriott, P. (1962), 'A random eddy modification of the penetration theory', *Chemical Engineering Science* **17**(3), 149–154.

[30] Henrick, A. K., Aslam, T. D. and Powers, J. M. (2005), 'Mapped weighted essentially non-oscillatory schemes: achieving optimal order near critical points', *Journal of Computational Physics* **207**(2), 542–567.

[31] Herlina, H. (2005), 'Gas transfer at the air-water interface in a turbulent flow environment'.

[32] Herlina, H. and Wissink, J. (2014), 'Direct numerical simulation of turbulent scalar transport across a flat surface', *Journal of Fluid Mechanics* **744**, 217–249.

[33] Herlina, H. and Wissink, J. (2016), 'Isotropic-turbulence-induced mass transfer across a severely contaminated water surface', *Journal of Fluid Mechanics* **797**, 665–682.

[34] Higbie, R. (1935), 'The rate of absorption of a pure gas into a still liquid during short periods of exposure', *Trans. AIChE* **31**, 365–389.

[35] Hryb, D., Cardozo, M., Ferro, S. and Goldschmit, M. (2009), 'Particle transport in turbulent flow using both lagrangian and eulerian formulations', *International Communications in Heat and Mass Transfer* **36**(5), 451–457.

[36] Imberger, J. (1985), 'The diurnal mixed layer 1', *Limnology and oceanography* **30**(4), 737–770.

[37] Jähne, B. and Haußecker, H. (1998), 'Air-water gas exchange', *Annual Review of Fluid Mechanics* **30**(1), 443–468.

[38] Jähne, B., Huber, W., Dutzi, A., Wais, T. and Ilmberger, J. (1984), Wind/wave-tunnel experiment on the schmidt number—and wave field dependence of air/water gas exchange, *in* 'Gas transfer at water surfaces', Springer, pp. 303–309.

[39] Jähne, B., Münnich, K. O., Bösinger, R., Dutzi, A., Huber, W. and Libner, P. (1987), 'On the parameters influencing air-water gas exchange', *Journal of Geophysical Research: Oceans* **92**(C2), 1937–1949.

[40] Jiang, G. S. and Shu, C. W. (1996), 'Efficient implementation of weighted eno schemes', *Journal of computational physics* **126**(1), 202–228.

[41] Jirka, G. H., Herlina, H. and Niepelt, A. (2010), 'Gas transfer at the air–water interface: experiments with different turbulence forcing mechanisms', *Experiments in Fluids* **49**(1), 319–327.

[42] Jirka, G. H. and Ho, A. H.-W. (1990), 'Measurements of gas concentration fluctuations at water surface', *Journal of Hydraulic Engineering* **116**(6), 835–847.

[43] Jonas, T., Stips, A., Eugster, W. and Wüest, A. (2003), 'Observations of a quasi shear-free lacustrine convective boundary layer: Stratification and its implications on turbulence', *Journal of Geophysical Research: Oceans* **108**(C10).

[44] Kermani, A. and Shen, L. (2009), 'Surface age of surface renewal in turbulent interfacial transport', *Geophysical Research Letters* **36**(10).

[45] Kerr, R. M. (1996), 'Rayleigh number scaling in numerical convection', *Journal of Fluid Mechanics* **310**, 139–179.

[46] Kolmogorov, A. (1945), 'A number of target hits by several shots and general principles of effectiveness of gunfire', *Proc. Moscow Inst. Math* (12).

[47] Koppel, L., Patel, R. and Holmes, J. (1966), 'Statistical models for surface renewal in heat and mass transfer: Part i. dependence of average transport coefficients on age distribution', *AIChE Journal* **12**(5), 941–946.

[48] Kraus, E. B. and Businger, J. A. (1994), *Atmosphere-ocean interaction*, Vol. 27, Oxford University Press.

[49] Kubrak, B., Herlina, H., Greve, F. and Wissink, J. G. (2013), 'Low-diffusivity scalar transport using a weno scheme and dual meshing', *Journal of Computational Physics* **240**, 158–173.

[50] Kunugi, T., Satake, S. I. and Ose, Y. (2001), 'Direct numerical simulation of carbon-dioxide gas absorption caused by turbulent free surface flow', *International journal of heat and fluid flow* **22**(3), 245–251.

[51] Lai, A. C. and Chen, F. (2007), 'Comparison of a new eulerian model with a modified lagrangian approach for particle distribution and deposition indoors', *Atmospheric Environment* **41**(25), 5249–5256.

[52] Lakehal, D., Fulgosi, M., Yadigaroglu, G. and Banerjee, S. (2003), 'Direct numerical simulation of turbulent heat transfer across a mobile, sheared gas-liquid interface', *Journal of heat transfer* **125**(6), 1129–1139.

[53] Lamont, J. C. and Scott, D. (1970), 'An eddy cell model of mass transfer into the surface of a turbulent liquid', *AIChE Journal* **16**(4), 513–519.

[54] Lapham, G., Dowling, D. and Schultz, W. (1999), 'In situ force-balance tensiometry', *Experiments in fluids* **27**(2), 157–166.

[55] Lee, M. (2002), 'Visualization of oxygen transfer across the air–water interface using a fluorescence oxygen visualization method', *Water research* **36**(8), 2140–2146.

[56] LeVeque, R. J. (2007), *Finite difference methods for ordinary and partial differential equations: steady-state and time-dependent problems*, SIAM.

[57] Lewis, W. and Whitman, W. (1924), 'Principles of gas absorption.', *Industrial & Engineering Chemistry* **16**(12), 1215–1220.

[58] Liu, X.-D., Osher, S. and Chan, T. (1994), 'Weighted essentially non-oscillatory schemes', *Journal of computational physics* **115**(1), 200–212.

[59] Lombard, L. (n.d.), 'Oceanic oxygen changes as a bellwether of climate change'.

[60] Lombardi, P., De Angelis, V. and Banerjee, S. (1996), 'Direct numerical simulation of near-interface turbulence in coupled gas-liquid flow', *Physics of Fluids (1994-present)* **8**(6), 1643–1665.

[61] MacIntyre, S., Eugster, W. and Kling, G. W. (2002), 'The critical importance of buoyancy flux for gas flux across the air-water interface', *Geophysical Monograph-American Geophysical Union* **127**, 135–140.

[62] Magnaudet, J. and Calmet, I. (2006), 'Turbulent mass transfer through a flat shear-free surface', *Journal of Fluid Mechanics* **553**, 155–185.

[63] McCready, M., Vassiliadou, E. and Hanratty, T. (1986), 'Computer simulation of turbulent mass transfer at a mobile interface', *AIChE Journal* **32**(7), 1108–1115.

[64] Mckenna, S. P. and Mcgillis, W. R. (2002), 'Surface divergence and air-water gas transfer', *GEOPHYSICAL MONOGRAPH-AMERICAN GEOPHYSICAL UNION* **127**, 129–134.

[65] Merlivat, L. and Memery, L. (1983), 'Gas exchange across an air-water interface: Experimental results and modeling of bubble contribution to transfer', *Journal of Geophysical Research: Oceans* **88**(C1), 707–724.

[66] Moog, D. B. and Jirka, G. H. (1998), 'Analysis of reaeration equations using mean multiplicative error', *Journal of Environmental Engineering* **124**(2), 104–110.

[67] Moog, D. B. and Jirka, G. H. (1999), 'Stream reaeration in nonuniform flow: Macroroughness enhancement', *Journal of Hydraulic Engineering* **125**(1), 11–16.

[68] Moog, D. B. and Jirka, G. H. (2002), 'Air-water gas transfer in uniform flows with large gravel-bed roughness', *Washington DC American Geophysical Union Geophysical Monograph Series* **127**, 371–375.

[69] O'Connor, D. J. and Dobbins, W. E. (1956), 'The mechanics of reaeration in natural streams', *Journal of the Sanitary Engineering Division* **82**(6), 1–30.

[70] Patel, R. G., Desjardins, O., Kong, B., Capecelatro, J. and Fox, R. O. (2017), 'Verification of eulerian–eulerian and eulerian–lagrangian simulations for turbulent fluid–particle flows', *AIChE Journal* **63**(12), 5396–5412.

[71] Perlmutter, D. (1961), 'Surface-renewal models in mass transfer', *Chemical Engineering Science* **16**(3-4), 287–296.

[72] Plate, E. and Friedrich, R. (1984), Reaeration of open channel flow, *in* 'Gas transfer at water surfaces', Springer, pp. 333–346.

[73] Sabersky, R. H. and Hauptenn, A. J. A. E. G. (1964), 'Fluid flow; a first course in fluid mechanics, macmillan publishing company', *New York* .

[74] Sander, J., Simon, A., Jonas, T. and Wüest, A. (2000), 'Surface turbulence in natural waters: A comparison of large eddy simulations with microstructure observations', *Journal of Geophysical Research: Oceans* **105**(C1), 1195–1207.

[75] Schladow, S. G., Lee, M., Hürzeler, B. E. and Kelly, P. B. (2002), 'Oxygen transfer across the air-water interface by natural convection in lakes', *Limnology and Oceanography* **47**(5), 1394–1404.

[76] Schwartz, J. and Dockery, D. W. (1992), 'Increased mortality in philadelphia associated with daily air pollution concentrations', *American review of respiratory disease* **145**(3), 600–604.

[77] Shay, T. J. and Gregg, M. (1986), 'Convectively driven turbulent mixing in the upper ocean', *Journal of Physical Oceanography* **16**(11), 1777–1798.

[78] Shay, T. J. and Gregg, M. C. (1984), 'Turbulence in an oceanic convective mixed layer', *Nature* **310**(5975), 282–285.

[79] Shu, C. W. and Osher, S. (1988), 'Efficient implementation of essentially non-oscillatory shock capturing schemes, 2'.

[80] Smithson, P. A. (2002), 'Ipcc, 2001: climate change 2001: the scientific basis. contribution of working group 1 to the third assessment report of the intergovernmental panel on climate change, edited by jt houghton, y. ding, dj griggs, m. noguer, pj van der linden, x. dai, k. maskell and ca johnson (eds). cambridge university press, cambridge, uk, and new york, usa, 2001. no. of pages: 881. price£ 34.95, us 49.95,isbn0-521-01495-6(paperback).£90.00,us 130.00, isbn 0-521-80767-0 (hardback).', *International Journal of Climatology: A Journal of the Royal Meteorological Society* **22**(9), 1144–1144.

[81] Son, J. S. and Hanratty, T. J. (1967), 'Limiting relation for the eddy diffusivity close to a wall', *AIChE Journal* **13**(4), 689–696.

[82] Suga, K. and Kubo, M. (2010), 'Modelling turbulent high schmidt number mass transfer across undeformable gas–liquid interfaces', *International Journal of Heat and Mass Transfer* **53**(15), 2989–2995.

[83] Tamburrino, A. and Gulliver, J. S. (2002), 'Free-surface turbulence and mass transfer in a channel flow', *AIChE Journal* **48**(12), 2732–2743.

[84] Thackston, E. L. and Krenkel, P. A. (1969), 'Reaeration prediction in natural streams', *Journal of the Sanitary Engineering Division* **95**(1), 65–94.

[85] Theofanous, T. (1984), Conceptual models of gas exchange, *in* 'Gas transfer at water surfaces', Springer, pp. 271–281.

[86] Thomas and Edison (1985), 'Numerical simulation of the turbulent rayleighbnard problem using subgrid modelling', *Journal of Fluid Mechanics* **158**, 245–268.

[87] Upstill-Goddard, R., Watson, A., Liss, P. and Liddicoat, M. (1990), 'Gas transfer velocities in lakes measured with sf6', *Tellus B* **42**(4), 364–377.

[88] Vargaftik, N. B. (1975), 'Tables on the thermophysical properties of liquids and gases in normal and dissociated states'.

[89] Vargaftik, N., Volkov, B. and Voljak, L. (1983), 'International tables of the surface tension of water', *Journal of Physical and Chemical Reference Data* **12**(3), 817–820.

[90] Wilson, R., Spengler, J. D. et al. (1996), *Particles in our air: concentrations and health effects*, Harvard School of Public Health Cambridge, MA.

[91] Wissink, J. (2004), 'On unconditional conservation of kinetic energy by finite-difference discretizations of the linear and non-linear convection equation', *Computers & fluids* **33**(2), 315–343.

[92] Wissink, J. and Herlina, H. (2016), 'Direct numerical simulation of gas transfer across the air–water interface driven by buoyant convection', *Journal of Fluid Mechanics* **787**, 508–540.

[93] Zeman, O. and Lumley, J. L. (1976), 'Modeling buoyancy driven mixed layers', *Journal of the Atmospheric Sciences* **33**(10), 1974–1988.